

Chapter 4

Planar Arrays and Apertures

In this chapter we discuss analysis and synthesis techniques for planar arrays. A planar array is an array whose elements all lie in the xy -plane.

In the array case, we consider three types of element geometries, as shown in figures 4.1, 4.2, and 4.3. We find that both the element topology and the boundaries are important. In the aperture case, we consider two cases, as shown in Figure 4.4.

Many of the ideas that we developed for linear arrays and apertures carry over to the planar case. In other cases, extensions are necessary. As in the linear array case, our development is a combination of classical antenna theory and finite impulse response filter theory. Classical antenna references that discuss planar arrays include [Ell81], [Bal82], [Mai94], [Ma74], [Ste81], and [Zio95]. Two-dimensional FIR filter references include [RG75] and [DM84].

In Section 4.1, we consider array geometries utilizing a rectangular element grid. We extend the techniques in Chapter 3 to the analysis and synthesis of rectangular arrays.

In Section 4.2, we develop analysis and synthesis procedures for circular arrays and ring apertures. We show that the Bessel function decomposition replaces the Fourier series decomposition for linear arrays.

In Section 4.3, we develop analysis and synthesis procedures for circular apertures. These apertures correspond to the limiting case for filled circular arrays. The circular aperture also occurs in parabolic reflector antennas.

In Section 4.4, we consider arrays using a hexagonal (also called triangular) element grid. Sampling theory indicates that a hexagonal grid is the most efficient grid and hexagonal grids are widely used in various applications. Hexagonal grid arrays are closely related to rectangular grid arrays.

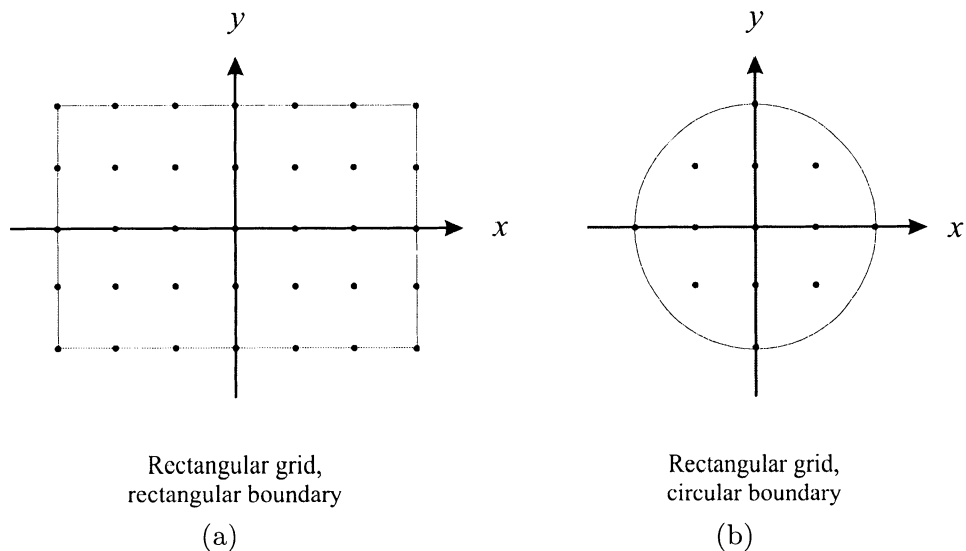


Figure 4.1 (a) Rectangular grid, rectangular boundary; (b) rectangular grid, circular boundary.

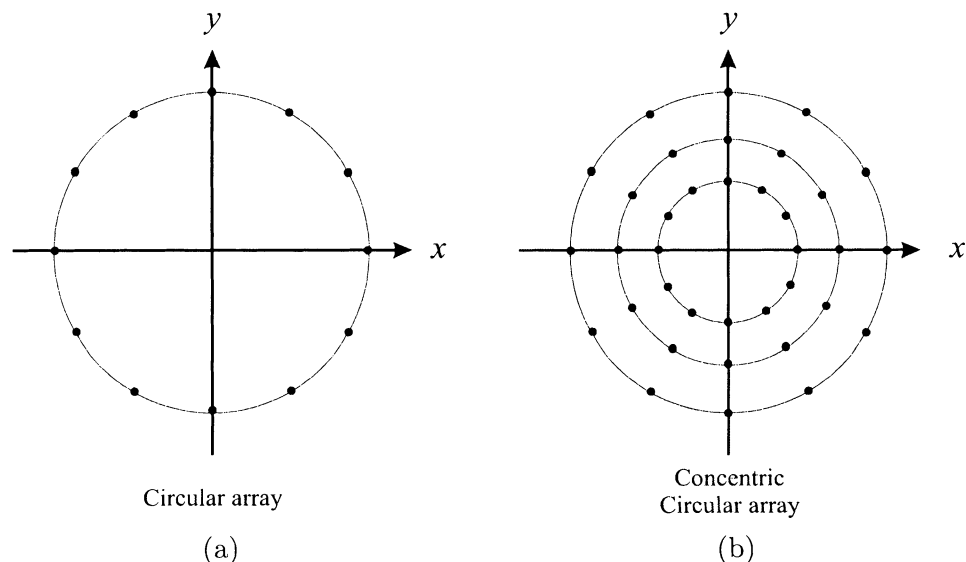


Figure 4.2 (a) Circular array; (b) concentric circular array.

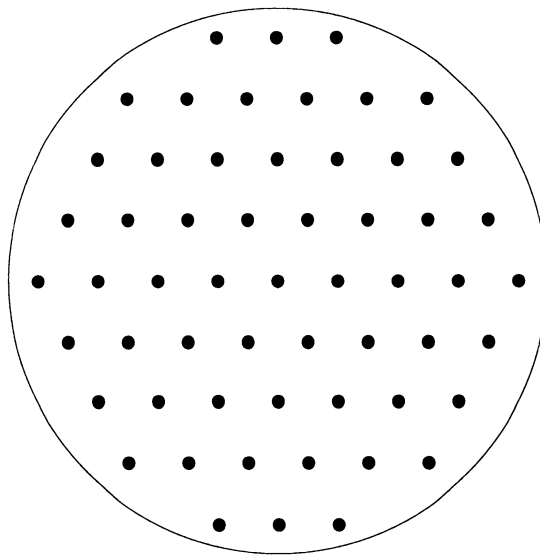


Figure 4.3 Hexagonal arrays; circular boundary.

Our development utilizes the circular aperture results in Section 4.3 which, in turn, uses the circular array results in Section 4.2. This path is the reason the two sections are separated.

In Section 4.5, we discuss nonplanar arrays briefly. In Section 4.6, we briefly summarize our results. The structure of Chapter 4 is shown in Table 4.1.

4.1 Rectangular Arrays

Our discussion of rectangular arrays parallels the development of synthesis techniques for linear arrays in Chapter 3.

4.1.1 Uniform Rectangular Arrays

The geometry for a planar array with a uniform rectangular grid and rectangular boundary is shown in Figure 4.5. We refer to these arrays as **uniform rectangular arrays** (URAs). Utilizing the relations in Chapter 3 we can write the beam pattern as the 2-D Fourier transform of the weighting function

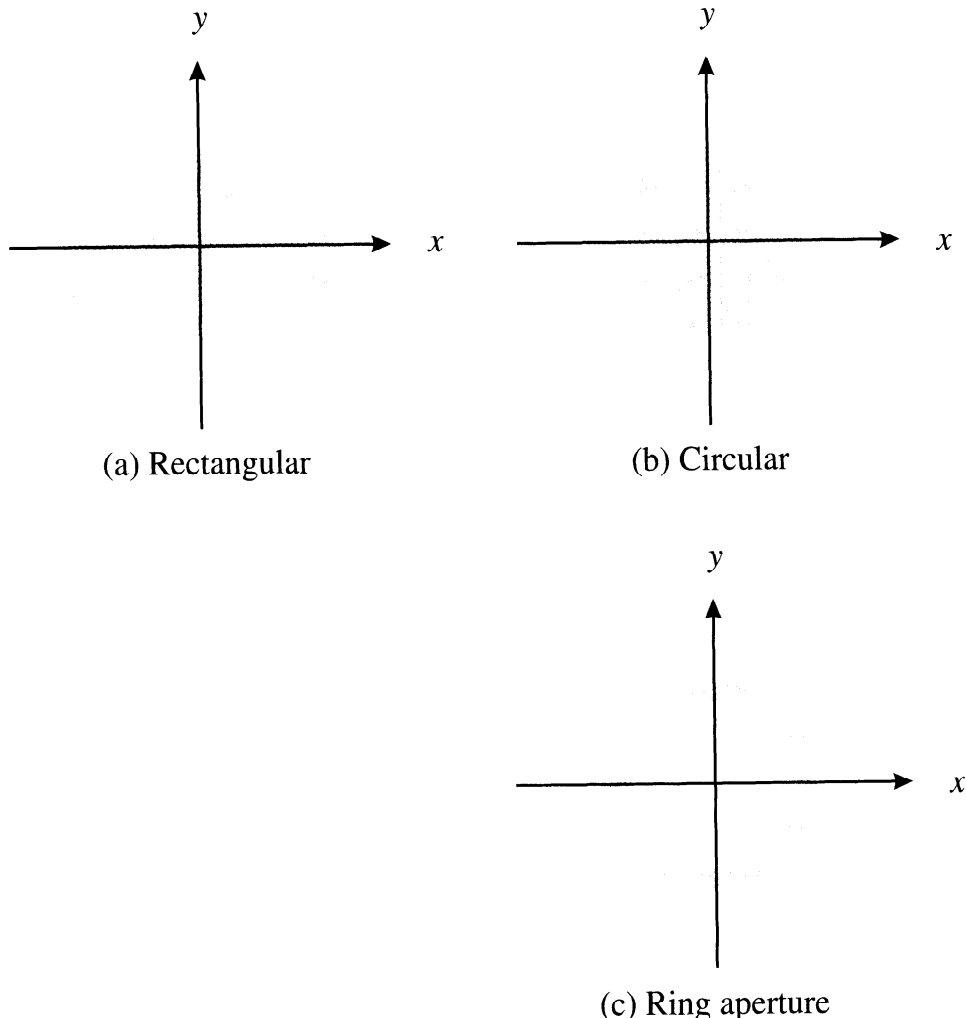


Figure 4.4 Apertures: (a) rectangular; (b) circular; (c) ring.

Table 4.1 Structure of Chapter 4.

4.1 Rectangular Rectangular grid URA, SRA Separable weighting 2-D Z-Transform Circular symmetry 2-D DIFT Chebychev	4.4 Hexagonal Triangular grid UHA SHA H-R Transformations Beamspace processing
4.2 Circular Arrays Ring aperture Circular arrays Phase mode excitation	4.3 Circular Aperture Separable weighting Taylor synthesis Sampling Difference beams
4.5 Nonplanar Arrays Cylindrical Spherical	

$$B(\psi_x, \psi_y) = e^{-j\left(\frac{N-1}{2}\psi_x + \frac{M-1}{2}\psi_y\right)} \sum_{n=0}^{N-1} \sum_{m=0}^{M-1} w_{nm}^* e^{j(n\psi_x + m\psi_y)}, \quad (4.1)$$

where

$$\psi_x = \frac{2\pi}{\lambda} d_x \sin \theta \cos \phi, \quad (4.2)$$

$$\psi_y = \frac{2\pi}{\lambda} d_y \sin \theta \sin \phi. \quad (4.3)$$

We can also express (4.2) and (4.3) in terms of the directional cosines,

$$u_x = \sin \theta \cos \phi, \quad (4.4)$$

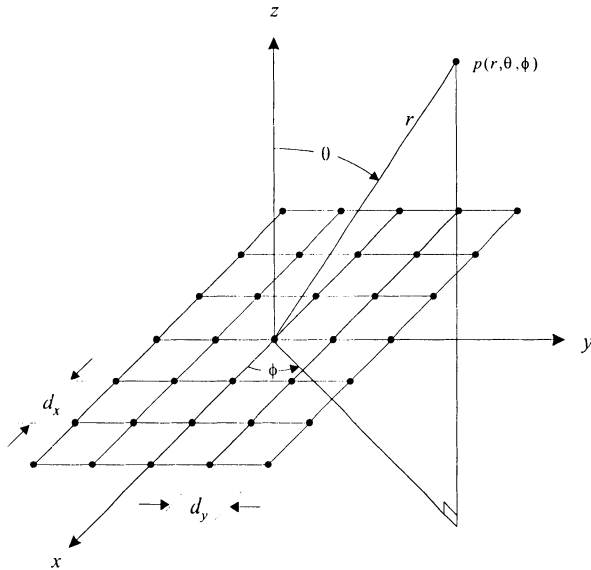


Figure 4.5 Planar array geometry.

$$u_y = \sin \theta \sin \phi. \quad (4.5)$$

The visible region is

$$u_r \triangleq \sqrt{u_x^2 + u_y^2} \leq 1. \quad (4.6)$$

In terms of ψ_x , ψ_y , the visible region is

$$\sqrt{\left(\frac{\psi_x}{d_x}\right)^2 + \left(\frac{\psi_y}{d_y}\right)^2} \leq \frac{2\pi}{\lambda}. \quad (4.7)$$

For the case in which

$$d_x = d_y = \frac{\lambda}{2}, \quad (4.8)$$

(4.2) and (4.3) reduce to

$$\psi_x = \pi u_x \quad (4.9)$$

and

$$\psi_y = \pi u_y. \quad (4.10)$$

We refer to uniform rectangular arrays that satisfy (4.8) as **standard rectangular arrays** (SRAs). We normally work in (ψ_x, ψ_y) space or (u_x, u_y) space because of the Fourier transform relationship. However, it is important

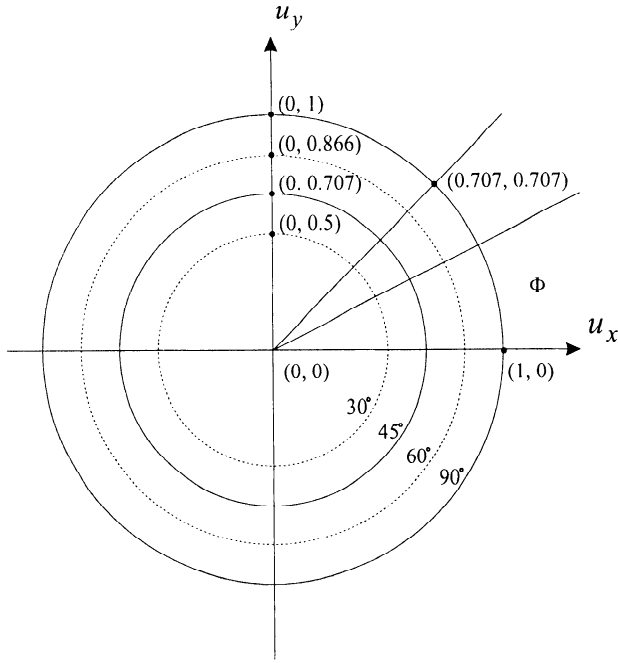


Figure 4.6 Mapping between (θ, ϕ) space and (u_x, u_y) space.

to remember the mapping into (θ, ϕ) space. This is shown in Figure 4.6 for the $d = \lambda/2$ case. The pairwise mapping $(u_x, u_y) \leftrightarrow (\theta, \phi)$ is unique.

As in the linear array case, we must consider the grating lobe structure. To do this, we rewrite (4.1) as

$$B(u_x, u_y) = e^{-j(\frac{N-1}{2}\pi u_x + \frac{M-1}{2}\pi u_y)} \sum_{m=0}^{M-1} \sum_{n=0}^{N-1} w_{nm}^* e^{j[nk_0 d_x u_x + mk_0 d_y u_y]}. \quad (4.11)$$

First, consider the case when the array is steered to broadside. Expanding (4.11) and recalling that $k_0 \triangleq |k| = 2\pi/\lambda$, we see that grating lobes will occur at

$$u_x = p \frac{\lambda}{d_x}, \quad p = 1, 2, \dots, \quad (4.12)$$

$$u_y = q \frac{\lambda}{d_y}, \quad q = 1, 2, \dots. \quad (4.13)$$

This periodicity is shown in the (u_x, u_y) plane in Figure 4.7.

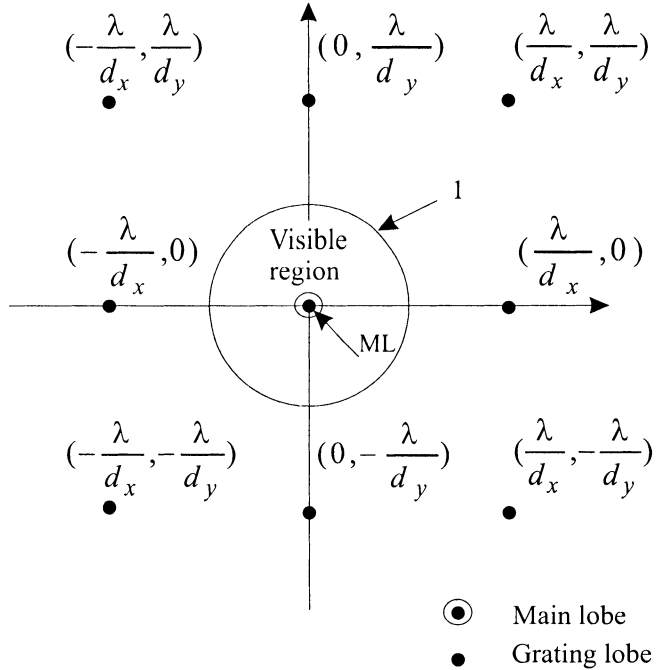


Figure 4.7 Planar array-grating lobe grid (rectangular lattice-rectangular grid).

Now assume the array is steered to (θ_0, ϕ_0) .¹ Then,

$$u_{x0} = \sin \theta_0 \cos \phi_0 \quad (4.14)$$

and

$$u_{y0} = \sin \theta_0 \sin \phi_0. \quad (4.15)$$

Also,

$$\frac{u_{y0}}{u_{x0}} = \tan \phi_0 \quad (4.16)$$

and

$$\sqrt{u_{x0}^2 + u_{y0}^2} = \sin \theta_0. \quad (4.17)$$

The location of the main beam in (u_x, u_y) space is given by (4.14) and (4.15) and is shown in Figure 4.8. The grating lobes shift along exactly the same vector as shown in Figure 4.8. We can now determine the values of d_x and d_y required to avoid grating lobes in the visible region. We illustrate the process with a simple example.

¹The subscript “0” denotes the steering direction.

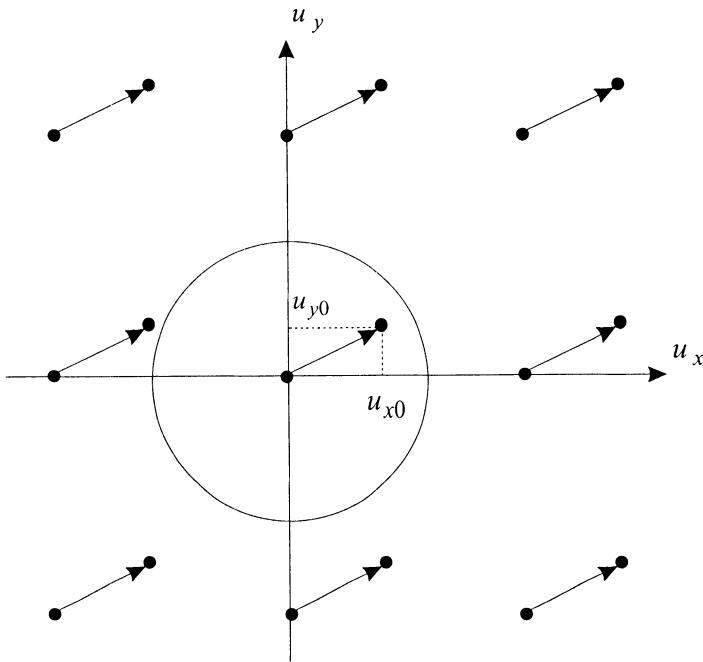


Figure 4.8 Planar array—scanned.

Example 4.1.1

Consider a rectangular grid array with uniform spacing d_x and d_y . We are required to scan from $0^\circ \leq \theta \leq 60^\circ$ and over all values of ϕ . Some possible locations of the grating lobes are shown in Figure 4.9. In the figure, we have chosen d_x and d_y so that the grating lobe is on the border of the visible region in the worst case.

Thus,

$$\frac{\lambda}{d_x} = \frac{\lambda}{d_y} = 1.866, \quad (4.18)$$

and we require,

$$d_x \leq \frac{\lambda}{1.866}, \quad (4.19)$$

and

$$d_y \leq \frac{\lambda}{1.866}. \quad (4.20)$$

If we are required to scan $0^\circ \leq \theta \leq 90^\circ$, then we require

$$d_x \leq \frac{\lambda}{2} \quad (4.21)$$

and

$$d_y \leq \frac{\lambda}{2}. \quad (4.22)$$

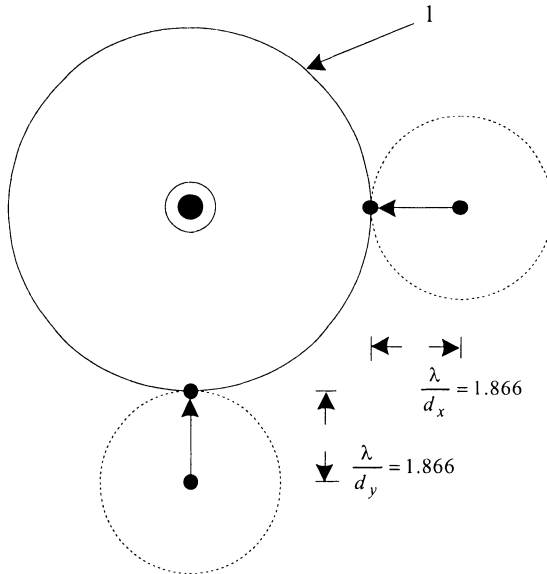


Figure 4.9 Possible locations of the grating lobes.

We will refer to a rectangular array with

$$d_x = d_y = \frac{\lambda}{2}, \quad (4.23)$$

as a standard uniform rectangular array.

For the special case in which we have separable weightings

$$w_{nm} = w_n w_m, \quad (4.24)$$

the beam pattern is the product of the two individual array factors,

$$B(\psi_x, \psi_y) = B_x(\psi_x) \cdot B_y(\psi_y). \quad (4.25)$$

If the weighting is uniform in both directions, then

$$B(\psi_x, \psi_y) = \left[\frac{1}{N} \frac{\sin\left(\frac{N}{2}\psi_x\right)}{\sin\left(\frac{\psi_x}{2}\right)} \right] \left[\frac{1}{M} \frac{\sin\left(\frac{M}{2}\psi_y\right)}{\sin\left(\frac{\psi_y}{2}\right)} \right]. \quad (4.26)$$

There are several ways to plot beam patterns for the 2-D case. We illustrate them for this case. In subsequent cases, we use the plot that is most appropriate for the particular problem. We use $M = N = 10$ in the plots.

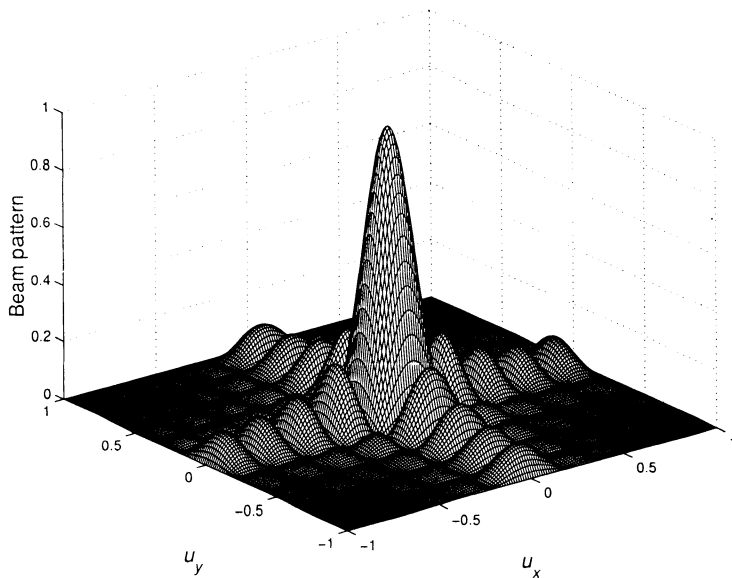


Figure 4.10 Magnitude of beam pattern of standard rectangular array: $N = M = 10$, uniform weighting, linear vertical scale.

- (i) In Figure 4.10, we show the amplitude of the beam pattern versus u_x and u_y with a linear vertical scale. In Figure 4.11, we show the amplitude of the beam pattern versus u_x and u_y on a logarithmic scale. Both of these give a good overall view of the pattern but are not convenient for examining the details of the main lobe and sidelobe behavior.
- (ii) In Figure 4.12, we show polar plots of the amplitude of the beam pattern versus θ for various values of ϕ . These plots are vertical cuts through the 3-D beam pattern. Note that the right side of the polar plot corresponds to the indicated value of ϕ . The left side corresponds to $\phi + 180^\circ$. In Figure 4.13, we plot the amplitude on a logarithmic scale versus $u_r = \sin \theta$ for various values of ϕ . These plots are referred to as pattern cuts and are generally the most useful for a detailed pattern analysis.
- (iii) In Figure 4.14, we show a contour plot of the amplitude in dB versus u_x and u_y . This plot gives a good view of the pattern symmetries and is particularly useful when plotted in color.

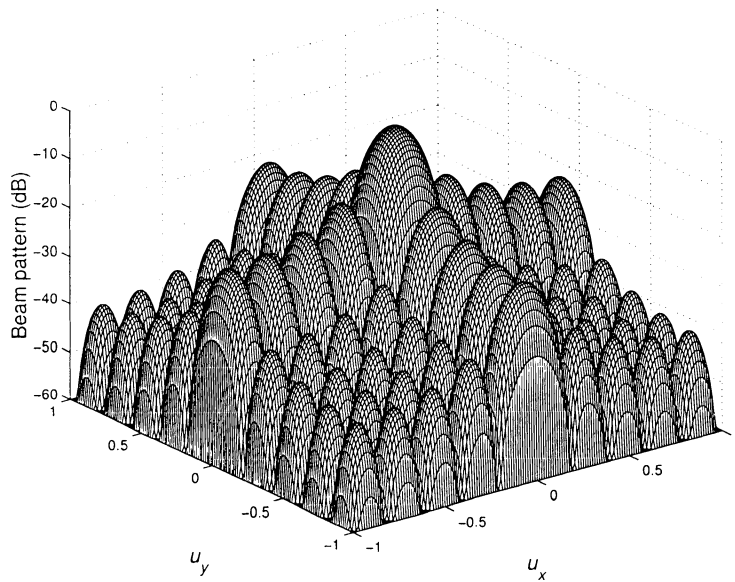


Figure 4.11 Magnitude of beam pattern of standard rectangular array: $N = M = 10$, uniform weighting, vertical scale is $20 \log |B_u(u)|$.

4.1.1.1 Beamwidth

The half-power beamwidth for a pattern array is a contour in (u_x, u_y) space or (θ, ϕ) space where the magnitude-squared of the beam pattern is 0.5. For general weights, this contour must be evaluated analytically.

In some cases, the weights are chosen so that when the array is steered to broadside, the 3-dB contour can be approximated by a circle if $M = N$ and an ellipse if $M \neq N$. In these cases, an approximate expression for the axes of the half-power ellipse can be used.

The beamshape versus scan angle is shown in Figure 4.15. As the MRA of the beam moves away from $\theta = 0$, the circular contour becomes elliptical and the beamwidth in the θ -direction increases.

Two planes are chosen to characterize the beamwidth. The first is the elevation plane corresponding to $\phi = \phi_0$ and the second is a plane perpendicular to it. The half-power beamwidths in the two planes are designated by θ_H and Ψ_H . For a large array steered near broadside, θ_H is given approximately by

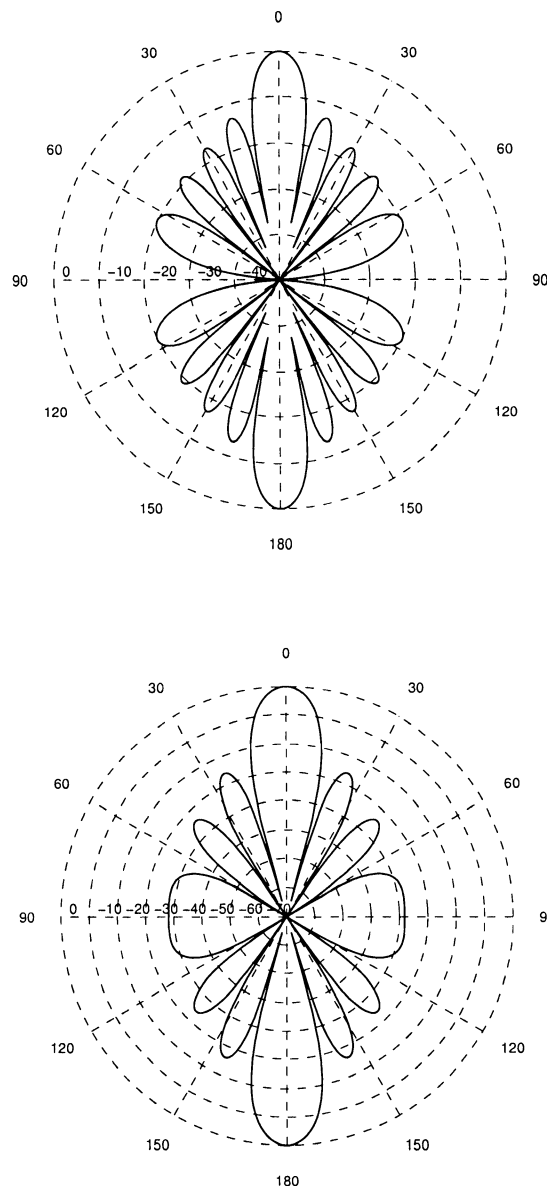


Figure 4.12 Polar plot of beam pattern cut of standard rectangular array:
 $N = M = 10$, uniform weighting; (a) $\phi = 0^\circ$ or 90° ; (b) $\phi = 45^\circ$.

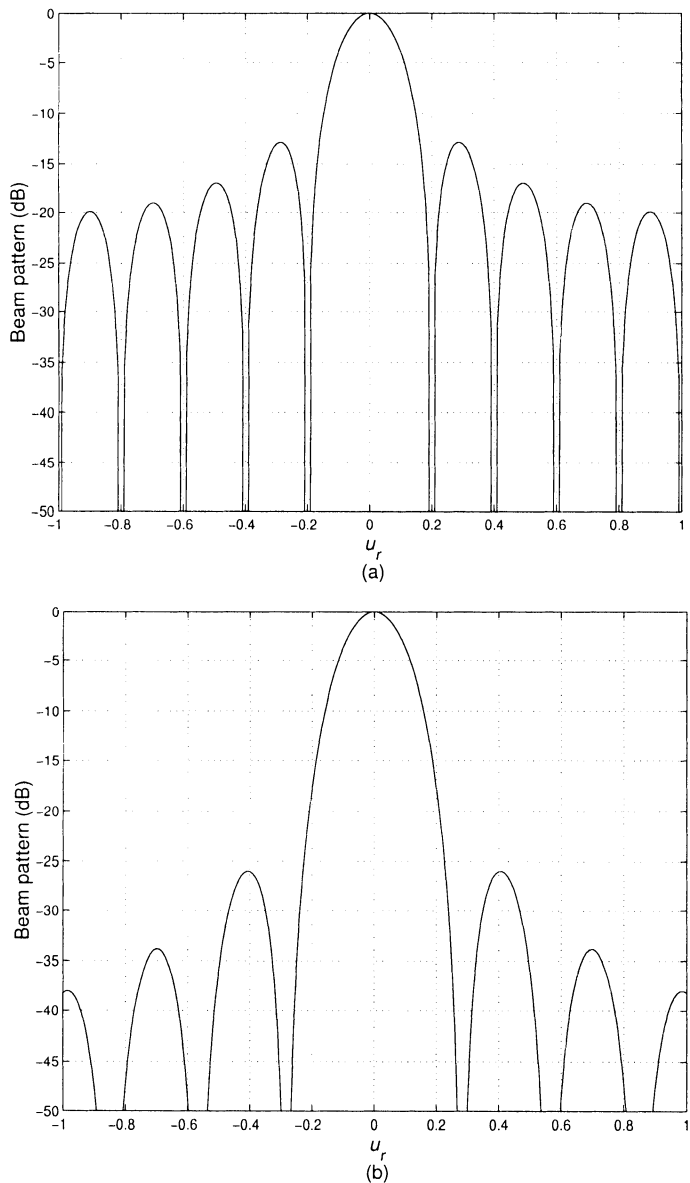


Figure 4.13 Beam pattern cut of standard rectangular array: $N = M = 10$, uniform weighting, plotted versus u_r ; (a) $\phi = 0^\circ$ or 90° ; (b) $\phi = 45^\circ$.

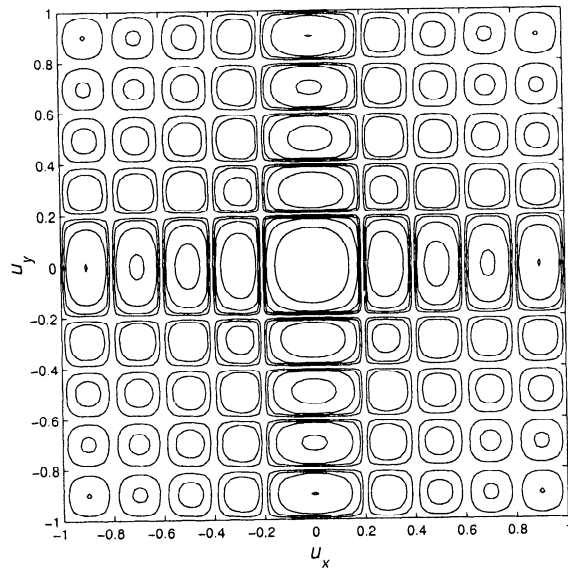


Figure 4.14 Contour plot of magnitude of beam pattern for standard rectangular array: $N = M = 10$, uniform weighting.

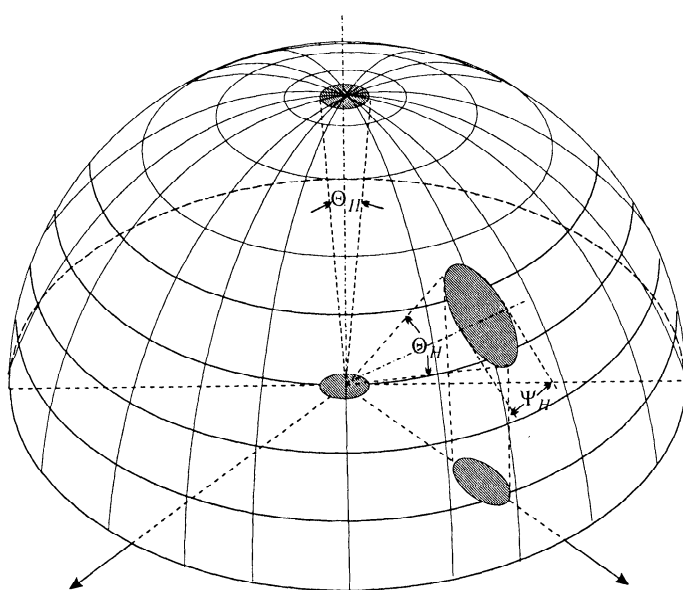


Figure 4.15 Beam shape versus scan angle.

$$\theta_H = \sqrt{\frac{1}{\cos^2\theta_0 \left[\theta_{x0}^{-2} \cos^2\phi_0 + \theta_{y0}^{-2} \sin^2\phi_0 \right]}}, \quad (4.27)$$

where

- (i) θ_{x0} is the HPBW of a broadside linear array with N elements;
- (ii) θ_{y0} is the HPBW of a broadside linear array with M elements (e.g., Elliot [Ell64] or Problem 4.1.1).

The HPBW values are obtained from our previous linear array beamwidth results in Chapter 3.

For a square array with equal separable weightings,

$$\theta_H = \theta_{x0} \sec\theta_0 = \theta_{y0} \sec\theta_0, \quad (4.28)$$

which is identical to our result in Chapter 2.

The HPBW in the perpendicular plane is given by

$$\Psi_H = \sqrt{\frac{1}{\theta_{x0}^{-2} \sin^2\phi_0 + \theta_{y0}^{-2} \cos^2\phi_0}} \quad (4.29)$$

(e.g., Elliot [Ell64] or Problem 4.1.2). Note that it does not depend on θ_0 . For a square array with equal separable weightings

$$\Psi_H = \theta_{x0} = \theta_{y0}. \quad (4.30)$$

The beam solid angle Ω_A is the product of the HPBWs,

$$\Omega_A = \theta_H \Psi_H, \quad (4.31)$$

which can be expressed as

$$\Omega_A = \frac{\theta_{x0} \theta_{y0} \sec\theta_0}{\left[\sin^2\phi_0 + \frac{\theta_{y0}^2}{\theta_{x0}^2} \cos^2\phi_0 \right]^{1/2} \left[\sin^2\phi_0 + \frac{\theta_{x0}^2}{\theta_{y0}^2} \cos^2\phi_0 \right]^{1/2}}. \quad (4.32)$$

The expression in (4.32) is useful. However, in most examples we plot the actual half-power contour of the beam pattern in the u_x, u_y plane or examine it for various pattern cuts.

4.1.1.2 Directivity of a planar array

The directivity of an array is given by (2.144) as

$$D = \frac{|B(\theta_0, \phi_0)|^2}{\frac{1}{4\pi} \int_0^{2\pi} \int_0^\pi |B(\theta, \phi)|^2 \sin \theta d\theta d\phi}, \quad (4.33)$$

where (θ_0, ϕ_0) is the MRA. We desire an expression for the directivity that is valid for any planar array in the xy -plane. The directivity does not depend on the choice of the coordinate system, so the result is valid for any planar array.

For an N -element planar array in the xy -plane, we denote the position of the n th element by (p_{x_n}, p_{y_n}) . Note that the array can have arbitrary configuration in the xy -plane and that we are indexing the elements with a single index n . Note that N is the total number of elements and would equal NM for the array in Figure 4.5.

The beam pattern can be written as,

$$B(\theta, \phi) = \sum_{n=0}^{N-1} w_n^* \exp \left(j \frac{2\pi}{\lambda} (p_{x_n} \sin \theta \cos \phi + p_{y_n} \sin \theta \sin \phi) \right). \quad (4.34)$$

The denominator in (4.33) can be written as

$$\begin{aligned} DEN &\triangleq \frac{1}{4\pi} \int_0^{2\pi} \int_0^\pi |B(\theta, \phi)|^2 \sin \theta d\theta d\phi \\ &= \frac{1}{4\pi} \int_0^{2\pi} \int_0^\pi \sum_{n=0}^{N-1} \sum_{m=0}^{N-1} w_n^* w_m e^{j \frac{2\pi}{\lambda} \sin \theta [(p_{x_n} - p_{x_m}) \cos \phi + (p_{y_n} - p_{y_m}) \sin \phi]} \\ &\quad \cdot \sin \theta d\theta d\phi, \end{aligned} \quad (4.35)$$

which reduces to

$$\begin{aligned} DEN &= \sum_{n=0}^{N-1} \sum_{m=0}^{N-1} w_n^* w_m \int_0^\pi \frac{1}{2} \sin \theta \cdot d\theta \int_0^{2\pi} \frac{1}{2\pi} \\ &\quad \cdot \exp \left(j \frac{2\pi}{\lambda} \sin \theta (\Delta p_{x_{nm}} \cos \phi + \Delta p_{y_{nm}} \sin \phi) \right) d\phi, \end{aligned} \quad (4.36)$$

where

$$\Delta p_{x_{nm}} \triangleq p_{x_n} - p_{x_m}, \quad (4.37)$$

and

$$\Delta p_{y_{nm}} \triangleq p_{y_n} - p_{y_m}. \quad (4.38)$$

Now define

$$\rho_{nm} = \left((\Delta p_{x_{nm}})^2 + (\Delta p_{y_{nm}})^2 \right)^{\frac{1}{2}} = \|\Delta \mathbf{p}_{nm}\|, \quad (4.39)$$

and

$$\phi_{nm} = \arctan \left(\frac{\Delta p_{y_{nm}}}{\Delta p_{x_{nm}}} \right). \quad (4.40)$$

Then

$$\Delta p_{x_{nm}} = \rho_{nm} \cos \phi_{nm}, \quad (4.41)$$

and

$$\Delta p_{y_{nm}} = \rho_{nm} \sin \phi_{nm}. \quad (4.42)$$

Using (4.41) and (4.42) in the inner integral in (4.36) gives

$$\begin{aligned} & \int_0^{2\pi} \frac{1}{2\pi} \exp \left(j \frac{2\pi}{\lambda} \rho_{nm} \sin \theta (\cos \phi \cos \phi_{nm} + \sin \phi \sin \phi_{nm}) \right) d\phi \\ &= \int_0^{2\pi} \frac{1}{2\pi} \exp \left(j \frac{2\pi}{\lambda} \rho_{nm} \sin \theta (\cos(\phi - \phi_{nm})) \right) d\phi \\ &= J_0 \left(\frac{2\pi}{\lambda} \rho_{nm} \sin \theta \right), \end{aligned} \quad (4.43)$$

where $J_0(\cdot)$ is a Bessel function of order zero. Substituting (4.43) into (4.36) gives

$$\begin{aligned} DEN &= \sum_{n=0}^{N-1} \sum_{m=0}^{N-1} w_n w_m^* \int_0^\pi \frac{1}{2} \sin \theta \cdot J_0 \left(\frac{2\pi}{\lambda} \rho_{nm} \sin \theta \right) d\theta \\ &= \sum_{n=0}^{N-1} \sum_{m=0}^{N-1} w_n w_m^* \text{sinc} \left(\frac{2\pi}{\lambda} \rho_{nm} \right). \end{aligned} \quad (4.44)$$

Defining a matrix \mathbf{B} with elements

$$[\mathbf{B}]_{nm} = \text{sinc} \left(\frac{2\pi}{\lambda} \rho_{nm} \right), \quad (4.45)$$

the directivity can be written as

$$D = \frac{|\mathbf{w}^H \mathbf{v}_0|^2}{\mathbf{w}^H \mathbf{B} \mathbf{w}},$$

(4.46)

where

$$\mathbf{v}_0 = \mathbf{v}(\theta_0, \phi_0), \quad (4.47)$$

is the array manifold vector steered at (θ_0, ϕ_0) .

If we normalize the weights so that $B(\theta_0, \phi_0) = 1$, then (4.46) reduces to

$$D = [\mathbf{w}^H \mathbf{B} \mathbf{w}]^{-1}. \quad (4.48)$$

Note that \mathbf{B} does not reduce to an identity matrix for a standard rectangular array.

For large rectangular grid planar arrays Elliot [Ell64] has shown that

$$D_0 = \pi \cos \theta_0 D_x D_y. \quad (4.49)$$

The reader is referred to that reference for a discussion of this result. We will use the result in (4.46) to calculate the directivity.

In the linear array we developed a number of techniques for synthesizing desireable beam patterns. In the next several sections, we look at the extension of these techniques to planar arrays and the introduction of modified techniques where appropriate. Before doing that development, it is useful to consider the array manifold vector in more detail.

4.1.2 Array Manifold Vector

The array manifold vector was defined for an arbitrary array in (2.28). For rectangular planar arrays it is convenient to define an array manifold matrix as an intermediate step.

We define

$$\mathbf{v}_m(\psi) = \begin{bmatrix} e^{jm\psi_y} \\ e^{j(\psi_x+m\psi_y)} \\ \vdots \\ e^{j((N-1)\psi_x+m\psi_y)} \end{bmatrix}, \quad (4.50)$$

as the array manifold vector corresponding to the m th line of sensors in the y -direction. The vector ψ is

$$\psi = \begin{bmatrix} \psi_x \\ \psi_y \end{bmatrix}. \quad (4.51)$$

Then,

$$\mathbf{V}_\psi(\psi) = [\mathbf{v}_0(\psi) \mid \cdots \mid \mathbf{v}_{M-1}(\psi)], \quad (4.52)$$

is an $N \times M$ array manifold matrix. Then, we can define a vector that is obtained by stacking the vectors to obtain an $NM \times 1$ vector (see (A.106)),

$$vec[\mathbf{V}_\psi(\psi)] = \begin{bmatrix} \mathbf{v}_0(\psi) \\ \vdots \\ \mathbf{v}_{M-1}(\psi) \end{bmatrix}. \quad (4.53)$$

It is easy to verify that $\text{vec} [\mathbf{v}_\psi(\psi)]$ is conjugate symmetric.

The expression in 4.53 can also be written as a Kronecker product (A.79):

$$\text{vec} [\mathbf{V}_\psi(\psi)] = \mathbf{v}(\psi) \otimes \mathbf{v}(\psi). \quad (4.54)$$

We can describe the weight vector using this notation. The weight vector down the m th line is

$$\mathbf{w}_m = \begin{bmatrix} w_{0,m} \\ \vdots \\ w_{n,m} \\ \vdots \\ w_{N-1,m} \end{bmatrix}, \quad (4.55)$$

and the weight matrix is

$$\mathbf{W} = \begin{bmatrix} \mathbf{w}_0 & \cdots & \mathbf{w}_m & \cdots & \mathbf{w}_{M-1} \end{bmatrix}, \quad (4.56)$$

and

$$\text{vec} [\mathbf{W}] = \begin{bmatrix} \mathbf{w}_0 \\ \vdots \\ \mathbf{w}_m \\ \vdots \\ \mathbf{w}_{M-1} \end{bmatrix}. \quad (4.57)$$

Then,

$$B(\psi) = B(\psi_x, \psi_y) = \text{vec}^H [\mathbf{W}] \text{vec} [\mathbf{V}_\psi(\psi)]. \quad (4.58)$$

If $\text{vec} [\mathbf{W}]$ is conjugate symmetric (or real and symmetric), then $B(\psi)$ will be real.

For a conventional delay-and-sum beamformer,

$$\text{vec}^H [\mathbf{W}] = \text{vec}^H [\mathbf{V}_{\psi_s}(\psi_s)], \quad (4.59)$$

and

$$B_c(\psi) = \text{vec}^H [\mathbf{V}_{\psi_s}(\psi_s)] \text{vec} [\mathbf{V}_\psi(\psi)] \quad (4.60)$$

is real.

We will find the $\text{vec}(\cdot)$ notation useful in a number of cases later in the text.

4.1.3 Separable Spectral Weightings

In Section 3.1, we introduced various spectral weightings to obtain desirable sidelobe patterns and acceptable main-lobe beamwidths.

A straightforward approach is to use the linear array spectral weighting along each axis:

$$w_{nm} = w_n w_m. \quad (4.61)$$

Since the weighting is separable, the beam pattern will be a product of the two linear array beam patterns. Then,

$$B(\psi_x, \psi_y) = B(\psi_x) B(\psi_y). \quad (4.62)$$

In many cases, this will lead to satisfactory patterns. The problem is that it is not clear how the two-dimensional pattern will behave when $\phi \neq 0$ or $\pi/2$. For example, we saw in Figure 4.13 that the sidelobe structure for $\phi = \pi/4$ was significantly different than that for $\phi = 0$ or $\pi/2$.

We consider an example to illustrate the behavior.

Example 4.1.2: Hamming window

We assume that $M = N = 11$ and use the Hamming weighting from (3.21):

$$w_N(n) = \begin{cases} 0.54 + 0.46 \cos\left(\frac{2\pi|n|}{N}\right), & |n| \leq 5, \\ 0, & \text{elsewhere.} \end{cases} \quad (4.63)$$

The resulting pattern is shown in Figure 4.16. In Figure 4.17, we show pattern cuts at $\phi = 0^\circ$ (or 90°) and $\phi = 45^\circ$. We see that the main lobe is wider for $\phi = 0^\circ$ (or 90°). The sidelobes are lower for $\phi = 45^\circ$ than for $\phi = 0^\circ$ (or 90°).

This behavior is typical for separable weightings. In order to obtain beam patterns whose pattern cuts are similar for all ϕ , non-separable weightings are required.

4.1.4 2-D z-Transforms

Just as in the 1-D case, we can write the z -transform of the weighting matrix as

$$B_z(z_1, z_2) = \sum_{n=0}^{N-1} \sum_{m=0}^{M-1} w_{nm} z_1^{-n} z_2^{-m}. \quad (4.64)$$

We define

$$z_1 = e^{j\psi_x}, \quad (4.65)$$

and

$$z_2 = e^{j\psi_y}. \quad (4.66)$$

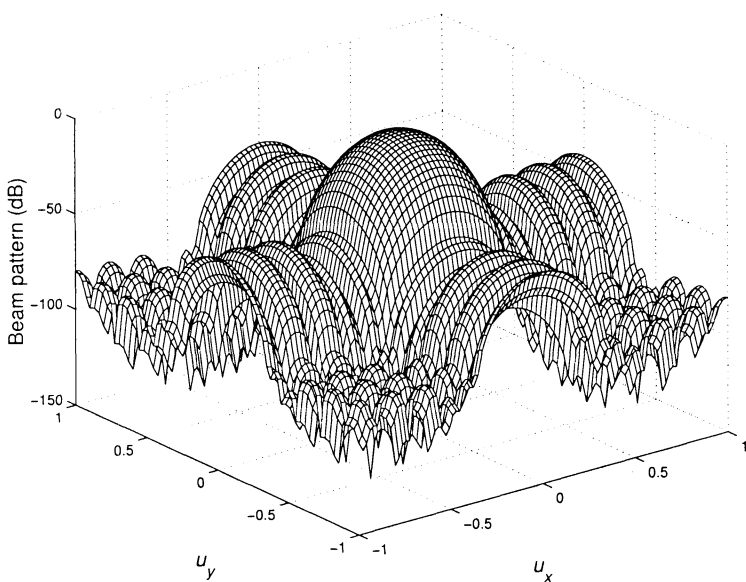


Figure 4.16 Beam pattern: separable Hamming weighting.

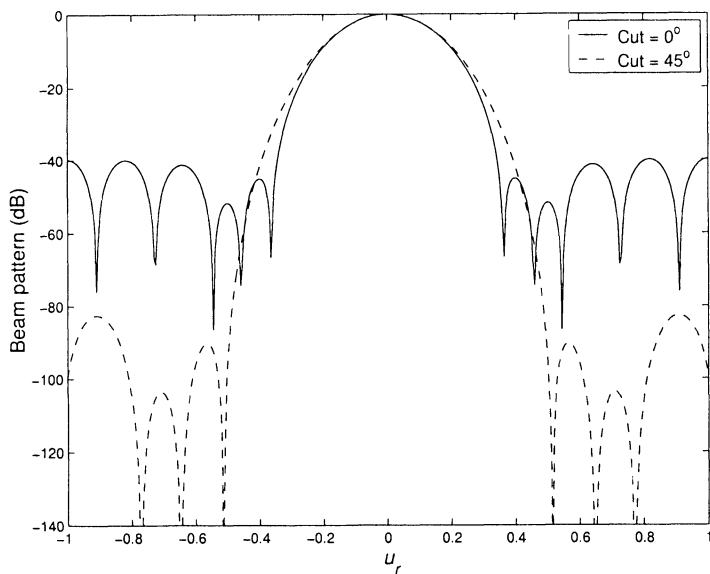


Figure 4.17 Beam pattern cuts: separable Hamming weighting.

The beam pattern can be written as

$$B_{\psi}(\psi_x, \psi_y) = \left[z_1^{-\frac{N-1}{2}} z_2^{-\frac{M-1}{2}} B_{\mathbf{z}}^*(z_1, z_2) \right]_{z_1=e^{j\psi_x}, z_2=e^{j\psi_y}} . \quad (4.67)$$

4.1.5 Least Squares Synthesis

In this section, we apply the least squares results in Section 3.5 to planar arrays. The square error can be written as

$$\xi = \frac{1}{4\pi} \int_0^{2\pi} \int_0^\pi |B_d(\theta, \phi) - \sum_{m=0}^{M-1} \mathbf{w}_m^H \mathbf{v}_m(\theta, \phi)|^2 \sin \theta d\theta d\phi \quad (4.68)$$

Differentiating with respect to \mathbf{w}_m^H and setting the result equal to $\mathbf{0}$ gives,²

$$\mathbf{w}_{m,o} = \frac{1}{4\pi} \mathbf{A}_m^{-1} \int_0^{2\pi} \int_0^\pi \mathbf{v}_m(\theta, \phi) B_d^*(\theta, \phi) \sin \theta d\theta d\phi, \quad m = 0, \dots, M-1, \quad (4.69)$$

where

$$\mathbf{A}_m = \frac{1}{4\pi} \int_0^{2\pi} \int_0^\pi \mathbf{v}_m(\theta, \phi) \mathbf{v}_m^H(\theta, \phi) \sin \theta d\theta d\phi, \quad m = 0, \dots, M-1 \quad (4.70)$$

is an $N \times N$ matrix. From (4.50), we observe that

$$\mathbf{v}_m(\psi_x, \psi_y) \mathbf{v}_m^H(\psi_x, \psi_y) = \mathbf{v}_m(\theta, \phi) \mathbf{v}_m^H(\theta, \phi) \quad (4.71)$$

is not a function of m so the subscript can be removed from the left side of (4.70). Evaluating (4.70) gives:

$$[\mathbf{A}]_{nl} = \text{sinc}[(n-l)] = \pi \delta_{nl} \quad (4.72)$$

for a standard rectangular grid. Thus,

$$\mathbf{w}_{m,o} = \frac{1}{4\pi^2} \int_0^{2\pi} \int_0^\pi \mathbf{v}_m(\theta, \phi) B_d^*(\theta, \phi) \sin \theta d\theta d\phi. \quad (4.73)$$

We consider two examples to illustrate typical behavior.

Example 4.1.3

The desired beam pattern is shown in Figure 4.18.

²This approach is the same as Section 3.5.

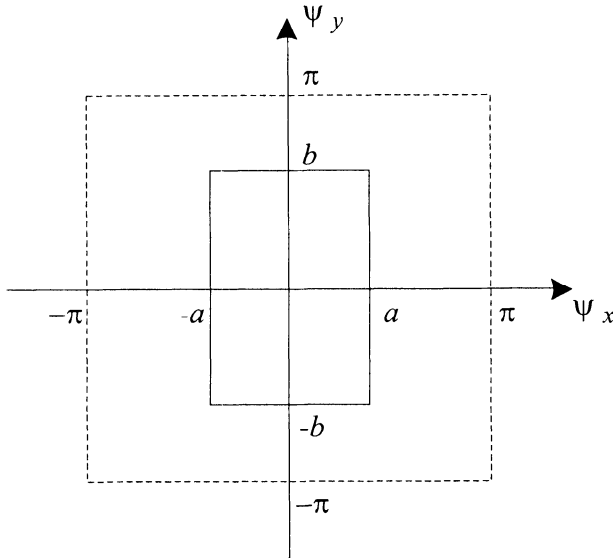


Figure 4.18 Ideal rectangular wavenumber beam pattern.

$$B_{\psi}(\psi_x, \psi_y) = \begin{cases} 1, & -\psi_a \leq \psi_x \leq \psi_a; -\psi_b \leq \psi_y \leq \psi_b, \\ 0, & \text{elsewhere.} \end{cases} \quad (4.74)$$

The limits of the integrand are completely inside the visible region so that we can use rectangular coordinates. The n th component of $\mathbf{w}_{m,o}$ is

$$\begin{aligned} [\mathbf{w}_{m,o}]_n = \frac{1}{4\pi^2} \int_{-\psi_a}^{\psi_a} \int_{-\psi_b}^{\psi_b} \exp \left\{ j \left[\left(n - \frac{N-1}{2} \right) \psi_x + \left(m - \frac{M-1}{2} \right) \psi_y \right] \right\} d\psi_x d\psi_y \\ n = 0, \dots, N-1, \\ m = 0, \dots, M-1. \end{aligned} \quad (4.75)$$

Integrating gives

$$\begin{aligned} [\mathbf{w}_{m,o}]_n = \left(\frac{\sin \left(\left(n - \frac{N-1}{2} \right) \psi_a \right)}{\left(n - \frac{N-1}{2} \right) \pi} \right) \left(\frac{\sin \left(\left(m - \frac{M-1}{2} \right) \psi_b \right)}{\left(m - \frac{M-1}{2} \right) \pi} \right) \\ n = 0, \dots, N-1, \\ m = 0, \dots, M-1. \end{aligned} \quad (4.76)$$

which is a separable weighting. The weight is real, so $[\mathbf{w}_{m,o}]_n = [\mathbf{w}_{m,o}^*]_n$.

The resulting beam pattern for $N = M = 11$ is a product of the uniform beam pattern in Figure 3.32 with a uniform beam pattern of identical shape (with $\psi_a \neq \psi_b$). As expected, we have an overshoot because of the Gibbs phenomenon.

Just as in the 1-D case, we can alleviate the overshoot problem by using one of the windows discussed in Section 3.1. For example, if we use the

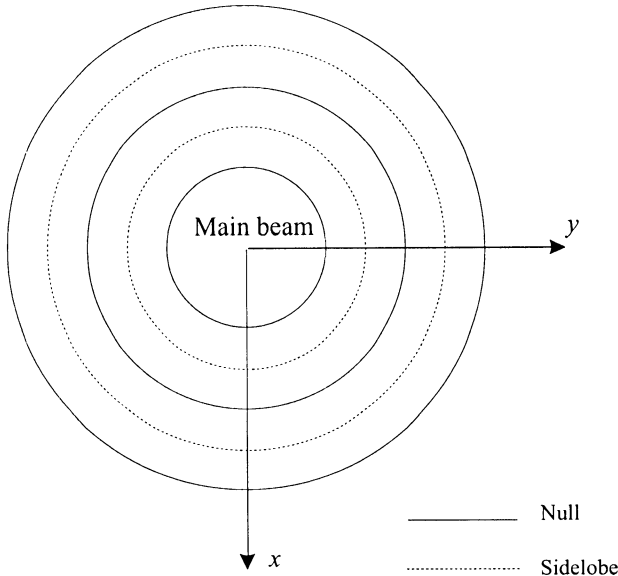


Figure 4.19 Ring-type sidelobe structure of ϕ -symmetric pattern.

Kaiser window from Example 3.4.3, the resulting pattern will be a product of the beam pattern in Figure 3.33 with itself when $\psi_a = \psi_b$.

In a large number of applications, we would like the beam pattern to be uniform in ϕ . This corresponds to circular symmetry in (ψ_x, ψ_y) space. This implies,

$$B_{\psi}(\psi_x, \psi_y) = B_{\psi_r}(\sqrt{\psi_x^2 + \psi_y^2}). \quad (4.77)$$

The argument of the function on the right side corresponds to the radial wavenumber,

$$\psi_r = \sqrt{\psi_x^2 + \psi_y^2}. \quad (4.78)$$

Beam patterns satisfying (4.77) will have a ring sidelobe structure, as shown in Figure 4.19, and will lead to a non-separable weighting function.

Example 4.1.4³

The simplest case corresponds to a desired beam pattern that is constant over a circular region, as shown in Figure 4.20.

In this case, it is useful to use symmetric indexing. Then, for N odd,

$$B_{\psi}(\psi_x, \psi_y) = \sum_{n=-\frac{N-1}{2}}^{\frac{N-1}{2}} \sum_{m=-\frac{M-1}{2}}^{\frac{M-1}{2}} a_{nm}^* e^{j(n\psi_x + m\psi_y)}, \quad (4.79)$$

³This example is on p. 446 of [RG75].

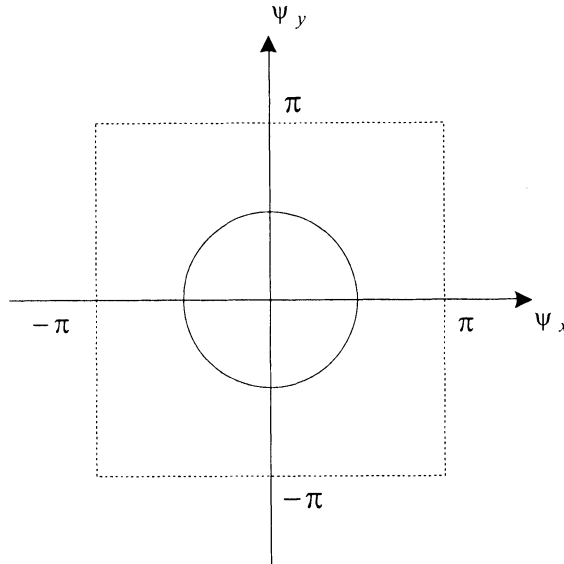


Figure 4.20 Desired beam pattern: circular symmetry.

and, for N even,

$$B_{\psi}(\psi_x, \psi_y) = \sum_{\substack{n=-\frac{N}{2} \\ n \neq 0}}^{\frac{N}{2}} \sum_{\substack{m=-\frac{M}{2} \\ m \neq 0}}^{\frac{M}{2}} a_{nm}^* e^{j(n\psi_x + m\psi_y)}. \quad (4.80)$$

The weight is denoted by a_{nm}^* when symmetric indexing is used.

Since the beam pattern has circular symmetry, the weighting function will have circular symmetry.

$$a^*(n, m) = a_c^* \left(\sqrt{n^2 + m^2} \right). \quad (4.81)$$

A simple way to find $a^*(n, m)$ is to first find $a^*(n, 0)$ and then replace n by $\sqrt{n^2 + m^2}$:

$$\begin{aligned} a^*(n, 0) &= \frac{1}{4\pi^2} \int_{-\psi_R}^{\psi_R} e^{jn\psi_x} d\psi_x \int_{-\sqrt{\psi_R^2 - \psi_x^2}}^{\sqrt{\psi_R^2 - \psi_x^2}} d\psi_y \\ &= \frac{1}{4\pi^2} \int_{-\psi_R}^{\psi_R} e^{jn\psi_x} \left[2\sqrt{\psi_R^2 - \psi_x^2} \right] d\psi_x. \end{aligned} \quad (4.82)$$

Letting,

$$\psi_x = \psi_R \sin \varphi, \quad (4.83)$$

where

$$\varphi = \tan^{-1} \left(\frac{\psi_x}{\psi_y} \right). \quad (4.84)$$

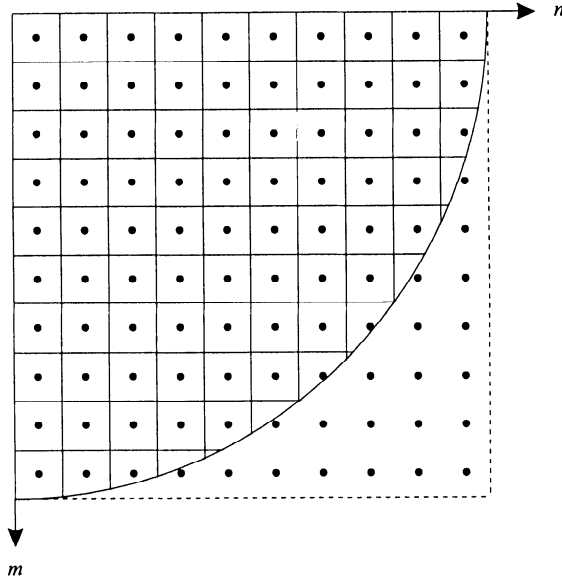


Figure 4.21 One quadrant of a rectangular array: $d_x = d_y = 0.5\lambda$.

Then

$$d\psi_x = \psi_R \cos \varphi d\varphi, \quad (4.85)$$

and

$$\begin{aligned} a^*(n, 0) &= \frac{1}{4\pi^2} \int_{-\frac{\pi}{2}}^{\frac{\pi}{2}} 2\psi_R^2 (\cos^2 \varphi) e^{j\psi_R n \sin \varphi} d\varphi \\ &= \frac{\psi_R J_1(\psi_R n)}{2\pi n}, \end{aligned} \quad (4.86)$$

where $J_1(\cdot)$ is the first-order Bessel function. In (4.86), n is treated as a continuous variable. Then

$$a^*(n, m) = \frac{\psi_R J_1(\psi_R \sqrt{n^2 + m^2})}{2\pi \sqrt{n^2 + m^2}}. \quad (4.87)$$

Now consider a square array with N elements in each direction. One quadrant of a square array with $N = 20$ is shown in Figure 4.21. We consider two ways of truncating $a^*(n, m)$ in (4.86).

The first choice is to let

$$a^*(n, m) = \begin{cases} a^*(\sqrt{n^2 + m^2}), & 0 \leq \sqrt{n^2 + m^2} \leq 10, \\ 0, & \text{elsewhere.} \end{cases} \quad (4.88)$$

The effect of (4.88) is to give the square array a circular boundary as shown in Figure 4.21. All of the elements outside of the circular boundary have zero weights.

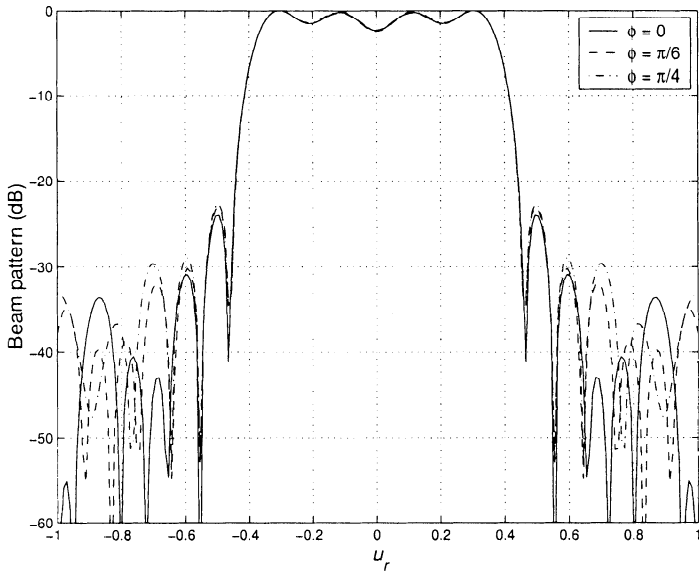


Figure 4.22 Beam pattern cut: standard rectangular grid array with circular boundary: $N = M = 10$, $\psi_R = 0.4\pi$, $\sqrt{n^2 + m^2} \leq 10$, $\phi = 0^\circ, 30^\circ$, and 45° .

The second choice is to let

$$a^*(n, m) = \begin{cases} a^*(\sqrt{n^2 + m^2}), & 0 \leq |n| \leq 10, 0 \leq |m| \leq 10, \\ 0, & \text{elsewhere.} \end{cases} \quad (4.89)$$

In this case, all of the elements have non-zero weights. To illustrate the effect of the two boundaries, we consider the case in which $\psi_R^2 = (0.4\pi)^2$. Then,

$$a^*(n, m) = \frac{0.4\pi J_1(0.4\pi \sqrt{n^2 + m^2})}{2\pi\sqrt{n^2 + m^2}}. \quad (4.90)$$

Beam pattern cuts at $\phi = 0, 30^\circ$, and 45° are shown in Figure 4.22 for case 1 and in Figure 4.23 for case 2. We see that using non-zero weights for all of the elements provides better sidelobe behavior. It gives a closer approximation to circular symmetry for the sidelobes but slightly less main-lobe symmetry.

The cuts show the same Gibbs phenomenon as in the one-dimensional case. This leads us to the topic of circularly symmetric windows and circularly symmetric weightings.

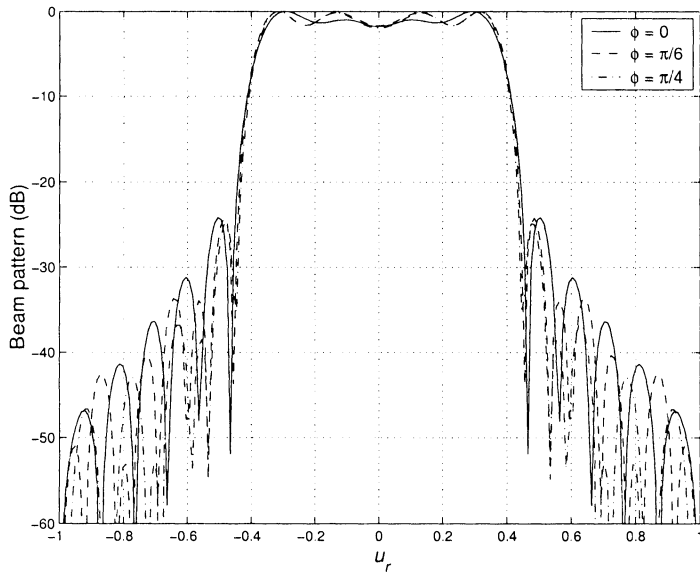


Figure 4.23 Beam pattern cut: standard rectangular grid array with square boundary: $N = M = 10$, $\psi_R = 0.4\pi$, $n \leq 10$, $m \leq 10$, $\phi = 0^\circ$, 30° , and 45° .

4.1.6 Circularly Symmetric Weighting and Windows

In Section 3.1, we developed a set of spectral weightings and then in Section 3.5 discussed their application as windows. We can extend these ideas into two dimensions in a straightforward manner.

We want the beam pattern associated with the weighting (or window) to approximate a circularly symmetric function. Huang [Hua81] showed that weightings (windows) of the form

$$w_{mn} = w_1 \left(\sqrt{n^2 + m^2} \right), \quad (4.91)$$

where $w_1(\cdot)$ is a continuous one-dimensional weighting (window), provide good results. Thus all of the weightings in Section 3.1 can be used for the 2-D case. As a simple example, we consider the example in Section 4.1.4.

Example 4.1.5 (continuation)

Assume that we use a Kaiser window

$$w_{K,nm} = \frac{I_0 \left[\beta \sqrt{1 - \left(\frac{\sqrt{n^2 + m^2}}{14} \right)^2} \right]}{I_0(\beta)}, \quad 0 \leq n \leq 10, 0 \leq m \leq 10, \quad (4.92)$$

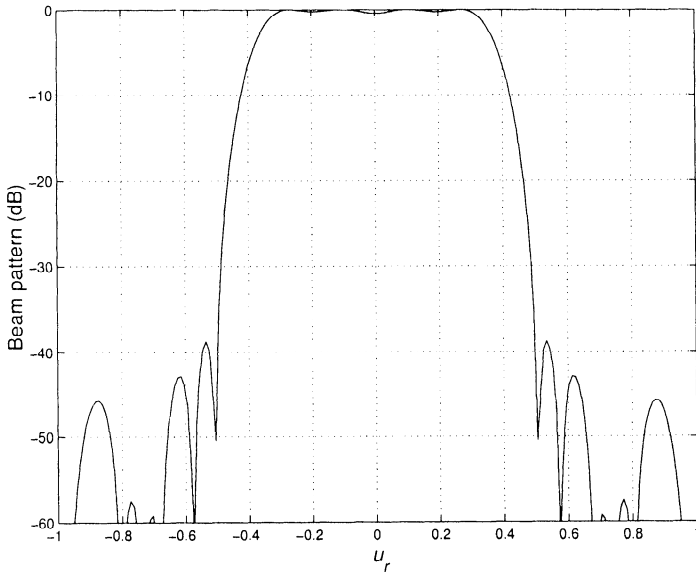


Figure 4.24 Beam pattern cut: standard rectangular grid array with square boundary: $N = M = 10$, $\psi_R = 0.4\pi$, Kaiser window, $\phi = 0^\circ, 30^\circ$, and 45° .

where $\beta = 5.0$ and I_0 is the modified Bessel function of zero-order. The constant 14 comes from $\sqrt{200}$, corresponding to the corner element of the array. We apply the Kaiser window to $a^*(n, m)$ in (4.87). Figure 4.24 shows several beam pattern cuts. All three cuts are identical. Figure 4.25 shows a plot of the beam pattern versus u_x and u_y . We see that we have obtained a good approximation to circular symmetry over a significant part of the ψ_1, ψ_2 space.

Other weightings and windows are analyzed in the problems. In Section 4.3, we analyze circular apertures and develop some desirable beam patterns. We will revisit rectangular grid arrays at that point and see how well they can approximate these beam patterns.

4.1.7 Wavenumber Sampling and 2-D DFT

In Section 3.3.3, we saw that Woodward's approach to finding the weighting function for a linear array corresponded to a DFT relation. These ideas are readily extendible to two dimensions. The problem has been studied extensively in the FIR context and is referred to as the frequency sampling problem (e.g., Rabiner and Gold [RG75]).

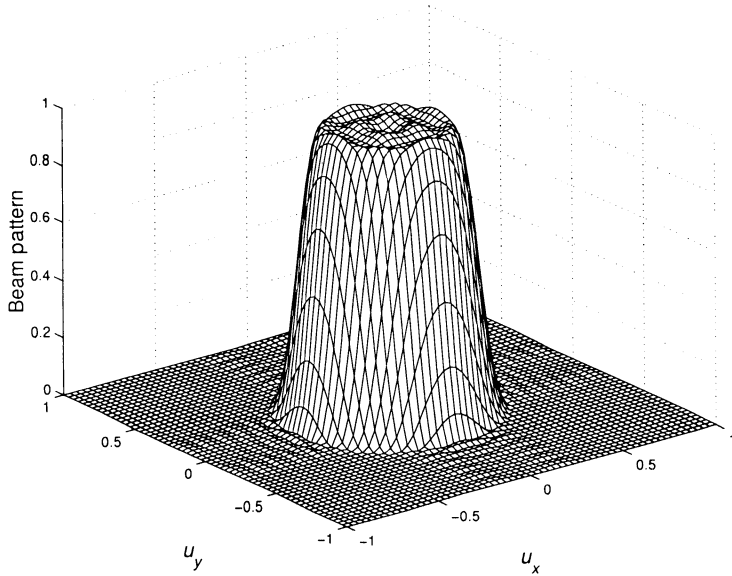


Figure 4.25 Magnitude of beam pattern versus u_x and u_y : standard rectangular grid array with square boundary, Kaiser window.

The z -transform of the array weighting function is

$$B_z(z_1, z_2) = \sum_{n=0}^{N-1} \sum_{m=0}^{M-1} w(n, m) z_1^{-n} z_2^{-m}. \quad (4.93)$$

The beam pattern is

$$B_\psi(\psi_x, \psi_y) = e^{-j\left(\frac{N-1}{2}\psi_x + \frac{M-1}{2}\psi_y\right)} B_z^*(z_1, z_2)|_{z_1=e^{j\psi_x}, z_2=e^{j\psi_y}}, \quad (4.94)$$

and

$$B_z(z_1, z_2)|_{z_1=e^{j\psi_x}, z_2=e^{j\psi_y}} = B_\psi^*(\psi_x, \psi_y) e^{-j\left(\frac{N-1}{2}\psi_x + \frac{M-1}{2}\psi_y\right)}. \quad (4.95)$$

We sample at

$$z_1 = e^{j\left(k_1 - \frac{N-1}{2}\right)\frac{2\pi}{N}}, \quad k_1 = 0, \dots, N-1, \quad (4.96)$$

and

$$z_2 = e^{j\left(k_2 - \frac{M-1}{2}\right)\frac{2\pi}{M}}, \quad k_2 = 0, \dots, M-1. \quad (4.97)$$

This corresponds to samples that are symmetric about the origin. Then,

$$B_\psi^*(\psi_{xk_1}, \psi_{yk_2}) e^{-j\left(\frac{N-1}{2}\psi_{xk_1} + \frac{M-1}{2}\psi_{yk_2}\right)}$$

$$\begin{aligned}
&= \sum_{n=0}^{N-1} \sum_{m=0}^{M-1} w(n, m) z_1^{-n} z_2^{-m} \\
&= \sum_{n=0}^{N-1} \sum_{m=0}^{M-1} w(n, m) e^{-j[(k_1 - \frac{N-1}{2}) \frac{2\pi}{N} n + (k_2 - \frac{M-1}{2}) \frac{2\pi}{M} m]} \\
&= \sum_{n=0}^{N-1} \sum_{m=0}^{M-1} \left(w(n, m) e^{j[n\pi(\frac{N-1}{N}) + m\pi(\frac{M-1}{M})]} \right) e^{-j(k_1 n \frac{2\pi}{N} + k_2 m \frac{2\pi}{M})}, \quad (4.98)
\end{aligned}$$

where

$$\psi_{xk_1} = \left(k_1 - \frac{N-1}{2} \right) \frac{2\pi}{N}, \quad k_1 = 0, 1, \dots, N-1, \quad (4.99)$$

$$\psi_{yk_2} = \left(k_2 - \frac{M-1}{2} \right) \frac{2\pi}{M}, \quad k_2 = 0, 1, \dots, M-1. \quad (4.100)$$

Now define

$$b(n, m) = w(n, m) e^{j[n\pi(\frac{N-1}{N}) + m\pi(\frac{M-1}{M})]}, \quad (4.101)$$

and

$$\begin{aligned}
B(k_1, k_2) &= B_{\psi}^*(\psi_{xk_1}, \psi_{yk_2}) e^{-j(\frac{N-1}{2}\psi_{xk_1} + \frac{M-1}{2}\psi_{yk_2})}, & k_1 &= 0, 1, \dots, N-1, \\
&& k_2 &= 0, 1, \dots, M-1. \quad (4.102)
\end{aligned}$$

Then,

$$\begin{aligned}
B(k_1, k_2) &= \sum_{n=0}^{N-1} \sum_{m=0}^{M-1} b(n, m) e^{-j(k_1 n \frac{2\pi}{N} + k_2 m \frac{2\pi}{M})}, & k_1 &= 0, 1, \dots, N-1, \\
&& k_2 &= 0, 1, \dots, M-1, \quad (4.103)
\end{aligned}$$

which is the 2-D DFT. The IDFT is

$$b(n, m) = \frac{1}{NM} \sum_{k_1=0}^{N-1} \sum_{k_2=0}^{M-1} B(k_1, k_2) e^{j(k_1 n \frac{2\pi}{N} + k_2 m \frac{2\pi}{M})}. \quad (4.104)$$

To find the weighting function, we:

(i) Sample the desired beam pattern to obtain

$$\begin{aligned}
&B_{\psi}^* \left(\left(k_1 - \frac{N-1}{2} \right) \frac{2\pi}{N}, \left(k_2 - \frac{M-1}{2} \right) \frac{2\pi}{M} \right), \\
&k_1 = 0, \dots, N-1, k_2 = 0, \dots, M-1
\end{aligned}$$

(ii) Use (4.102) to find $B(k_1, k_2)$

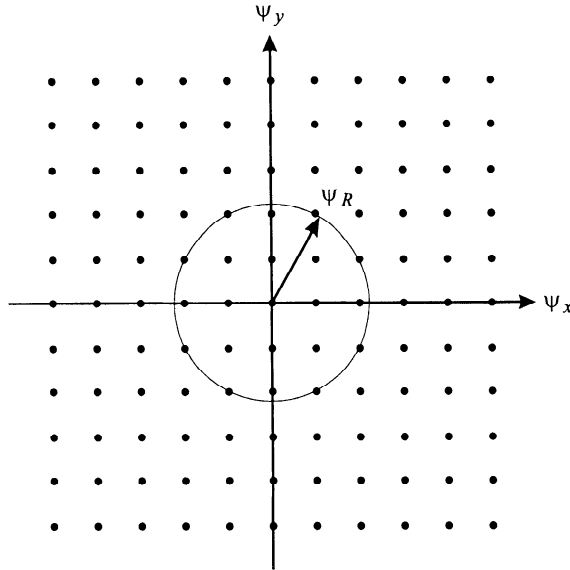


Figure 4.26 Sampling grid in wavenumber space.

(iii) Use (4.104) to find $b(n, m)$

(iv) Use (4.101) to find $w(n, m)$

(v) Use (4.1) to find $\hat{B}_d(\psi_1, \psi_2)$

If the desired beam pattern was synthesizable by a standard planar array, then $\hat{B}_d(\psi_1, \psi_2)$ will equal $B_d(\psi_1, \psi_2)$. In this case, the choice of the initial sampling point is unimportant.

For other desired beam patterns, the choice of the initial sampling point will affect the accuracy of $\hat{B}_d(\psi_1, \psi_2)$ and it may be useful to investigate several options (recall the discussion in Section 3.3.3).

We consider a simple example to demonstrate the technique.

Example 4.1.6

Consider the 11×11 sampling grid in ψ -space shown in Figure 4.26. The samples are at $((k_1 - \frac{N-1}{2}) \frac{2\pi}{N}, (k_2 - \frac{M-1}{2}) \frac{2\pi}{M})$, $0 \leq k_1 \leq N-1$, $0 \leq k_2 \leq M-1$. The desired beam pattern is constant over a circle of radius

$$\psi_R = \frac{2\pi}{N} \sqrt{5}. \quad (4.105)$$

We set

$$B_{\psi}^*(k_1 - 5, k_2 - 5) = \begin{cases} 1, & 13 \text{ interior samples,} \\ \frac{1}{2}, & 8 \text{ samples on edge,} \\ 0, & \text{all remaining samples.} \end{cases} \quad (4.106)$$

We carry out the five steps listed after (4.104) to find $\hat{B}_d(\psi_x, \psi_y)$. In Figure 4.27(a), we show the beam pattern. In Figure 4.27(b), we show several beam pattern cuts.

4.1.8 Transformations from One Dimension to Two Dimensions

In this section, we consider a different approach to the specification of the 2-D beam pattern. In Sections 4.1.5 and 4.1.7, we specified the 2-D beam pattern and then found a weighting function. In this section, we start with a desirable 1-D pattern and transform it into two dimensions. We then find the weighting function. The approach is due to Baklanov [Bak66] and Tseng and Cheng [TC68] and develops a transformation for the Chebychev pattern, although the technique is applicable to any pattern. We develop this technique in Section 4.1.8.1 and also consider alternative approaches.

In Section 4.1.8.2, we discuss some modifications to the technique.

4.1.8.1 Chebychev patterns for planar arrays⁴

In this section we consider the planar array shown in Figure 4.5. There are N^2 identical elements. The interelement spacing is d_x in the x -direction and d_y in the y -direction, so that the array is not necessarily square.

We assume that the weights are real and symmetrical about the x and y axes and the elements are cophasal in the direction of scan (θ_0, ϕ_0) .

The beam pattern is

$$\begin{aligned} B_e(\theta, \phi) &= B_{\psi}(\psi_x, \psi_y) \\ &= 4 \sum_{m=1}^N \sum_{n=1}^N a_{mn} \cos \left[(2m-1) \frac{\psi_x}{2} \right] \cos \left[(2n-1) \frac{\psi_y}{2} \right] \end{aligned} \quad (4.107)$$

for an even number of elements in each row and column, and

$$\begin{aligned} B_o(\theta, \phi) &= B_{\psi}(\psi_x, \psi_y) \\ &= \sum_{m=1}^{N+1} \sum_{n=1}^{N+1} \epsilon_m \epsilon_n a_{mn} \cos \left[(2m-1) \frac{\psi_x}{2} \right] \\ &\quad \cdot \cos \left[(2n-1) \frac{\psi_y}{2} \right] \end{aligned} \quad (4.108)$$

⁴Our discussion follows Tseng and Cheng [TC68].

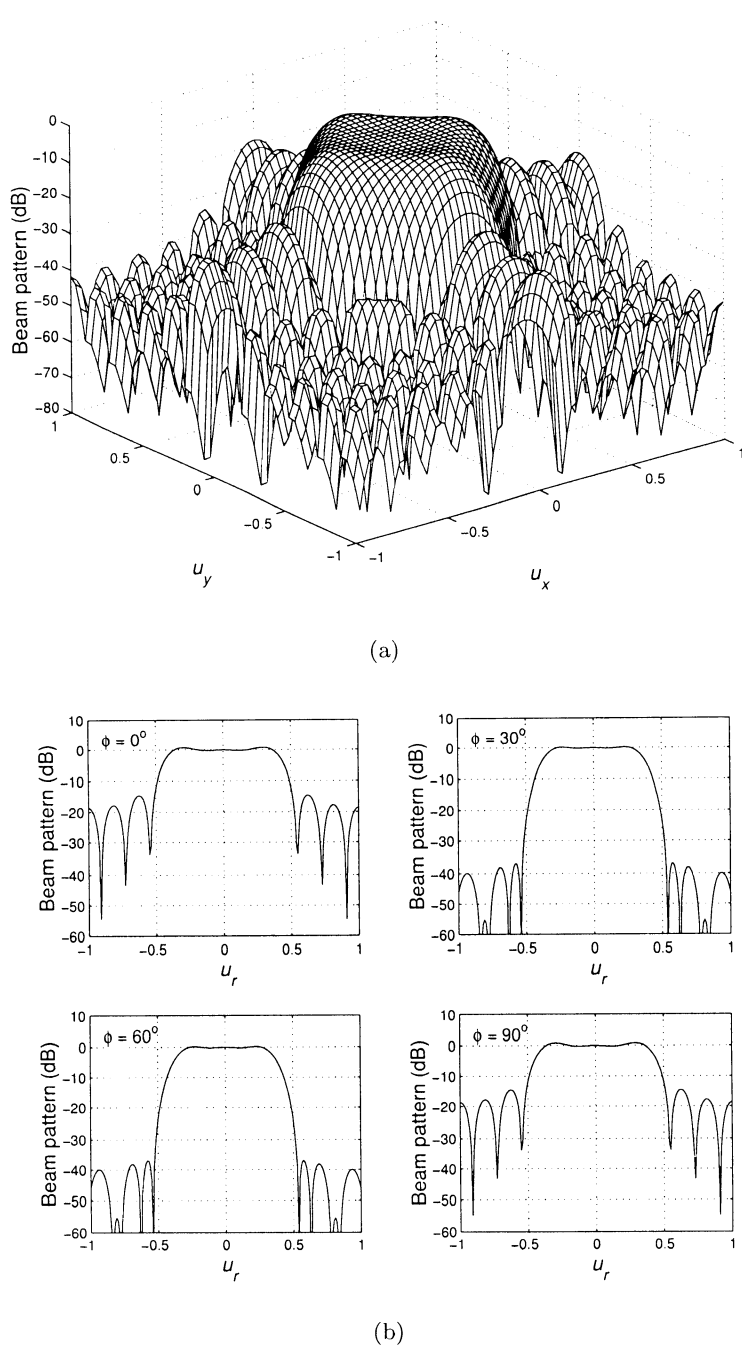


Figure 4.27 Beam pattern synthesized by pattern sampling.

for an odd number of elements in each row and column. In (4.108) $\epsilon_m = 1, m = 1; \epsilon_m = 2, m \neq 1; \epsilon_n = 1, n = 1; \epsilon_n = 2, n \neq 1$. The variables ψ_x and ψ_y are

$$\psi_x = \frac{2\pi d_x}{\lambda} (\sin \theta \cos \phi) \quad (4.109)$$

and

$$\psi_y = \frac{2\pi d_y}{\lambda} (\sin \theta \sin \phi). \quad (4.110)$$

The separable approach is to generate $B_{\psi}(\psi_x, \psi_y)$ as a product of two Chebychev polynomials of order $N - 1$. The resulting pattern is only optimum when $\psi_x = 0$ or $\psi_y = 0$.

To get a Chebychev pattern in any cross section, we must use a single Chebychev polynomial.⁵ For N even,

$$B_{\psi}(\psi_x, \psi_y) = \frac{T_{N-1}\left(x_0 \cos \frac{\psi_x}{2} \cos \frac{\psi_y}{2}\right)}{R}, \quad (4.111)$$

where $R = T_{N-1}(x_0)$. The function $B_{\psi}(\psi_x, \psi_y)$ has a maximum value of $T_{N-1}(x_0)$ at $\psi_x = \psi_y = 0$ and has sidelobes of value $-20 \log R$ dB in any cross section. The value x_0 is determined in the same manner as in the 1-D case. For example, if $N = M = 10$, and we require -20 -dB sidelobes, we solve $T_{N-1}(x_0) = 10$. This gives $x_0 = 1.0558$.

In order to find the corresponding weights, we find $B(k_1, k_2)$ from (4.102),

$$B(k_1, k_2) = e^{-j\left(\frac{N-1}{2}\psi_{xk_1} + \frac{M-1}{2}\psi_{yk_2}\right)} T_{N-1}\left(x_0 \cos\left(\frac{\psi_{xk_1}}{2}\right) \cos\left(\frac{\psi_{yk_2}}{2}\right)\right) R^{-1},$$

$$k_1 = 0, 1, \dots, N-1,$$

$$k_2 = 0, 1, \dots, M-1. \quad (4.112)$$

where ψ_{xk_1} and ψ_{yk_2} are given by (4.99) and (4.100). We use the four steps following (4.104) to find $w(n, m)$.

We illustrate the procedure with a simple example.

Example 4.1.7

Consider a 10×10 array with $d_x = \lambda/2$ and $d_y = \lambda/2$. The steering direction is broadside ($\theta_0 = 0^\circ$) and we desire -20 -dB ring sidelobes. Then,

$$T_{N-1}(x_0) = T_9(x_0) = 10, \quad (4.113)$$

and

$$x_0 = 1.0558. \quad (4.114)$$

The weightings can be obtained by taking the IDFT of (4.112) using (4.104) and (4.102). The results are shown in Table 4.2.

⁵This result is due to Baklanov [Bak66].

Table 4.2 Weightings Obtained from (4.112):
 $w_{mn}, m = 6, \dots, 10, n = 6, \dots, 10$

w_{mn}	6	7	8	9	10
6	0.7725	0.5686	0.7961	0.0294	1.0000
7	0.5686	0.9461	0.1186	0.6176	0.6667
8	0.7961	0.1186	0.4859	0.7773	0.2857
9	0.0294	0.6176	0.7773	0.3866	0.0714
10	1.0000	0.6667	0.2857	0.0714	0.0079

The 2-D Dolph-Chebychev pattern is shown in Figure 4.28(a). Several pattern cuts are shown in Figure 4.28(b). We see that they exhibit the desired Dolph-Chebychev behavior. Similar results are available when N is odd.

4.1.8.2 Modified transformations

The transformation in Section 4.1.8.1 used a $\cos(m\psi/2)$ term as a starting point because of the Chebychev beam pattern.

In many other cases when the 1-D beam pattern is real and symmetric we can write it as,

$$B_\psi(\psi) = \sum_{m=0}^{\frac{N-1}{2}} \alpha_m \cos(m\psi), \quad N \text{ odd}, \quad (4.115)$$

where, from Figure 3.22 and Table 3.2,

$$\alpha_m = \begin{cases} a_0, \\ 2a_m, \quad 1 \leq m \leq \frac{N-1}{2}. \end{cases} \quad (4.116)$$

From our discussion in Section 3.5, we can write

$$B_\psi(\psi) = \sum_{m=0}^{\frac{N-1}{2}} \tilde{\alpha}_m (\cos \psi)^m, \quad (4.117)$$

where $\tilde{\alpha}_m$ and α_m are related by the Chebychev polynomials (3.133). We create a 2-D beam pattern by using the transformation

$$\cos \psi = \cos \psi_x \cos \psi_y. \quad (4.118)$$

This transformation is a special case of transformation due to McClellan [McC82] and is a generalization of the transformation used by Baklanov [Bak66] and Tseng and Cheng [TC68].

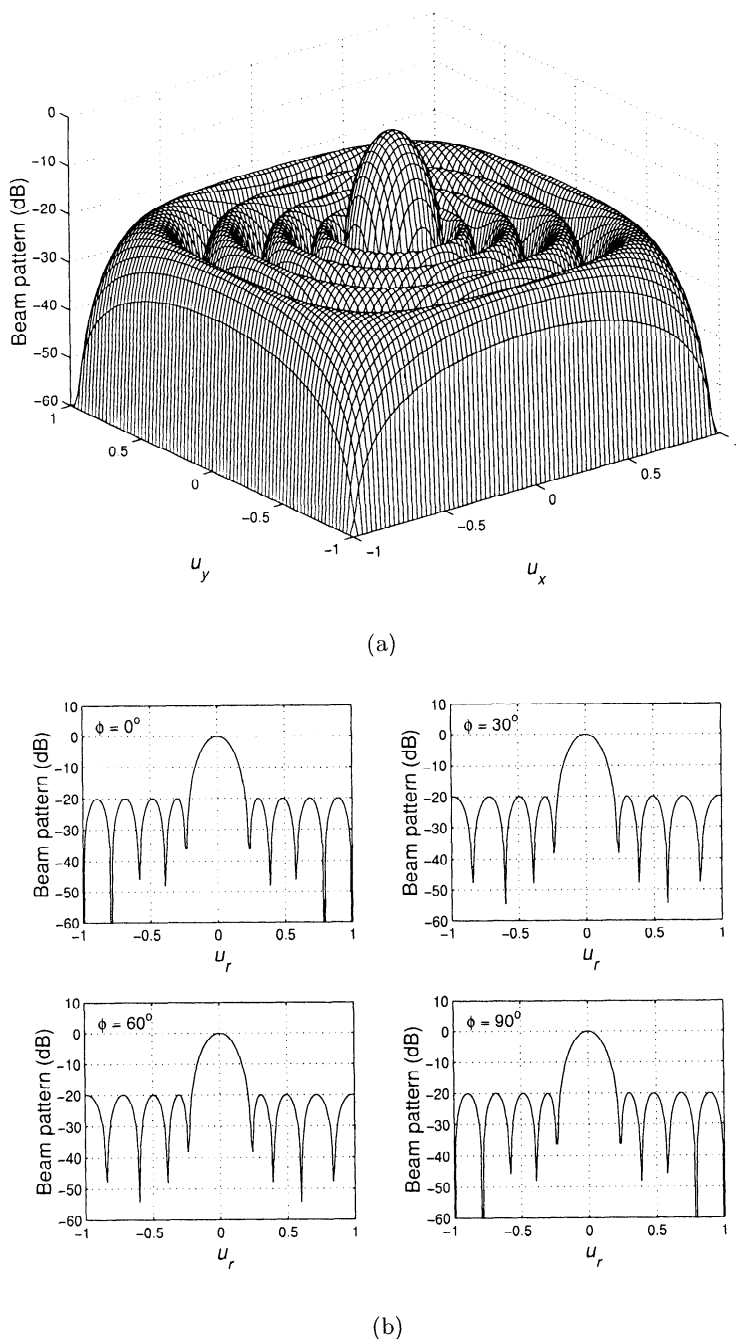


Figure 4.28 Four ϕ -cuts of the beam pattern of a standard rectangular grid array with rectangular boundary; $N = M = 10$; Tseng-Cheng distribution, -20-dB sidelobe level.

The resulting 2-D beam pattern is

$$B_{\psi}(\psi_x, \psi_y) = \sum_{m=0}^{\frac{N-1}{2}} \tilde{\alpha}_m (\cos \psi_x \cos \psi_y)^m. \quad (4.119)$$

Example 4.1.8

Consider an 11-element rectangular array with $d_x = d_y = \lambda/4$. We use a Riblet weighting with -20-dB sidelobes (e.g., (3.162)–(3.168) and Figure 3.28) and the transformation in (4.117)–(4.119). The resulting beam pattern is shown in Figure 4.29(a). Several pattern cuts are shown in Figure 4.29(b). We see that the transformation provides the desired 2-D beam pattern.

These two transformations, (4.111) and (4.119), provide an effective procedure for generating desirable 2-D beam patterns. We have demonstrated them for the Dolph-Chebychev and Riblet-Chebychev patterns, but the general technique is applicable to a large class of 1-D patterns.

4.1.9 Null Steering

Our basic discussion on null constraints in Section 3.7 was valid for arbitrary array geometries. We then considered several examples using linear arrays. We now consider the application to planar arrays. For notational simplicity, we will only consider pattern nulls and not derivative nulls. The derivative null case follows in a straightforward manner (see Problem 4.1.22).

As in (4.50), we can write the array manifold vector for the m th column of the array in Figure 4.30 as

$$\mathbf{v}_m(\psi) = e^{-j\left(\frac{N-1}{2}\psi_x + \frac{M-1}{2}\psi_y\right)} \begin{bmatrix} e^{jm\psi_y} & e^{j(\psi_x+m\psi_y)} & \dots & e^{j((N-1)\psi_x+m\psi_y)} \end{bmatrix}^T. \quad (4.120)$$

We then create an $NM \times 1$ array manifold vector, as in (4.54),

$$vec [\mathbf{V}_{\psi}(\psi)] = \begin{bmatrix} \mathbf{v}_0(\psi) \\ \vdots \\ \mathbf{v}_{M-1}(\psi) \end{bmatrix}, \quad (4.121)$$

where $\mathbf{v}_m(\psi)$ is the array manifold for the m th column, as shown in Figure 4.30 for M odd. The vector ψ is

$$\psi = \begin{bmatrix} \psi_x \\ \psi_y \end{bmatrix}, \quad (4.122)$$

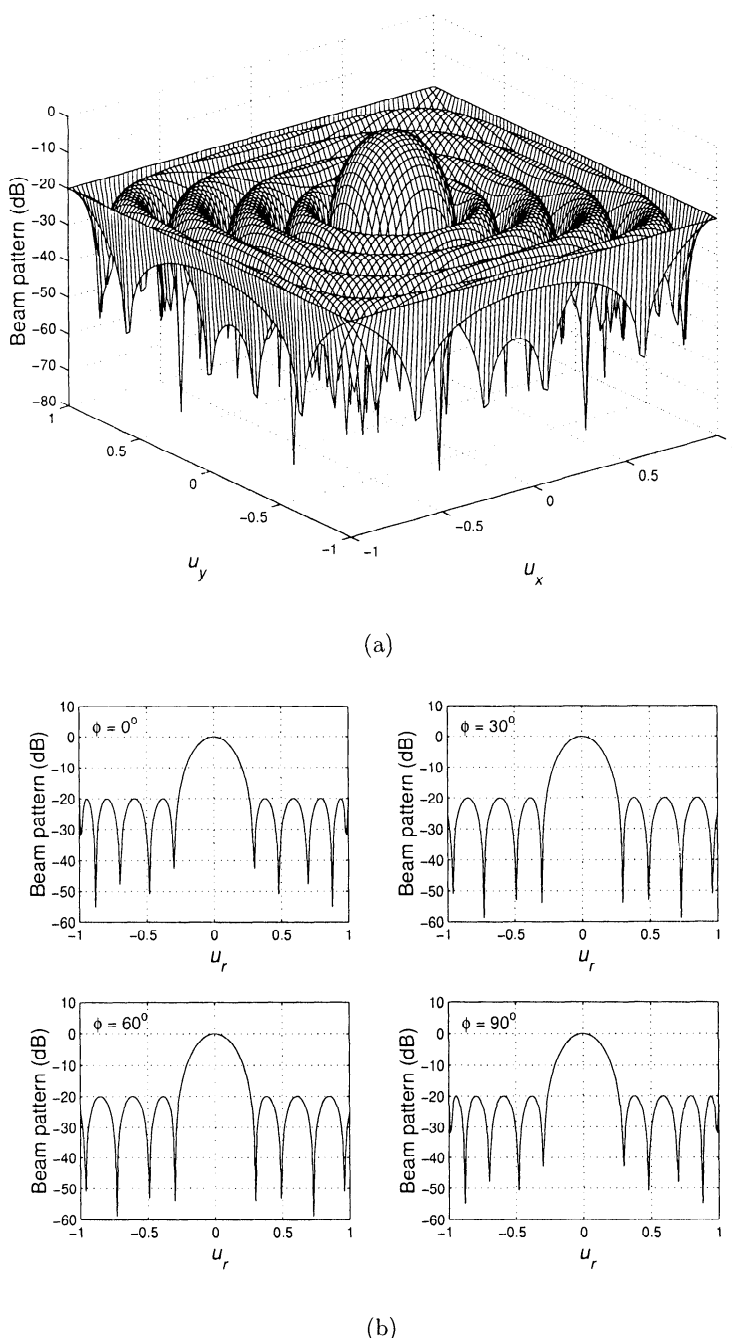


Figure 4.29 Beam pattern with 2-D Riblet-Chebychev weighting: (a) 2-D beam pattern; (b) pattern cuts: $d_x = d_y = \lambda/4$, sidelobes, -20 dB.

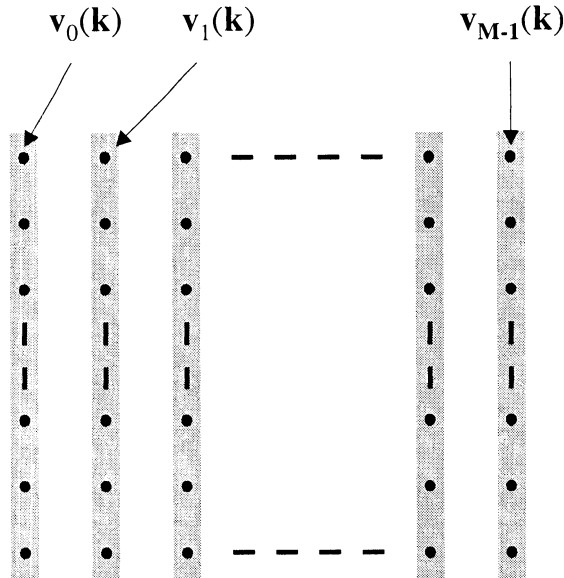


Figure 4.30 Array manifold for rectangular array.

and ψ_x and ψ_y are given in (4.2) and (4.3).

The null constraint matrix is (from (3.251)),

$$\mathbf{C}_0 = \left[\text{vec} [\mathbf{V}_{\boldsymbol{\psi}}(\psi_1)] \mid \text{vec} [\mathbf{V}_{\boldsymbol{\psi}}(\psi_2)] \mid \cdots \mid \text{vec} [\mathbf{V}_{\boldsymbol{\psi}}(\psi_{M_0})] \right], \quad (4.123)$$

and has dimensions $NM \times M_0$ where M_0 is the number of null constraints.

We assume that the desired weighting is given by an $NM \times 1$ weight vector \mathbf{w}_d . Then (3.268) applies directly,

$$\mathbf{w}_0^H = \mathbf{w}_d^H - \left[\mathbf{w}_d^H \mathbf{C}_0 \left[\mathbf{C}_0^H \mathbf{C}_0 \right]^{-1} \mathbf{C}_0^H \right]. \quad (4.124)$$

We use (4.124) to compute the weight vector. The resulting beam pattern is,

$$B_0(\boldsymbol{\psi}) = B_d(\boldsymbol{\psi}) - \mathbf{a} \mathbf{C}_0^H \text{vec} [\mathbf{V}_{\boldsymbol{\psi}}(\boldsymbol{\psi})]. \quad (4.125)$$

Using (4.123) in (4.125) gives,

$$B_0(\psi) = B_d(\psi) - \mathbf{a} \begin{bmatrix} \text{vec}^H [\mathbf{V}_\psi(\psi_1)] \text{vec} [\mathbf{V}_\psi(\psi)] \\ \text{vec}^H [\mathbf{V}_\psi(\psi_2)] \text{vec} [\mathbf{V}_\psi(\psi)] \\ \vdots \\ \text{vec}^H [\mathbf{V}_\psi(\psi_{M_0})] \text{vec} [\mathbf{V}_\psi(\psi)] \end{bmatrix}. \quad (4.126)$$

Just as in the 1-D case,

$$B_c(\psi : \psi_m) = \frac{1}{NM} \text{vec}^H [\mathbf{V}_\psi(\psi_m)] \text{vec} [\mathbf{V}_\psi(\psi)], \quad (4.127)$$

is the beam pattern of a uniformly weighted array steered to $\psi = \psi_m$. Thus,

$$B_0(\psi) = B_d(\psi) - \sum_{m=1}^{M_0} a_m N M B_c(\psi : \psi_m). \quad (4.128)$$

The results in (4.126)–(4.128) are useful to understand the behavior, but (4.124) is used to compute \mathbf{w}_0^H .

We consider a simple example to illustrate the result.

Example 4.1.9

Consider a standard 10×10 array with Dolph-Chebychev weighting (-20 -dB sidelobes) aimed at broadside. The spacing between elements is $d_x = \frac{\lambda}{2}$, $d_y = \frac{3\lambda}{4}$. We put a null at $\theta = -30^\circ$ and $\phi = -60^\circ$.

Then

$$\mathbf{C}_0 = \text{vec} [\mathbf{v}_\psi(\psi_m)], \quad (4.129)$$

with $\psi_{mx} = -0.25\pi$ and $\psi_{my} = -0.433\pi$. The resulting beam pattern is shown in Figure 4.31.

4.1.10 Related Topics

In this section we have developed the major results for rectangular arrays. There are several topics of interest that have been omitted:

- (i) Beamspace processing: the techniques in Section 3.10 can be extended to rectangular arrays in a straightforward manner.
- (ii) The beam pattern design algorithms in Section 3.9.3 can be extended to rectangular arrays.

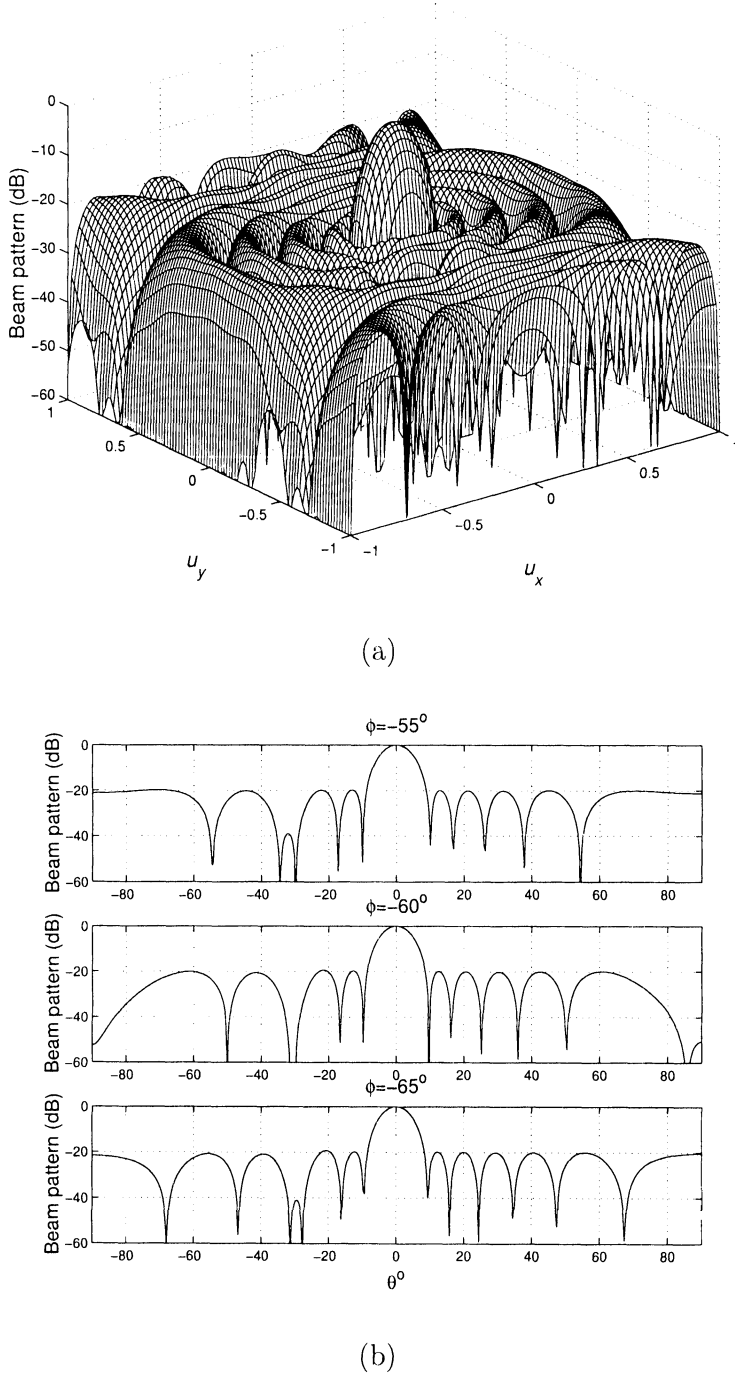


Figure 4.31 Beam pattern of Chebychev array with null.

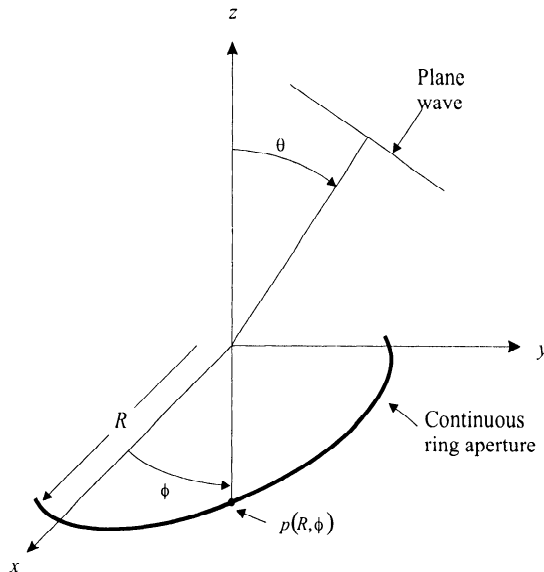


Figure 4.32 Ring apertures.

- (iii) Rectangular apertures: the techniques utilized for linear apertures can be extended to rectangular apertures.
- (iv) Difference beams can be developed for rectangular arrays. In Section 4.3.4, we discuss difference patterns for circular apertures. These techniques coupled with the techniques in Section 3.8 can be applied to rectangular arrays.
- (v) Arrays of apertures: the techniques of Section 2.8 can be extended to rectangular arrays.

Most of these topics are developed in the problems.

4.2 Circular Arrays

The geometry for the circular array and ring aperture problem is shown in Figure 4.32. The model in Figure 4.32 is for a continuous circular (or ring) aperture. For an N -element array with equal spacing between elements we sample the ring around the circumference. We begin our discussion with the continuous ring aperture.

4.2.1 Continuous Circular Arrays (Ring Apertures)

In this section we consider continuous circular arrays. These are also referred to as ring apertures and are shown in Figure 4.4(c)⁶ and Figure 4.32.

The first step is to find $\mathbf{v}(\mathbf{k})$ as defined in (2.28). The wavenumber is

$$\mathbf{k} = -\frac{2\pi}{\lambda} \begin{bmatrix} \sin \theta \cos \phi \\ \sin \theta \sin \phi \\ \cos \theta \end{bmatrix}, \quad (4.130)$$

for a plane wave arriving from $[\theta, \phi]$. The position vector is

$$\mathbf{p}_{\phi_1} = R \begin{bmatrix} \cos \phi_1 \\ \sin \phi_1 \\ 0 \end{bmatrix}, \quad (4.131)$$

for an element at $[R, \phi_1]$. Thus,

$$\begin{aligned} \mathbf{k}^T \mathbf{p}_{\phi_1} &= -\frac{2\pi}{\lambda} R \sin \theta [\cos \phi \cos \phi_1 + \sin \phi \sin \phi_1] \\ &= -\frac{2\pi}{\lambda} R \sin \theta [\cos(\phi - \phi_1)]. \end{aligned} \quad (4.132)$$

The frequency wavenumber response is

$$\Upsilon(\omega : \mathbf{k}) = \int_0^{2\pi} w(\phi_1) e^{j \frac{2\pi}{\lambda} R \sin \theta [\cos(\phi - \phi_1)]} R d\phi_1. \quad (4.133)$$

Writing (4.133) as a beam pattern

$$\begin{aligned} B(\theta, \phi) &= \int_0^{2\pi} w(\phi_1) e^{j \frac{2\pi}{\lambda} R \sin \theta [\cos(\phi - \phi_1)]} R d\phi_1 \\ &= \int_0^{2\pi} w(\phi_1) e^{j k_0 R \sin \theta [\cos(\phi - \phi_1)]} R d\phi_1, \end{aligned} \quad (4.134)$$

where $k_0 = |k| = 2\pi/\lambda$. Since any weighting function will be periodic in ϕ , we expand the aperture weighting function in a Fourier series.

$$w(\phi) = \sum_{m=-\infty}^{\infty} w'_m e^{jm\phi}, \quad (4.135)$$

where

$$w'_m = \frac{1}{2\pi} \int_0^{2\pi} w(\phi) e^{-jm\phi} d\phi. \quad (4.136)$$

⁶[Ma74] has a complete discussion of circular geometries. [Bag76] has this example.

Each term is called a **phase mode excitation** of the aperture.

Then, (4.134) can be written as

$$\begin{aligned} B(\theta, \phi) &= \sum_{m=-\infty}^{\infty} w'_m R \int_0^{2\pi} e^{j[k_0 R \sin \theta \cos(\phi - \phi_1) + m\phi_1]} d\phi_1 \\ &= 2\pi R \sum_{m=-\infty}^{\infty} w'_m j^m J_m(k_0 R \sin \theta) e^{jm\phi}, \end{aligned} \quad (4.137)$$

where $J_m(x)$ is the Bessel function of the first kind of order m .

It is convenient to normalize the weights so that when $w_0 = 1$, $B(0, \phi)$ will equal 1.

$$w'_m = \frac{1}{2\pi R} w_m. \quad (4.138)$$

We denote the component of the beam pattern due to the m th term as $B_m(\theta, \phi)$:

$$B_m(\theta, \phi) = w_m j^m J_m(k_0 R \sin \theta) e^{jm\phi}. \quad (4.139)$$

We see that each phase mode excitation term gives rise to a spatial harmonic in the beam pattern. This correspondence means that we can take a desired beam pattern in the ϕ -dimension, decompose it into its Fourier components, and separately excite each of the Fourier components with a phase mode term. The weighting must take into account the appropriate Bessel function term. The observation was made by Davies [Dav65], [R⁺83] and can be used to develop effective pattern synthesis techniques.

First, consider the case of uniform weighting,

$$w_0 = 1 \quad (4.140)$$

and

$$w_m = 0, \quad m \neq 0. \quad (4.141)$$

The pattern is uniform in ϕ and the main response axis is perpendicular to the plane of the aperture.

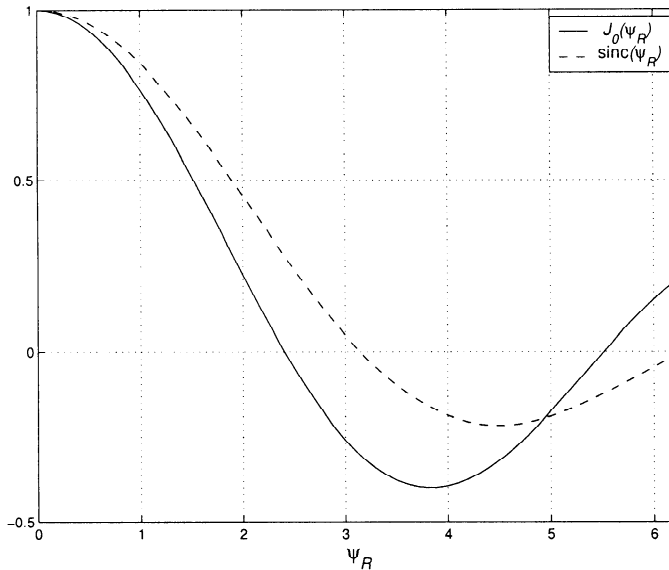
$$B(\theta, \phi) = J_0(k_0 R \sin \theta) = J_0(\psi_R), \quad (4.142)$$

where

$$\psi_R = \frac{2\pi}{\lambda} R \sin \theta = 2\pi R_\lambda \sin \theta, \quad (4.143)$$

and R_λ is the radius measured in wavelengths.

For a ring aperture, $J_0(\cdot)$ plays the same role as $\text{sinc}(\cdot)$ did for linear aperture. The two functions are shown in Figure 4.33. The first zero of

Figure 4.33 Comparison of $J_0(\psi_R)$ and $\text{sinc}(\psi_R)$.

$J_0(\psi_R)$ is at $\psi_R = 2.4$. The first sidelobe level (SLL) occurs at $\psi_R = 3.8$ and its height is -7.9 dB. These values can be compared to a linear aperture. The function $\text{sinc}(\psi_R)$ has its first zero at $\psi_R = \pi$ and its first sidelobe occurs at $\psi_R = 4.7$ with a height of -13.6 dB.

From (4.143),

$$\theta = \sin^{-1} \left(\frac{\psi_R}{2\pi R_\lambda} \right), \quad (4.144)$$

and the first null is at

$$\theta_{NULL} = \sin^{-1} \left(\frac{2.4}{2\pi R_\lambda} \right). \quad (4.145)$$

As expected, the beamwidth decreases as the radius increases.

The visible region corresponds to

$$0 \leq |\sin \theta| \leq 1, \quad (4.146)$$

or

$$0 \leq \psi_R \leq 2\pi R_\lambda. \quad (4.147)$$

In order to generate a beam pattern with ϕ -dependence we need to utilize phase modes with $m \neq 0$. In many applications, we are primarily interested

in the beam pattern in the xy -plane. We find that we can synthesize satisfactory patterns for a specific θ_0 , but the sidelobe behavior is poor for $\theta \neq \theta_0$.

To illustrate a simple case of pattern synthesis, assume that $2M+1$ phase modes are weighted in the following manner:

$$w_m = \frac{1}{j^m J_m(2\pi R_\lambda)}, \quad -M \leq m \leq M. \quad (4.148)$$

We first examine the pattern in the xy -plane ($\theta = 90^\circ$ and $\sin \theta = 1$). This weighting causes all of the modes to contribute equally to the beam pattern

$$\begin{aligned} B_m(90^\circ, \phi) &= \sum_{m=-M}^M w_m j^m J_m(2\pi R_\lambda) e^{jm\phi} \\ &= \sum_{m=-M}^M e^{jm\phi} = \frac{\sin M\phi}{\sin \phi}. \end{aligned} \quad (4.149)$$

The resulting pattern is the conventional $\sin M\phi / \sin \phi$ pattern in ϕ -space. Note that the pattern extends over 360° and the argument is ϕ . This is in contrast to the ULA, which extends over 180° and the argument is $\psi = \pi \cos \theta$ (for an array along the z -axis).

The amplitude and elevation dependence of each phase mode is governed by the corresponding Bessel function.

For the weighting in (4.148), the pattern for other values of θ is

$$B(\theta, \phi) = \sum_{m=-M}^M \frac{J_m(2\pi R_\lambda \sin \theta)}{J_m(2\pi R_\lambda)} e^{jm\phi}. \quad (4.150)$$

Using the relation,

$$J_{-m}(x) = (-1)^m J_m(x), \quad (4.151)$$

we can write (4.150) as

$$B(\theta, \phi) = \frac{J_0(2\pi R_\lambda \sin \theta)}{J_0(2\pi R_\lambda)} + \sum_{m=1}^M 2 \frac{J_m(2\pi R_\lambda \sin \theta)}{J_m(2\pi R_\lambda)} \cos m\phi. \quad (4.152)$$

For small $|\theta|$, the beam pattern is still acceptable, but it degenerates rapidly as θ increases.

To determine how many modes can be excited for a ring aperture of radius R , we examine the behavior of the Bessel functions in the visible

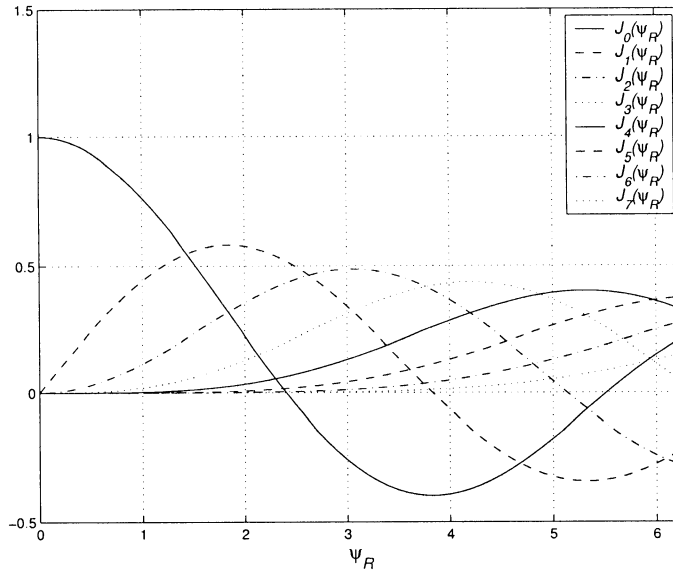


Figure 4.34 $J_0(\psi_R)$ through $J_7(\psi_R)$ versus ψ_R ; $\psi_R = 2\pi R_\lambda \sin \theta$; $R_\lambda = 1$.

region. The first seven Bessel functions are plotted versus $x = 2\pi R_\lambda \sin \theta$ in Figure 4.34 for the case when

$$R_\lambda = 1. \quad (4.153)$$

In this case the visible region is $0 < x < 2\pi$. We see that the first six Bessel functions have a non-zero value in the visible region, and that J_7 has a slight non-zero value toward the upper end of the region.

In general, the amplitude is small when the order m exceeds the argument. Thus,

$$M \simeq 2\pi R_\lambda \quad (4.154)$$

is a useful limit. We can use $2M + 1$ phase modes.

In order to have each mode available, we need to choose R so that

$$J_m(2\pi R_\lambda) \neq 0. \quad (4.155)$$

One can show (e.g., p. 307 of [R⁺83]) that if the diameter, $2R$, is an integral number of half-wavelengths, then (4.155) is satisfied.

We see that by using the phase mode excitation technique, for any given elevation angle θ , we can synthesize a desired pattern in ϕ corresponding to a $(2M+1)$ -element linear array. Thus all of the design techniques in Chapter

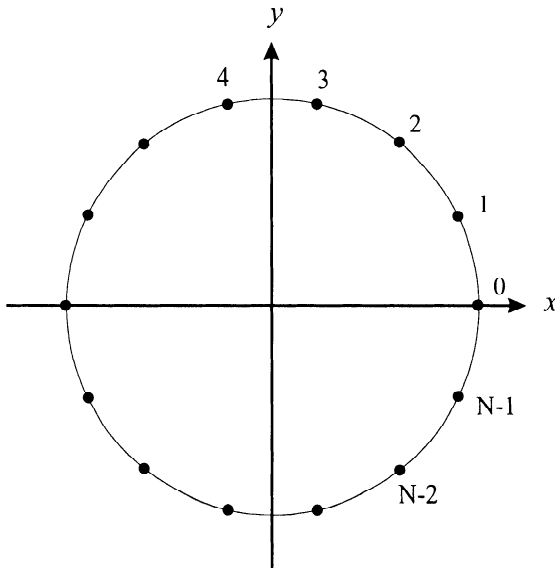


Figure 4.35 Geometry for circular array.

3 can be applied to the ring aperture. In Section 4.2.3, we discuss methods for implementing phase mode excitation beam patterns.

In practice, we normally use a circular array rather than a continuous aperture. We analyze its behavior in the next section.

4.2.2 Circular Arrays

The geometry of interest for the discrete circular array is shown in Figure 4.35. For isotropic elements, the array weighting will correspond to sampling the continuous aperture weighting. If we assume the aperture weighting generated M spatial harmonics, then a sampling theorem argument indicates that we need $(2M + 1)$ elements to reproduce these spatial harmonics. Using (4.154), this condition implies

$$N \geq 2 \left(\frac{2\pi R}{\lambda} \right) + 1, \quad (4.156)$$

which implies the spacing on the arc is

$$d_{cir} \leq \frac{\lambda}{2}. \quad (4.157)$$

To find the beam pattern, we use a sampling function. We assume that the highest spatial frequency that affects the beam pattern is,

$$M = 2\pi R_\lambda. \quad (4.158)$$

Then, the minimum sampling frequency is $4\pi R_\lambda$ and the sampling interval around the circle is

$$\phi_T = \frac{2\pi}{2\frac{2\pi}{\lambda}R} = \frac{\lambda}{2R}. \quad (4.159)$$

The sampling function is

$$S_\phi(\phi) = \sum_{n=-\infty}^{\infty} \delta(\phi - n\phi_T). \quad (4.160)$$

We can use the expression,

$$\sum_{n=-\infty}^{\infty} \delta(\phi - n\phi_T) = \frac{1}{\phi_T} \sum_{q=-\infty}^{\infty} e^{jqN\phi}, \quad (4.161)$$

and rewrite that sampling function as

$$\begin{aligned} S_\phi(\phi) &= \sum_{q=-\infty}^{\infty} e^{jqN\phi} \\ &= 1 + \sum_{q=1}^{\infty} e^{jqN\phi} + \sum_{q=1}^{\infty} e^{-jqN\phi}. \end{aligned} \quad (4.162)$$

Then, the weighting for the m th-order phase mode is,

$$w_m(\phi) = w_m e^{jm\phi} S_\phi(\phi). \quad (4.163)$$

Using (4.162) in (4.163) gives

$$w_m(\phi) = w_m e^{jm\phi} + w_m \sum_{q=1}^{\infty} e^{j(Nq+m)\phi} + w_m \sum_{q=1}^{\infty} e^{-j(Nq-m)\phi}. \quad (4.164)$$

The corresponding beam pattern for the m th mode is,

$$\begin{aligned} B_m(\theta, \phi) &= w_m j^m J_m(2\pi R_\lambda \sin \theta) e^{jm\phi} \\ &\quad + \sum_{g=1}^{\infty} w_m j^{-g} J_g(2\pi R_\lambda \sin \theta) e^{-jg\phi} \\ &\quad + \sum_{h=1}^{\infty} w_m j^h J_h(2\pi R_\lambda \sin \theta) e^{jh\phi}, \end{aligned} \quad (4.165)$$

where $g = (Nq - m)$ and $h = (Nq + m)$.

The first term is the desired beam pattern corresponding to the ring aperture and the remaining terms are residual distortion modes due to sampling. The first distortion mode has a Bessel function of order $(N - m)$. It will have negligible amplitude in the visible region if

$$N - m > \frac{2\pi R}{\lambda}. \quad (4.166)$$

However,

$$m \leq M \leq \frac{2\pi R}{\lambda}. \quad (4.167)$$

Thus, (4.166) implies that the distortion modes will be negligible if

$$N \geq \frac{4\pi R}{\lambda} \geq 2M. \quad (4.168)$$

The condition in (4.168) is satisfied if

$$d_{cir} \leq \frac{\lambda}{2}. \quad (4.169)$$

We can make the distortion modes as small as desired by increasing N . In Table 4.3,⁷ we show the maximum residual contribution as a function of $(N - M)$ for $R_\lambda = 1$.

Table 4.3 Maximum Residual Contribution as a Function of N

N	13	14	15	16	17	18	19
$J_{N-M}(k_0 r)$	0.158	0.073	0.029	0.010	0.003	8.8e-4	2.3e-4

We see that for $N > 15$, the residual contribution would be approximately 0.01 ($d_{cir} = 0.42$). We will focus our attention in the text on arrays that satisfy (4.168) and (4.169).

The total pattern is

$$B(\theta, \phi) = \sum_{m=-\infty}^{\infty} B_m(\theta, \phi), \quad (4.170)$$

where $B_m(\theta, \phi)$ is given by (4.165). When the main response axis of the array is steered, it is convenient to define a new set of variables.⁸ The beam pattern is

⁷From [MZ94].

⁸This is a reasonably standard derivation (e.g., [Ma74], p.192).

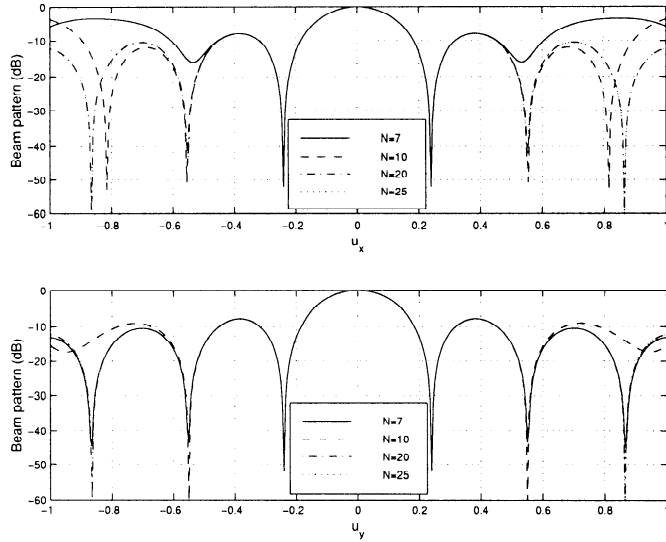


Figure 4.36 Beam patterns for a uniform circular array steered to broadside:
(a) $\phi = 0$ and π ; (b) $\phi = \pi/2$ and $3\pi/2$.

$$B(\theta, \phi) = \sum_{n=0}^{N-1} w_n \exp [jk_0 R \sin \theta \cos (\phi - \phi_n) + j\beta_n], \quad (4.171)$$

where β_n is the phase factor with respect to the origin. To align the MRA along (θ_0, ϕ_0) ,

$$\beta_n = -k_0 R \sin \theta_0 \cos (\phi_0 - \phi_n). \quad (4.172)$$

We now define a new set of variables,

$$\rho = R \left\{ \left[(\sin \theta \cos \phi - \sin \theta_0 \cos \phi_0)^2 + (\sin \theta \sin \phi - \sin \theta_0 \sin \phi_0)^2 \right]^{\frac{1}{2}} \right\}, \quad (4.173)$$

and

$$\cos \xi = \frac{\sin \theta \cos \phi - \sin \theta_0 \cos \phi_0}{\left[(\sin \theta \cos \phi - \sin \theta_0 \cos \phi_0)^2 + (\sin \theta \sin \phi - \sin \theta_0 \sin \phi_0)^2 \right]^{\frac{1}{2}}}. \quad (4.174)$$

We can rewrite (4.171) as

$$B(\theta, \phi) = \sum_{n=1}^N w_n \exp [jk_0\rho \cos (\xi - \phi_n)]. \quad (4.175)$$

If we assume uniform excitation and equally spaced elements, then

$$w_n = \frac{1}{N}, \quad (4.176)$$

and

$$\phi_n = \frac{2\pi n}{N}, \quad (4.177)$$

$$B(\theta, \phi) = \sum_{m=-\infty}^{\infty} j^{mN} e^{-jmN\xi} J_{mN}(k_0\rho), \quad (4.178)$$

where mN is the product of the index m and the number of elements N . The term corresponding to $m = 0$, $J_0(k\rho)$ is the principal term and the other terms are the residuals. This expression has the same form as (4.165) and our previous discussion concerning residuals carries over. The behavior of the pattern can be examined by plotting (4.178).

The beam pattern of a uniform circular array with $2\pi R_\lambda = 10$ for the $\theta_0 = 0$ case is plotted in Figure 4.36 for $\phi = 0$ and $\phi = \frac{\pi}{2}$ and several values of N . In this case, (4.178) reduces to

$$B(\theta, \phi) = \sum_{m=-\infty}^{\infty} j^{mN} e^{-jmN\xi} J_{mN}(k_0 R \sin \theta). \quad (4.179)$$

The main-lobe behavior is adequately described by the J_0 term. The effect of finite N appears in the sidelobe structure.

In Figure 4.37, we show the beam pattern for a 20-element array with $2\pi R_\lambda = 2\pi R/\lambda = 10$ ($d_{cir} = \lambda/2$). In Figure 4.38 we show the vertical patterns along the planes $\phi = 0^\circ$ (the left side of the plot in $\phi = 180^\circ$). As N is increased for a fixed $2\pi R/\lambda$, the beam pattern approaches the beam pattern of the ring aperture.

4.2.3 Phase Mode Excitation Beamformers

Davies [R⁺83], [Dav65] showed how to excite the phase modes using a Butler beamforming matrix. Our approach is similar to his original work. In order

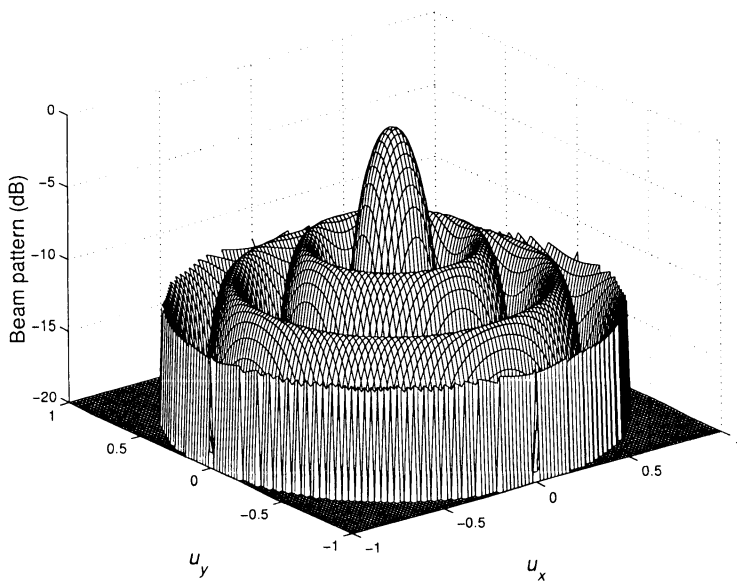


Figure 4.37 Beam pattern for a uniform circular array of 20 elements ($2\pi R/\lambda = 10$).

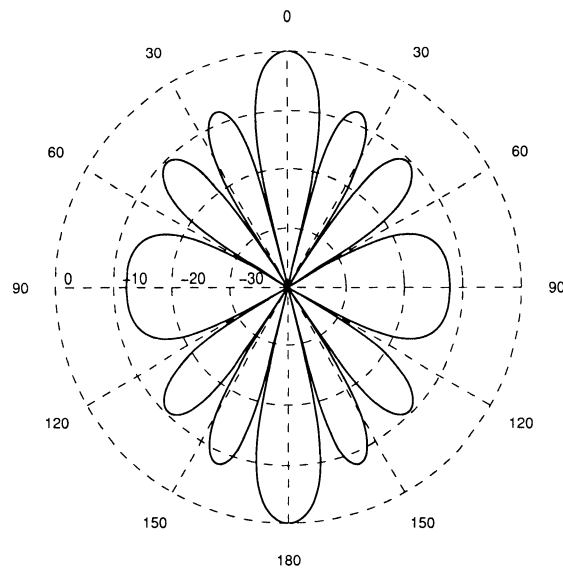


Figure 4.38 Beam patterns as a function of θ for a uniform circular array of 20 elements ($2\pi R/\lambda = 10$) with uniform weighting: $\phi = 0^\circ$ (and $\phi = 180^\circ$).

to generate the m th phase mode from the incoming signal, we multiply by the $N \times 1$ weight vector,

$$\mathbf{w}_m^H = \frac{1}{\sqrt{N}} \left[1 \quad e^{jm\frac{2\pi}{N}} \quad e^{jm\frac{2\pi}{N}2} \quad \dots \quad e^{jm\frac{2\pi}{N}(N-1)} \right]. \quad (4.180)$$

We can generate a $(2M + 1)$ -dimensional beamspace with the matrix \mathbf{B}_{PM}^H , where

$$\mathbf{B}_{PM}^H = \mathbf{C}_j \mathbf{B}_1^H, \quad (4.181)$$

$$\mathbf{B}_1 = \left[\mathbf{w}_{-M} \quad \dots \quad \mathbf{w}_0 \quad \dots \quad \mathbf{w}_M \right], \quad (4.182)$$

and

$$\mathbf{C}_j \triangleq \text{diag} \left\{ j^{-M}, \dots, j^{-1}, 1, j^1, \dots, j^M \right\}. \quad (4.183)$$

The matrix \mathbf{B}_1^H generates the phase modes and the diagonal matrix \mathbf{C}_j scales the output. The scaling in \mathbf{C}_j is motivated by (4.139). Then the beamspace array manifold vector is given by the $(2M + 1) \times 1$ vector

$$\mathbf{v}_{BS}(\theta, \phi) = \mathbf{B}_{PM}^H \mathbf{v}(\theta, \phi). \quad (4.184)$$

Using (4.139), we can write (4.184) as

$$\mathbf{v}_{BS}(\theta, \phi) = \tilde{\mathbf{J}}(2\pi R_\lambda \sin \theta) \mathbf{v}(\phi), \quad (4.185)$$

where the azimuthal dependence is completely contained in $\mathbf{v}(\phi)$:

$$\mathbf{v}(\phi) = \left[e^{-jM\phi} \quad \dots \quad e^{-j\phi} \quad 1 \quad e^{j\phi} \quad \dots \quad e^{jM\phi} \right]^T, \quad (4.186)$$

which has the same form as a uniform linear array. The elevation dependence is contained in $\tilde{\mathbf{J}}(\cdot)$,

$$\tilde{\mathbf{J}}(x) \triangleq \text{diag} \left\{ J_M(x), \dots, J_1(x), J_0(x), J_1(x), \dots, J_M(x) \right\}. \quad (4.187)$$

We observe that $\mathbf{v}_{BS}(\theta, \phi)$ is conjugate symmetric and that the columns of \mathbf{B}_{PM} are orthonormal.

We can now operate on $\mathbf{v}_{BS}(\theta, \phi)$ to achieve a desired beam pattern. Defining,

$$\mathbf{w}_{PM}^H = \left[w_{-M}^* \quad \dots \quad w_0^* \quad \dots \quad w_M^* \right]^T, \quad (4.188)$$

the output $y(k)$ is

$$y(k) = \mathbf{w}_{PM}^H \mathbf{B}_{PM}^H \mathbf{x}(k), \quad (4.189)$$

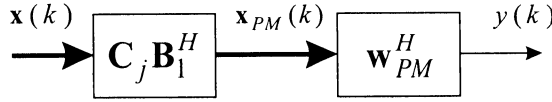


Figure 4.39 Phase mode excitation beamformer.

and the beam pattern is

$$B(\theta, \phi) = \mathbf{w}_{PM}^H \tilde{\mathbf{J}}(2\pi R_\lambda \sin \theta) \mathbf{v}(\phi). \quad (4.190)$$

The beamspace processor is shown in Figure 4.39.

We illustrate the design procedure with an example.

Example 4.2.1

Consider a 25-element uniform circular array with radius $2\pi R = 10\lambda$. Using (4.154), we see that we can excite 21 phase modes.

We design the beam pattern for the case when $\theta = 90^\circ$. The desired pattern corresponds to the Villeneuve pattern in Figure 3.31(a) in ϕ -space instead of u -space.

To achieve the desired pattern, we use

$$[\mathbf{w}_{PM}^H]_m = \frac{[\mathbf{w}_{VIL}^H]_m}{j^m J_m(2\pi R_\lambda)}, \quad (4.191)$$

where \mathbf{w}_{VIL} was derived in Section 3.5.4. The resulting beam pattern is plotted versus ϕ for $\theta = 90^\circ$ in Figure 4.40. The pattern exhibits the desired behavior for $\theta = 90^\circ$, but deteriorates rapidly as θ moves away from 90° (these patterns are not shown). To achieve satisfactory behavior we need to introduce vertical directivity in the sensor elements. We do this in the next example.

Example 4.2.2 (continuation)

Consider a 25-element uniform circular array with radius $2\pi R = 10\lambda$. Each element is a linear aperture that is parallel to the z -axis (perpendicular to the xy -plane) with length $L = 10\lambda$. We use the same phase mode weighting in (4.191). In Figure 4.41, the resulting beam pattern is plotted versus ϕ for $\theta = 0.5137\pi$ radians. (This corresponds to the first sidelobe of the element pattern.) The resulting pattern is well-behaved.

The argument of the Bessel function restricts both the elevation beam pattern and the array bandwidth.⁹ This limitation is due to cancellation effects between elements at opposite sides of the circle. Therefore, most circular arrays use elements with an element beam pattern whose main response axis is in the radial direction. Synthesis of desirable array beam patterns is more difficult because the pattern is not a product of the element pattern and the array factor. Discussions of this topic are contained in Mailloux [Mai94], Davies [Dav87], and Rahim and Davies [RD82]. The

⁹This discussion follows Chapter 4 of Mailloux [Mai94].

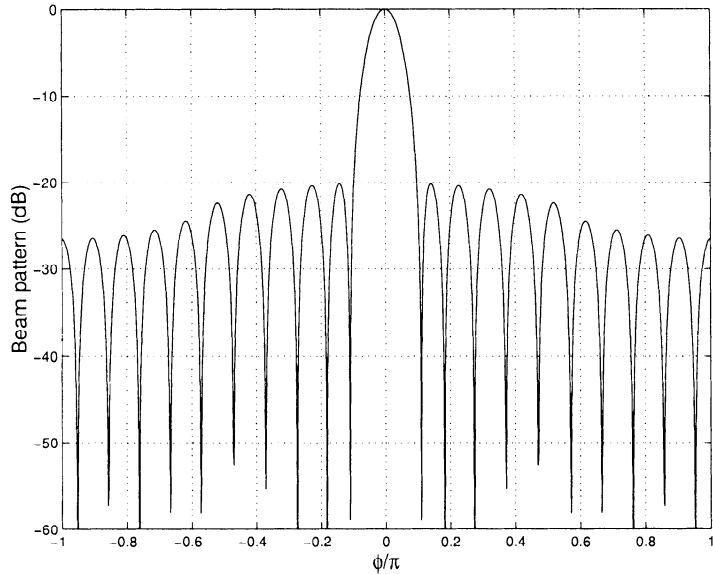


Figure 4.40 Beam pattern versus ϕ : Villenueve phase excitation, $\theta = 90^\circ$.

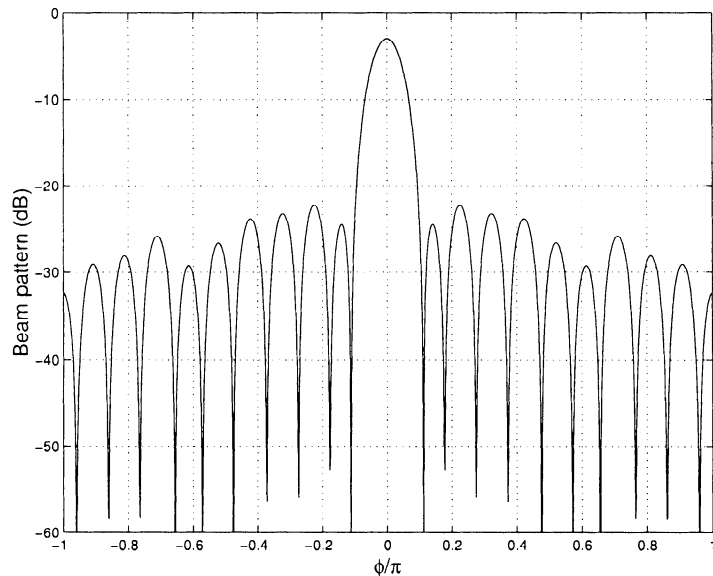


Figure 4.41 Beam pattern versus ϕ for various θ : Villenueve phase excitation, $\theta = 0.514\pi$.

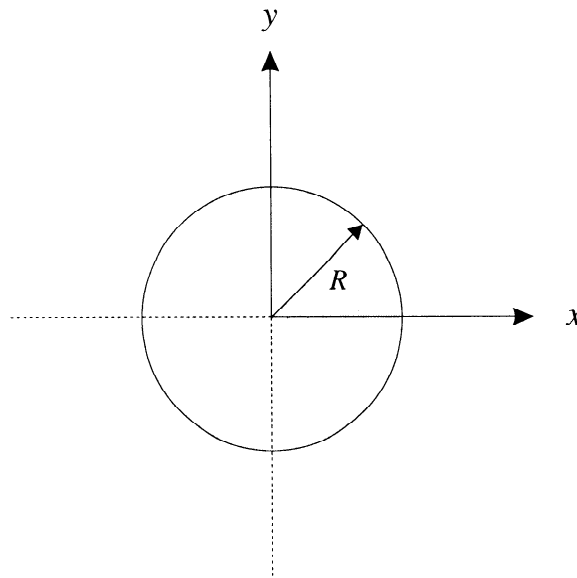


Figure 4.42 Circular aperture.

synthesis techniques that were developed in Section 3.9.3 are applicable to this problem and have been applied to it by Sureau and Keeping [SK82] and Bell et al. [BVT99].

In many applications, the main response axis is scanned in azimuth and only the elements in a 90° sector centered on the MRA are utilized. The techniques in Section 3.9.3 are useful in this case also.

Other references that discuss various aspects of circular arrays include Hansen [Han98], which contains a history of the various advances, and the book by Ma [Ma74].

4.3 Circular Apertures

In this section we consider the characteristics of circular apertures lying in the xy -plane, as shown in Figure 4.42. These apertures are important in many applications (perhaps the most common being the aperture of a parabolic antenna). In addition, they provide the limiting case for several array configurations such as the concentric circular array shown in Figure 4.2(b) and the hexagon array shown in Figure 4.3.

4.3.1 Separable Weightings

We assume that the weighting function is separable in polar coordinates,

$$w(r, \phi_a) = w_R(r) w_\phi(\phi_a). \quad (4.192)$$

We will find that a number of useful beam patterns can be synthesized with separable weightings. The beam pattern for a broadside beam ($\theta_0 = 0$) is given by

$$B(\theta, \phi) = \int_0^R \int_0^{2\pi} w(r, \phi_a) \exp \left[j \frac{2\pi}{\lambda} r \sin \theta \cos(\phi - \phi_a) \right] r dr d\phi_a. \quad (4.193)$$

Letting k_r denote the radial component of the wavenumber,

$$k_r = \frac{2\pi r}{\lambda} \sin \theta, \quad (4.194)$$

and defining

$$\alpha = \phi - \phi_a + \frac{\pi}{2}, \quad (4.195)$$

we can write

$$\sin \alpha = \sin \left(\phi - \phi_a + \frac{\pi}{2} \right) = \cos(\phi - \phi_a). \quad (4.196)$$

Using (4.194)–(4.196), the beam pattern can be written as

$$B(\theta, \phi) = \int_0^{2\pi} d\phi_a \int_0^R w(r, \phi_a) \exp(j k_r \sin \alpha) r dr. \quad (4.197)$$

We can write the exponential term in (4.197) as a Fourier series,

$$\exp(j k_r \sin \alpha) = \sum_{n=-\infty}^{\infty} J_n(k_r) e^{jn\alpha}, \quad (4.198)$$

where

$$J_n(k_r) = \frac{1}{2\pi} \int_{-\pi}^{\pi} \exp[\pm j(k_r \sin x - nx)] dx. \quad (4.199)$$

Using (4.192), (4.195), and (4.198) in (4.197), we have¹⁰

$$\begin{aligned} B(\theta, \phi) &= \sum_{n=-\infty}^{\infty} j^n e^{jn\phi} \left[\int_0^{2\pi} w_\phi(\phi_a) e^{-jn\phi_a} d\phi_a \right] \\ &\quad \cdot \int_0^R w_R(r) J_n \left(\frac{2\pi r}{\lambda} \sin \theta \right) r dr, \end{aligned} \quad (4.200)$$

¹⁰We use $\exp(j \frac{n\pi}{2}) = j^n$ and $J_{-n}(x) = (-1)^n J_n(x)$.

which is the desired result. We now consider some simple cases. Assume

$$w_\phi(\phi_a) = e^{jm\phi_a}. \quad (4.201)$$

This is equivalent to a sinusoidal variation in ϕ . Substituting (4.201) into the first integral in (4.200) gives,

$$\int_0^{2\pi} e^{j(m-n)\phi_a} d\phi_a = 2\pi\delta_{mn}, \quad (4.202)$$

so (4.200) becomes

$$B(\theta, \phi) = 2\pi j^m e^{jm\phi} \int_0^R w_R(r) J_m\left(\frac{2\pi r}{\lambda} \sin \theta\right) r dr. \quad (4.203)$$

For the special case in which $m = 0$, the weighting in the ϕ -direction is uniform and

$$B(\theta, \phi) = B(\theta) = 2\pi \int_0^R w_R(r) J_0\left(\frac{2\pi r}{\lambda} \sin \theta\right) r dr. \quad (4.204)$$

If we substitute¹¹

$$u_R = \frac{2R}{\lambda} \sin \theta, \quad (4.205)$$

$$p = \frac{\pi r}{R}, \quad (4.206)$$

and

$$g_0(p) = \frac{2R^2}{\pi} w_R\left(\frac{Rp}{\pi}\right), \quad (4.207)$$

then (4.204) can be written as,

$$B(\theta) = \int_0^\pi p g_0(p) J_0(u_R p) dp. \quad (4.208)$$

The reason for this choice of variables is to obtain an integral with $[0, \pi]$ limits.

The final simplification is to assume that $w_R(r)$ is constant ($w_R(r) = c$) from 0 to R . In this case, we can use (4.204) without the change of variables. Then (4.204) becomes

$$B(\theta) = 2\pi c \int_0^R J_0\left(\frac{2\pi r}{\lambda} \sin \theta\right) r dr. \quad (4.209)$$

¹¹Note that u_R is not the radial component in (ψ_x, ψ_y) space. It contains a factor of R so the visible region is $0 \leq u_R \leq 2R/\lambda$. This notation is used to be consistent with the antenna literature.

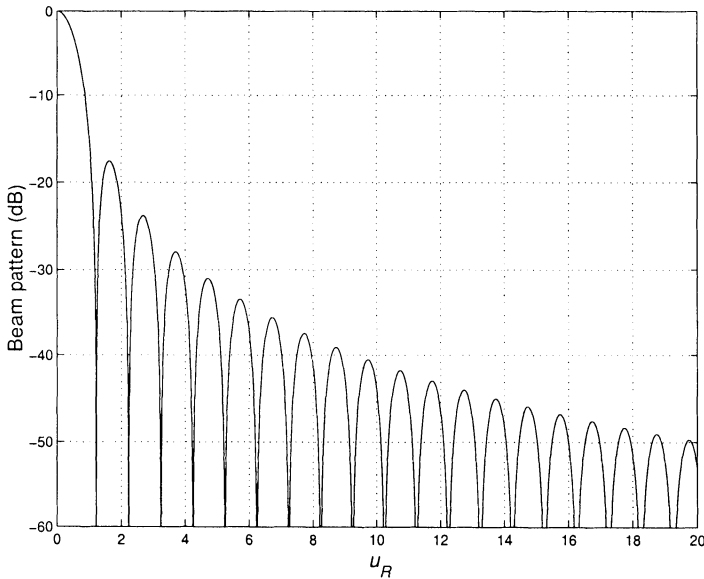


Figure 4.43 Beam pattern of a circular aperture lying in the xy -plane with $R/\lambda = 10$ and uniform weighting; the horizontal axis is $u_R = \psi_R/\pi$ and the visible region is $0 \leq u \leq 2R/\lambda$.

Using

$$\int_0^R x J_0(\alpha x) dx = \frac{R}{\alpha} J_1(\alpha R), \quad (4.210)$$

we obtain

$$B(\theta) = cR \frac{J_1\left(\frac{2\pi R}{\lambda} \sin \theta\right)}{\frac{\sin \theta}{\lambda}}. \quad (4.211)$$

One can show that

$$B(0) = c\pi R^2, \quad (4.212)$$

so the normalized pattern is

$$B(\theta) = 2 \frac{J_1\left(\frac{2\pi R}{\lambda} \sin \theta\right)}{\frac{2\pi R}{\lambda} \sin \theta} = 2 \frac{J_1(\pi u_R)}{\pi u_R}. \quad (4.213)$$

The visible region is $0 \leq \psi_R \leq 2\pi R/\lambda$. In Figure 4.43 we plot the normalized beam pattern versus u_R .

The first null of $J_1(\pi u_R)$ is at

$$u_R = 1.22, \quad (4.214)$$

or

$$\theta = \sin^{-1} \left(1.22 \frac{\lambda}{2R} \right). \quad (4.215)$$

The height of the first sidelobe is -17.6 dB.

One can show that the HPBW is

$$\begin{aligned} \Delta\theta &= 2\sin^{-1} \left(0.257 \frac{\lambda}{R} \right) \simeq 0.514 \frac{\lambda}{R} \text{ rad} \\ &= 29.2 \frac{\lambda}{R} \text{ degrees.} \end{aligned} \quad (4.216)$$

This compares to the HPBW for a square aperture of the same area

$$\begin{aligned} \Delta\theta_{sq} &= 2\sin^{-1} \left(0.250 \frac{\lambda}{R} \right) \simeq 0.50 \frac{\lambda}{R} \text{ rad} \\ &= 28.65 \frac{\lambda}{R} \text{ degrees.} \end{aligned} \quad (4.217)$$

Thus, the circular aperture has a slightly larger 3-dB beamwidth, but the sidelobes are significantly lower (-17.6 dB vs. -13.4 dB).

In order to improve the sidelobe characteristics, a nonuniform radial weighting is used. A family of weightings that is used in practice (e.g., [Bal82], [Jas61]) is

$$w_R(r) = \begin{cases} \left[1 - \left(\frac{r}{R} \right)^2 \right]^n, & 0 \leq r \leq R, n = 0, 1, 2, 3, \dots, \\ 0, & \text{elsewhere.} \end{cases} \quad (4.218)$$

For $n = 0$, we have the uniform distribution that we just analyzed. The characteristics for $n = 0, 1$, and 2 are shown in Table 4.4. As n increases, the HPBW increases and the height of the first sidelobe decreases.

Table 4.4 Characteristics of Circular Apertures with Circular Symmetric Weightings¹²

Radial Weighting	Uniform	Radial Taper	Radial Taper Squared
$w_R(r)$	$\left[1 - \left(\frac{r}{R}\right)^2\right]^0$	$\left[1 - \left(\frac{r}{R}\right)^2\right]^1$	$\left[1 - \left(\frac{r}{R}\right)^2\right]^2$
Beam pattern	$2 \frac{J_1(\psi_R)}{\psi_R}$	$8 \frac{J_2(\psi_R)}{\psi_R^2}$	$48 \frac{J_3(\psi_R)}{\psi_R^3}$
Half-power beamwidth (degrees) $R \gg \lambda$	$\frac{29.2}{\frac{R}{\lambda}}$	$\frac{36.4}{\frac{R}{\lambda}}$	$\frac{42.1}{\frac{R}{\lambda}}$
BW_{NN} (degrees) $R \gg \lambda$	$\frac{69.9}{\frac{R}{\lambda}}$	$\frac{93.4}{\frac{R}{\lambda}}$	$\frac{116.3}{\frac{R}{\lambda}}$
First sidelobe (dB)	-17.6	-24.6	-30.6
Directivity	$0.5 \left(\frac{2\pi R}{\lambda}\right)^2$	$0.375 \left(\frac{2\pi R}{\lambda}\right)^2$	$0.28 \left(\frac{2\pi R}{\lambda}\right)^2$

4.3.2 Taylor Synthesis for Circular Apertures

Taylor [Tay60] also developed a synthesis procedure for circular apertures that is a modification of the procedure developed for line sources in Section 3.5.3. He starts with the pattern for a uniformly illuminated circular aperture $J_1(\pi u)/(\pi u)$ and removes a set of zeros from it and adds new zeros.

The roots of $J_1(\pi u)$ are the values of u_m such that

$$J_1(\pi u_m) = 0, \quad m = 1, 2, \dots \quad (4.219)$$

The Taylor pattern is obtained by removing first $(\bar{n} - 1)$ root pairs and replacing them with $(\bar{n} - 1)$ new root pairs

$$B_{TAY}(u) = \frac{J_1(\pi u)}{\pi u} \frac{\prod_{n=1}^{\bar{n}-1} \left(1 - \frac{u^2}{z_n^2}\right)}{\prod_{m=1}^{\bar{n}-1} \left(1 - \frac{u^2}{u_m^2}\right)}. \quad (4.220)$$

¹²Table follows [Jas61], [Bal82], and [Mai94].

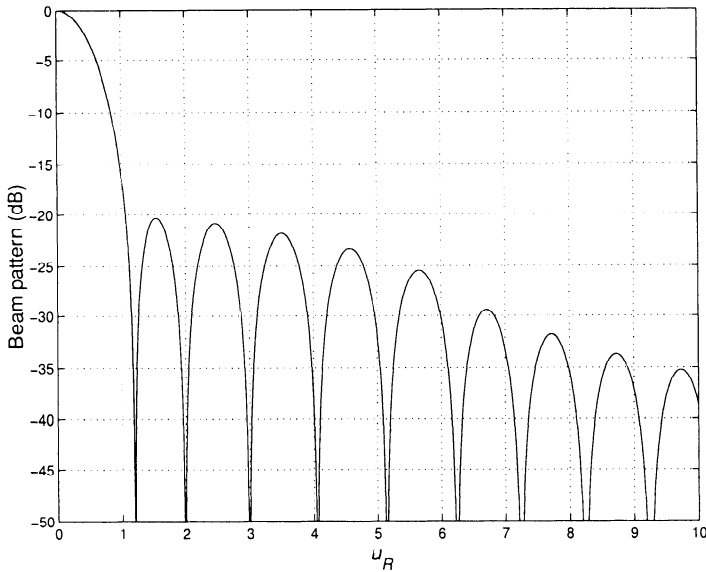


Figure 4.44 Taylor pattern for a circular aperture, $\bar{n} = 6$, -20 dB SLL; $R = 5\lambda$.

Taylor showed that the location of the new roots should be

$$z_n^2 = u_{\bar{n}}^2 \frac{A^2 + \left(n - \frac{1}{2}\right)^2}{A^2 + \left(\bar{n} - \frac{1}{2}\right)^2}, \quad (4.221)$$

where

$$A = \frac{1}{\pi} \cosh^{-1}(R_0), \quad (4.222)$$

or, in other words, $-20 \log_{10} \cosh(\pi A)$ is the desired SLL.

A representative Taylor pattern is shown in Figure 4.44 for $\bar{n} = 6$ and -20 -dB sidelobes. The radius R equals 5λ so, from (4.205), the visible region is $|u_R| \leq 10$.

To find the aperture weighting $g_0(p)$ that will produce this pattern we write $g_0(p)$ as a series

$$g_0(p) = \sum_{m=0}^{\infty} B_m J_0(u_m p), \quad (4.223)$$

where the u_m are roots of $J_1(\pi u)$ and the B_m are the coefficients in the

series. Then the pattern is

$$\begin{aligned} B_{TAY}(u) &= \sum_{m=0}^{\infty} B_m \int_0^{\pi} p J_0(u_m p) J_0(up) dp \\ &= \sum_{m=0}^{\infty} B_m \left[\frac{u_m p J_1(u_m p) J_0(up) - up J_0(u_m p) J_1(up)}{u_m^2 - u^2} \right] \Big|_0^{\pi}. \end{aligned} \quad (4.224)$$

We denote the k th zero of the uniform distribution by u_k . Now $B_{TAY}(u_k)$ is determined by a single term in the series,

$$\begin{aligned} B_{TAY}(u_k) &= B_k \int_0^{\pi} p J_0^2(u_k p) dp \\ &= B_k \left[\frac{p^2}{2} [J_0^2(u_k p) + J_1^2(u_k p)] \right] \Big|_0^{\pi} \\ &= B_k \left[\frac{\pi^2}{2} J_0^2(u_k \pi) \right]. \end{aligned} \quad (4.225)$$

Thus,

$$B_k = \frac{2}{\pi^2} \frac{B_{TAY}(u_k)}{J_0^2(u_k \pi)}. \quad (4.226)$$

Since $B_{TAY}(u_k) = 0$ for $k \geq \bar{n}$, the sum in (4.224) is finite and

$$g_0(p) = \frac{2}{\pi^2} \sum_{m=0}^{\bar{n}-1} \frac{B_{TAY}(u_m)}{J_0^2(u_m \pi)} J_0(u_m p), \quad (4.227)$$

where $B_{TAY}(u_m)$ is obtained from (4.220). The zero locations of $J_1(u_m \pi)$ are shown in Table 4.5.

Table 4.5 Zero Locations u_m for $J_1(\pi u_m)^{13}$

m	u_m	m	u_m	m	u_m	m	u_m
1	1.2196699	6	6.2439216	11	11.2466228	16	16.2476619
2	2.2331306	7	7.2447598	12	12.2468985	17	17.2477974
3	3.2383155	8	8.2453948	13	13.2471325	18	18.2479181
4	4.2410629	9	9.2458927	14	14.2473337	19	19.2480262
5	5.2439216	10	10.2462933	15	15.2475086	20	20.2481237

¹³From [Ell81].

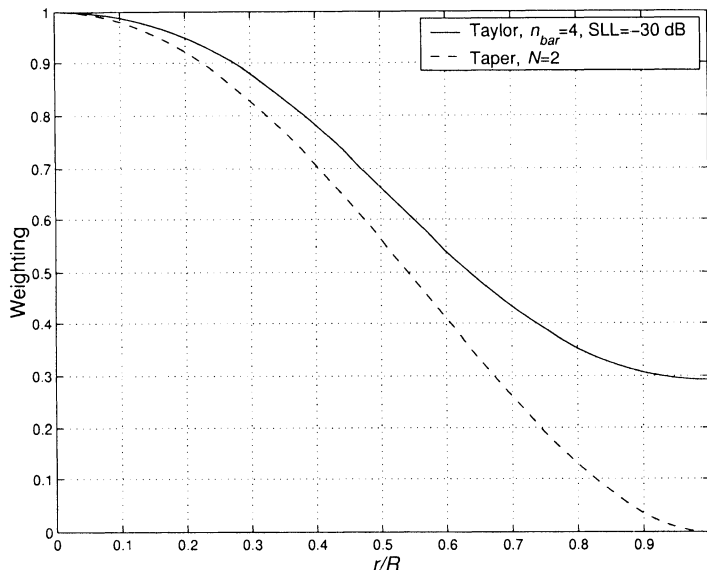


Figure 4.45 Weight function: Taylor weighting and radial taper squared weighting.

Tables of the roots of circular Taylor patterns and the corresponding aperture distributions are given in Hansen [Han59], [Han60]. Hansen [Han60] also compares the characteristics of Taylor weightings and the second-order weighting from Table 4.4. In Figure 4.45, we show the Taylor weighting function for the 30-dB sidelobe case and the second-order weighting from Table 4.3. The beam patterns for the two weightings are shown in Figure 4.46. The main-lobe beamwidth is larger using the radial taper squared, but the sidelobes decay more quickly. In Table 4.6 (from [Han60]), we show the comparative beamwidths for the Taylor weighting and the $(1 - (r/R)^2)^N$ weighting. We see that for similar first sidelobe levels there is a significant decrease in the beamwidth obtained by using the Taylor weighting. However the remaining sidelobes decrease more rapidly with the radial taper.

Table 4.6 Comparative Beamwidths

Sidelobe Level, dB	Taylor		$(1 - (r/R)^2)^N$		
	\bar{n}	Beamwidth	Sidelobe Level, dB	N	Beamwidth
25	4	$1.13\lambda/2R$	24.6	1	$1.27\lambda/2R$
30	4	$1.20\lambda/2R$	30.6	2	$1.47\lambda/2R$
35	5	$1.25\lambda/2R$	36.0	3	$1.65\lambda/2R$
40	5	$1.31\lambda/2R$	40.9	4	$1.81\lambda/2R$

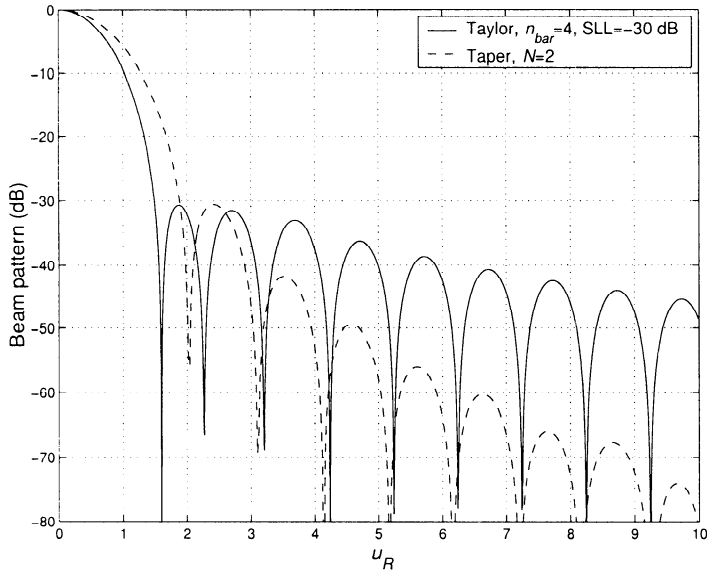


Figure 4.46 Beam patterns for Taylor weighting and radial taper squared weighting.

4.3.3 Sampling the Continuous Distribution

In many applications we approximate the circular aperture by a discrete array. In this section,¹⁴ we discuss the effect that sampling the continuous aperture function has on the beam pattern.

We first consider a rectangular array with a circular boundary. One quadrant of a 20×20 array is shown in Figure 4.47. We want to approximate the Taylor pattern in Figure 4.44.

For the nm th element, the distance from the origin is

$$d_{nm} = \left\{ \left[\frac{(2|n|-1)d_x}{2} \right]^2 + \left[\frac{(2|m|-1)d_y}{2} \right]^2 \right\}^{\frac{1}{2}}, \quad (4.228)$$

where symmetric indexing is used. Then,

$$p_{nm} = \frac{d_{nm}}{R} \quad (4.229)$$

and

$$w_{nm} = g_0(p_{nm}). \quad (4.230)$$

¹⁴This section follows Elliott [Ell81], pp. 225–230.

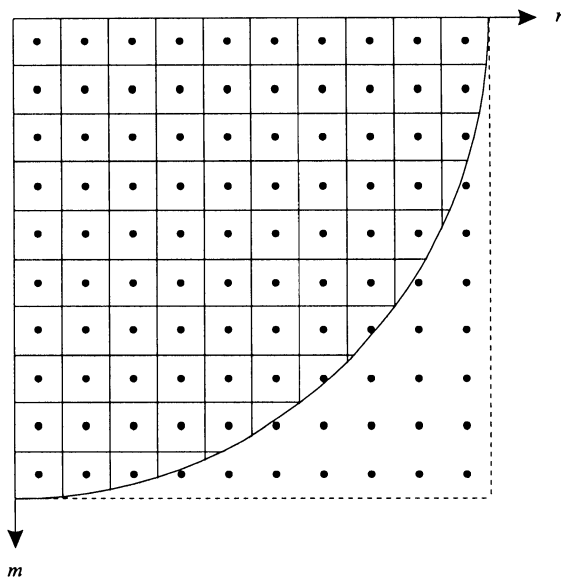


Figure 4.47 One quadrant of a rectangular grid array with circular boundary: $d_x = d_y = 0.5\lambda$, $R = 5\lambda$.

The beam pattern can be written as

$$B(\theta, \phi) = 4 \sum_{n=1}^{10} \sum_{m=1}^{10} w_{nm} \cos \left[\frac{(2n-1)\psi_x}{2} \right] \cos \left[\frac{(2m-1)\psi_y}{2} \right], \quad (4.231)$$

where

$$\psi_x = \pi \sin \theta \cos \phi, \quad (4.232)$$

$$\psi_y = \pi \sin \theta \sin \phi. \quad (4.233)$$

In Figure 4.48, we show four cuts of the pattern for $\phi = 0^\circ, 15^\circ, 30^\circ, 45^\circ$. We see that there is reasonable agreement with the continuous pattern in Figure 4.44.

In Section 4.4, we discuss hexagonal grids and their ability to generate various circular patterns.

4.3.4 Difference Beams

In Section 3.8, we explored the usage of difference patterns in linear arrays. They play a similar role in circular apertures (and arrays). In this section, we develop a general structure for difference beams.¹⁵

¹⁵Our discussion follows Section 6.11 of [Ell81].

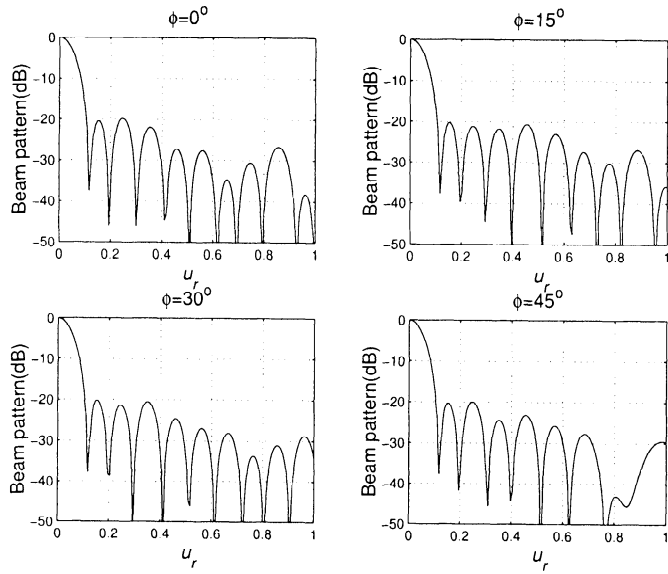


Figure 4.48 Beam pattern cuts: rectangular grid array with circular boundary; $N = 20$, SLL = -20 dB, $\bar{n} = 6$, $R = 5\lambda$, weights obtained by sampling continuous Taylor distribution.

In order to find the beam pattern we write $w(r, \phi)$ as

$$w(r, \phi) = \sum_{n=-\infty}^{\infty} w_n(r) e^{jn\phi}. \quad (4.234)$$

Then, from our discussion in Section 4.3.1 (specifically (4.192)–(4.202)), we can write the beam pattern as

$$B(\theta, \phi) = 2\pi \sum_{n=-\infty}^{\infty} (j)^n e^{jn\phi} \int_0^R w_n(r) J_n(k_r \sin \theta) r dr. \quad (4.235)$$

In Section 4.3.1 we focused on the case in which only w_0 was non-zero.

In order to construct a difference beam we look at the special case in which only the $n = \pm 1$ weights are non-zero. We denote this difference beam as $D(\theta, \phi)$. Letting $n = \pm 1$ in (4.235) gives

$$\begin{aligned} D(\theta, \phi) = 2\pi j \int_0^R & \left[e^{j\phi} w_1(r) J_1(k_r \sin \theta) \right. \\ & \left. - e^{-j\phi} w_{-1}(r) J_{-1}(k_r \sin \theta) \right] r dr. \end{aligned} \quad (4.236)$$

Since $J_{-1}(x) = -J_1(x)$, if we set $w_{-1}(r) = w_1(r)$, then (4.234) becomes

$$w(r, \phi) = 2w_1(r) \cos \phi, \quad (4.237)$$

and (4.236) becomes

$$D(\theta, \phi) = 4\pi j \cos \phi \int_0^R w_1(r) J_1(k_r \sin \theta) r dr. \quad (4.238)$$

We see that the resulting pattern is of the form

$$D_\alpha(\theta, \phi) = 4\pi j \cos \phi D_\theta(\theta), \quad (4.239)$$

where $D_\theta(\theta)$ is the integral in (4.238). Now consider a cut of the pattern through any plane containing the z -axis. Then,

$$D_\alpha(\theta, \phi) = 4\pi j \cos \phi D_\theta(\theta), \quad (4.240)$$

and

$$D_\alpha(\theta, \phi + \pi) = -4\pi j \cos \phi D_\theta(\theta), \quad (4.241)$$

which give a difference pattern in the various planes containing the z -axis. The function $D_\theta(\theta)$ is weighted with $\cos \phi$ so the maximum slope is in the xz -plane and the function is zero in the yz -plane.

To develop a useful difference pattern for the yz -plane, we set $w_{-1}(r) = -w_1(r)$. Then,

$$w(r, \phi) = 2jw_1(r) \sin \phi, \quad (4.242)$$

$$D_\beta(\theta, \phi) = -4\pi \sin \phi D_\theta(\theta). \quad (4.243)$$

This difference pattern provides maximum slope in the yz -plane. Thus, we utilize a beamspace consisting of a sum beam and two difference beams $D_\alpha(\theta, \phi)$ and $D_\beta(\theta, \phi)$. The shape of the difference patterns is determined by $D_\theta(\theta)$. We now focus on how the aperture weighting function affects $D_\theta(\theta)$.

Defining

$$u = \frac{2R}{\lambda} \sin \theta, \quad p = \frac{\pi r}{R}, \quad (4.244)$$

we can write $D_\theta(\theta)$ as,

$$D_\theta(u) = \left(\frac{R}{\pi} \right)^2 \int_0^\pi w_1(p) J_1(up) p dp. \quad (4.245)$$

In order to perform the integration, we expand $w_1(p)$ in an orthogonal expansion of Bessel functions,

$$w_1(p) = \sum_{m=0}^{\infty} A_m J_1(u_m p), \quad (4.246)$$

where the u_m are eigenvalues that we will define shortly. Using (4.246) in (4.245) gives

$$\begin{aligned} D_\theta(u) &= \left(\frac{R}{\pi}\right)^2 \sum_{m=0}^{\infty} A_m \int_0^\pi J_1(u_m p) J_1(up) p dp \\ &= \left(\frac{R}{\pi}\right)^2 \sum_{m=0}^{\infty} A_m \left[\frac{u_m p J_1(up) J_0(u_m p) - up J_0(up) J_1(u_m p)}{u^2 - u_m^2} \right] \Big|_0^\pi. \end{aligned} \quad (4.247)$$

Since $vJ_0(v) = J_1(v) + vJ'_1(v)$, where the prime denotes differentiation, (4.247) can be rewritten as

$$\begin{aligned} D_\theta(u) &= \left(\frac{R}{\pi}\right)^2 \sum_{m=0}^{\infty} A_m \left[\frac{u_m p J'_1(u_m p) J_1(up) - up J'_1(up) J_1(u_m p)}{u^2 - u_m^2} \right] \Big|_0^\pi \\ &= \left(\frac{R}{\pi}\right)^2 \sum_{m=0}^{\infty} A_m \frac{\pi u_m J'_1(\pi u_m) J_1(\pi u) - \pi u J'_1(\pi u) J_1(\pi u_m)}{u^2 - u_m^2}. \end{aligned} \quad (4.248)$$

To get $D_\theta(u_n)$ equal to zero for $n \neq m$, we require either $J_1(\pi u_m) = 0$ or $J'_1(\pi u_m) = 0$. The first choice requires $w_1(\pi) = 0$, which is undesirable, so we use the second option. The u_m are the zeros of $J'(\pi u)$, so

$$J'(\pi u_m) = 0; \quad (4.249)$$

then (4.248) becomes

$$D_\theta(u) = \left(\frac{R}{\pi}\right)^2 \sum_{m=0}^{\infty} A_m J_1(\pi u_m) \frac{\pi u J'_1(\pi u)}{u_m^2 - u^2}. \quad (4.250)$$

The zeros of $J'_1(x)$ are tabulated (e.g., p. 252 of [Ell81]). The first 10 zeros are shown in Table 4.7.

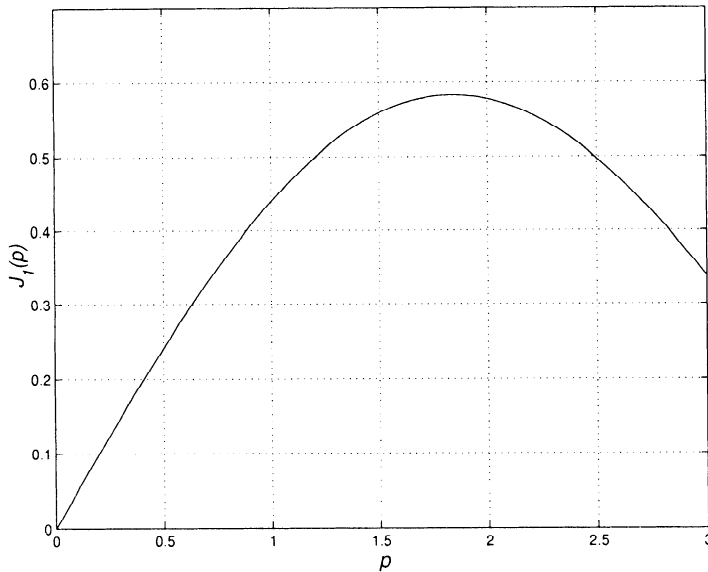


Figure 4.49 Aperture distribution for generic difference pattern: $v = 0.586p$.

Table 4.7 Bessel Function Zeros, $J'_1(\pi u_m) = 0$

m	u_m	m	u_m
0	0.5860670	5	5.7345205
1	1.6970509	6	6.7368281
2	2.7171939	7	7.7385356
3	3.7261370	8	8.7398505
4	4.7312271	9	9.7408945

We now consider the simple case in which there is a single term corresponding to $m = 0$. In this case,

$$D_\theta(u) = \left(\frac{R}{\pi}\right)^2 \frac{A_0 J_1(0.586\pi)}{(0.586)^2} \left[\frac{\pi u J'_1(\pi u)}{1 - \left(\frac{u}{0.586}\right)^2} \right]. \quad (4.251)$$

The aperture weighting $J_1(0.586p)$ is shown in Figure 4.49 and the beam pattern is shown in Figure 4.50. We see that the first sidelobe is at about -14 dB. We would like to preserve an adequate slope at the origin and decrease the height of the sidelobes.

This problem is analogous to the linear array problem that led to a Bayliss difference pattern. Bayliss [Bay68] also derived the difference pattern for a circular aperture.

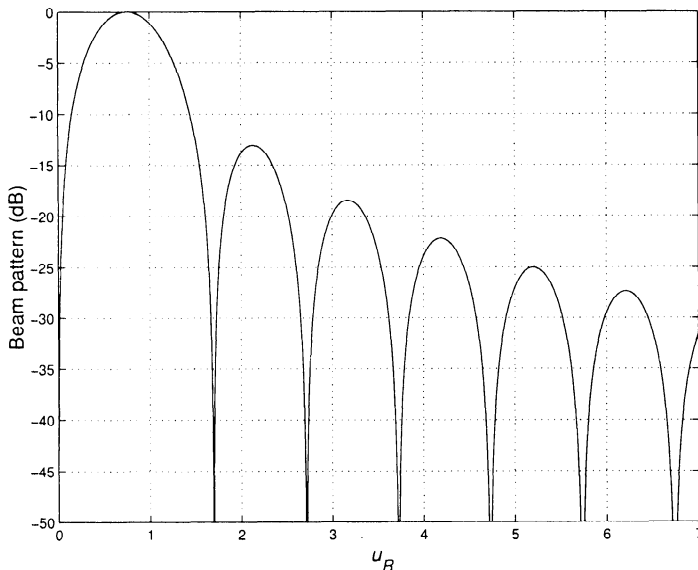


Figure 4.50 Beam pattern for generic aperture distribution: $u_R = 2R \sin \theta / \lambda$.

The reader should consult the above reference for a discussion of Bayliss difference patterns for circular apertures.

A sum beam and two difference beams are often used to estimate (θ, ϕ) of a signal (or target). In later chapters, we use these beams to do beamspace processing.

4.3.5 Summary

In Sections 4.3.1 and 4.3.2 we developed techniques for synthesizing beam patterns for circular apertures. Our emphasis was on patterns in which the weighting in the ϕ -direction was uniform. However, the relationships in (4.200)–(4.203) can be extended to include non-uniform weightings. We found that uniform weighting leads to a $J_1(\psi_R)/\psi_R$ beam pattern. We developed a family of radial taper weightings and Taylor weightings that resulted in lower sidelobes.

In Section 4.3.3, we discussed sampling the continuous distribution using a rectangular grid. Although the performance was satisfactory, we will find that the hexagonal grid in Section 4.4 provides a better approach. In Section 4.3.4, we developed techniques for synthesizing difference beams.

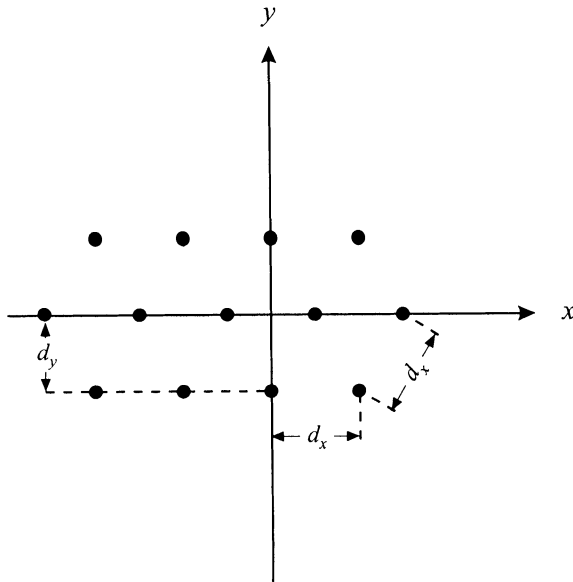


Figure 4.51 Configuration of a typical hexagonal array.

4.4 Hexagonal Arrays

4.4.1 Introduction

In this section, we discuss arrays whose elements are located on a hexagonal (or equilateral triangular) grid, as shown in Figure 4.51. The horizontal interelement spacing is d_x and the vertical spacing between rows is

$$d_y = \frac{\sqrt{3}}{2}d_x. \quad (4.252)$$

The motivation for using hexagonal-grid arrays can be approached from three viewpoints. The first viewpoint emphasizes that the array is sampling a spatial field. Peterson and Middleton [PM62] showed that hexagonal sampling is the optimum sampling strategy for signals that are bandlimited over a circular region of the Fourier plane. In the array case, this corresponds to the visible region,

$$u_x^2 + u_y^2 \leq 1. \quad (4.253)$$

We revisit this viewpoint in Chapter 5.

The second viewpoint emphasizes the grating lobe viewpoint. Sharp [Sha61] shows that if the main beam is required to scan inside a cone whose

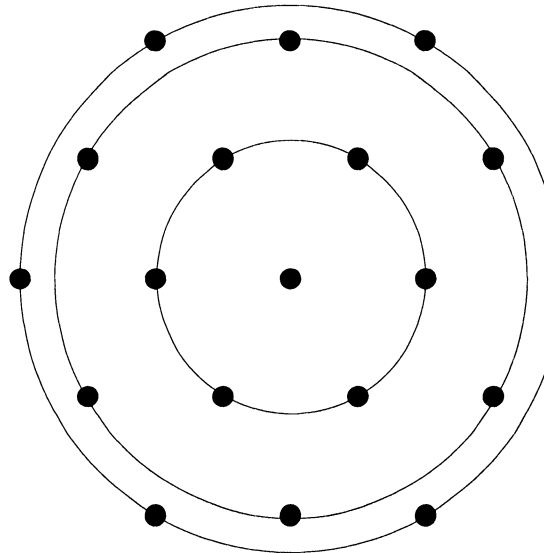


Figure 4.52 Nineteen-element hexagonal arrays.

axis is normal to the array, then the number of elements can be reduced by 13.4%.

A third viewpoint emphasizes the circular symmetry of many desired beam patterns. To illustrate this point, consider the 19-element hexagonal array in Figure 4.52. The hexagonal grid causes the elements to be arranged in concentric circles. From the discussion in Section 4.1, we would anticipate that the hexagonal array would be an efficient arrangement.

Our discussion will focus on triangular-grid arrays that have six equal sides with

$$d_x = \frac{\lambda}{2}, \quad (4.254)$$

and

$$d_y = \frac{\sqrt{3}}{4} \lambda. \quad (4.255)$$

We refer to these as **standard hexagonal arrays (SHA)**. The total number of elements will be 7, 19, 37, 61, ⋯,

$$N_H = 1 + \sum_{n=1}^{\frac{N_x-1}{2}} 6n, \quad (4.256)$$

where N_x is the number of elements in the horizontal row through the origin,

and N_x is odd in order to get a symmetric array. Standard hexagonal arrays with $N_H = 7$ and 19 are shown in Figure 4.53.

This configuration is useful whenever the desired beam pattern is circularly symmetric. An application that uses a similar configuration is a geostationary military satellite operating at 8 GHz that uses a 19-beam multiple beam antenna for reception and 61-beam multiple beam antenna for transmission.

Our discussion of hexagonal arrays is reasonably short because many of the rectangular-grid techniques can be applied directly to hexagonal arrays by using an appropriate coordinate system.

In Section 4.4.2, we discuss several beam pattern design techniques that are representative of possible approaches.

In Section 4.4.3, we discuss a hexagonal-grid to rectangular-grid transformation that will be useful for several applications.

In Section 4.4.4, we summarize our results.

4.4.2 Beam Pattern Design

In this section we discuss techniques for beam pattern design for standard hexagonal arrays. To illustrate the notation, consider the standard 19-element hexagonal array shown in Figure 4.53(b). Each horizontal row of sensors is indexed with the variable n , which ranges from $n = 0$ to $n = N_r - 1$, where N_r is the number of elements in the row. The rows are indexed by the variable m , which ranges from $-(N_x - 1)/2$ to $(N_x - 1)/2$. We see that $N_r = N_x - |m|$.

We define a 19-element array manifold vector as,

$$\text{vec}_H(u_x, u_y) = \begin{bmatrix} \mathbf{v}_2^T & \mathbf{v}_1^T & \mathbf{v}_0^T & \mathbf{v}_{-1}^T & \mathbf{v}_{-2}^T \end{bmatrix}^T, \quad (4.257)$$

where

$$\mathbf{v}_2 = e^{j\pi\sqrt{3}u_y} \begin{bmatrix} e^{-j\pi u_x} & 1 & e^{j\pi u_x} \end{bmatrix}^T, \quad (4.258)$$

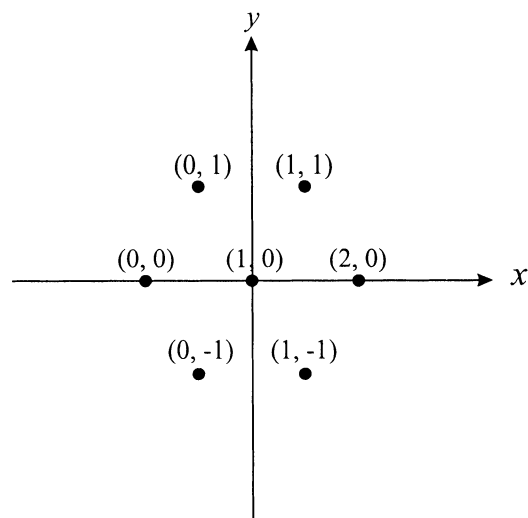
$$\mathbf{v}_1 = e^{j\pi\frac{\sqrt{3}}{2}u_y} \begin{bmatrix} e^{-j\pi\frac{3u_x}{2}} & e^{-j\pi\frac{u_x}{2}} & e^{j\pi\frac{u_x}{2}} & e^{j\pi\frac{3u_x}{2}} \end{bmatrix}^T, \quad (4.259)$$

$$\mathbf{v}_0 = \begin{bmatrix} e^{-j2\pi u_x} & e^{-j\pi u_x} & 1 & e^{j\pi u_x} & e^{j2\pi u_x} \end{bmatrix}^T, \quad (4.260)$$

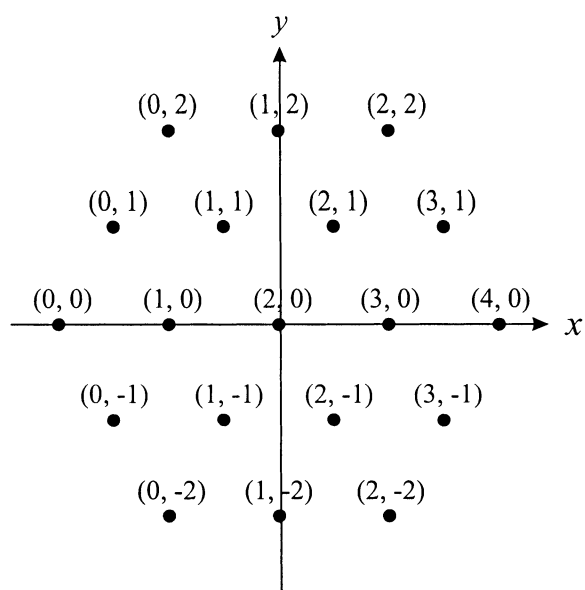
$$\mathbf{v}_{-1} = e^{-j\pi\frac{\sqrt{3}}{2}u_y} \begin{bmatrix} e^{-j\pi\frac{3u_x}{2}} & e^{-j\pi\frac{u_x}{2}} & e^{j\pi\frac{u_x}{2}} & e^{j\pi\frac{3u_x}{2}} \end{bmatrix}^T, \quad (4.261)$$

$$\mathbf{v}_{-2} = e^{-j\pi\sqrt{3}u_y} \begin{bmatrix} e^{-j\pi u_x} & 1 & e^{j\pi u_x} \end{bmatrix}^T. \quad (4.262)$$

We see that $\text{vec}_H(u_x, u_y)$ is conjugate symmetric.



(a)



(b)

Figure 4.53 Configurations of standard hexagonal arrays: (a) $N_H = 7$; (b) $N_H = 19$.

For a standard hexagonal array with N_x elements along the x -axis, the nm th term in the array manifold vector is

$$[vec_H(u_x, u_y)]_{nm} = \exp \left\{ j\pi \left[m \frac{\sqrt{3}}{2} u_y + n u_x - \frac{N_x - |m| - 1}{2} u_x \right] \right\}. \quad (4.263)$$

The beam pattern is

$$B_u(u_x, u_y) = \sum_{m=-\frac{N_x-1}{2}}^{\frac{N_x-1}{2}} w_{nm}^* \exp \left\{ j\pi \left[m \frac{\sqrt{3}}{2} u_y + \frac{N_x - |m| - 1}{2} u_x \right] \right\} \cdot \sum_{n=0}^{N_x - |m| - 1} \exp \{j\pi n u_x\}. \quad (4.264)$$

For uniform weighting,

$$w_{nm} = \frac{1}{N_H}, \quad (4.265)$$

and

$$B_u(u_x, u_y) = \frac{1}{N_H} \sum_{m=-\frac{N_x}{2}}^{\frac{N_x}{2}} \exp \left\{ j\pi \left[m \frac{\sqrt{3}}{2} u_y - \frac{N_x - |m| - 1}{2} u_x \right] \right\} \cdot \sum_{n=0}^{N_x - |m| - 1} \exp \{j\pi n u_x\}. \quad (4.266)$$

We first consider a design approach in which we construct the desired weighting for the circular aperture using the techniques in Section 4.3. We then sample the aperture weighting on a hexagonal grid to find the element weightings.

To match the hexagonal array to the continuous aperture, we observe that, if R is the radius of the continuous aperture and $2R/\lambda$ is an integer, then

$$R = \frac{N_x}{4} \lambda. \quad (4.267)$$

In our examples, we use $N_x = 11$, which corresponds to a standard hexagonal array with 91 elements.

Example 4.4.1

Consider a SHA with 91 elements with uniform weighting. Then $B_u(u_x, u_y)$ is given by (4.266), with $N_x = 11$ and $N_H = 91$.

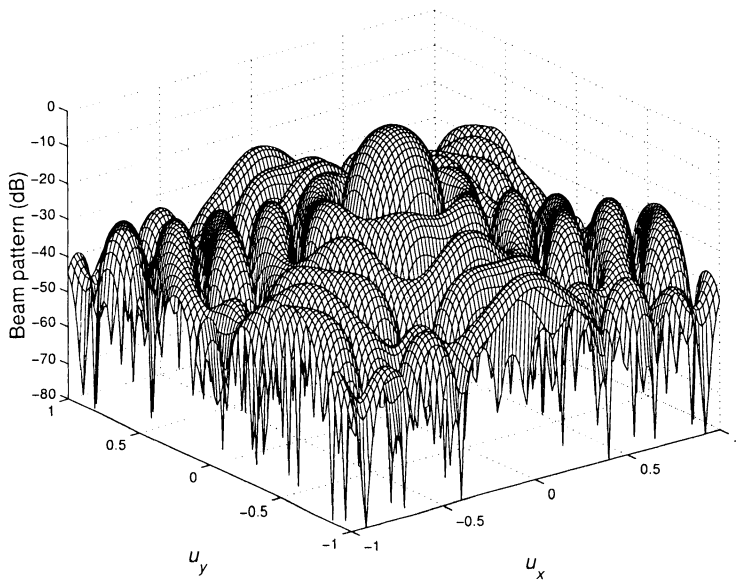


Figure 4.54 Beam pattern of a standard 91-element hexagonal array with uniform weighting.

The beam pattern is shown in Figure 4.54. A contour plot in Figure 4.55 shows the 6-fold symmetry inside the visible region. Beam pattern cuts at $\phi = 0^\circ, 10^\circ, 20^\circ$, and 30° are shown in Figure 4.56. The horizontal axis is $u_r = (u_x^2 + u_y^2)^{\frac{1}{2}}$. These pattern cuts can be compared to the beam pattern of the circular aperture in Figure 4.43. The main lobe and the first sidelobe are almost identical, but the other sidelobes vary from those of the aperture.

In order to reduce the sidelobes we can use a radial taper from Table 4.4.

Example 4.4.2

Consider a standard 91-element hexagonal array. We start with the radial taper in column 2 of Table 4.4.

$$w_R(r) = 1 - \left(\frac{r}{R} \right)^2, \quad 0 \leq r \leq R, \quad (4.268)$$

where

$$R = 2.75\lambda. \quad (4.269)$$

We choose the hexagonal array weights using

$$w_{nm} = 1 - \frac{\left(\left(n - \frac{N_x - |m| - 1}{2} \right) \frac{\lambda}{2} \right)^2 + \left(m \frac{\sqrt{3}}{4} \lambda \right)^2}{R^2}. \quad (4.270)$$

The hexagonal array beam pattern is shown in Figure 4.57 with pattern cuts in Figure 4.58.

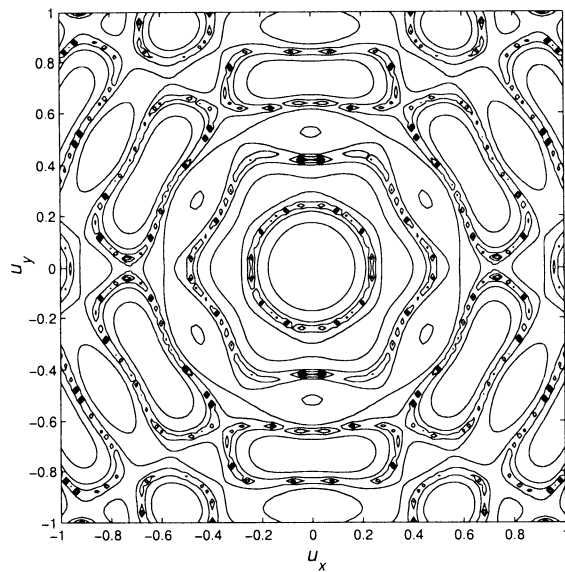


Figure 4.55 Contour plot of a standard 91-element hexagonal array with uniform weighting.

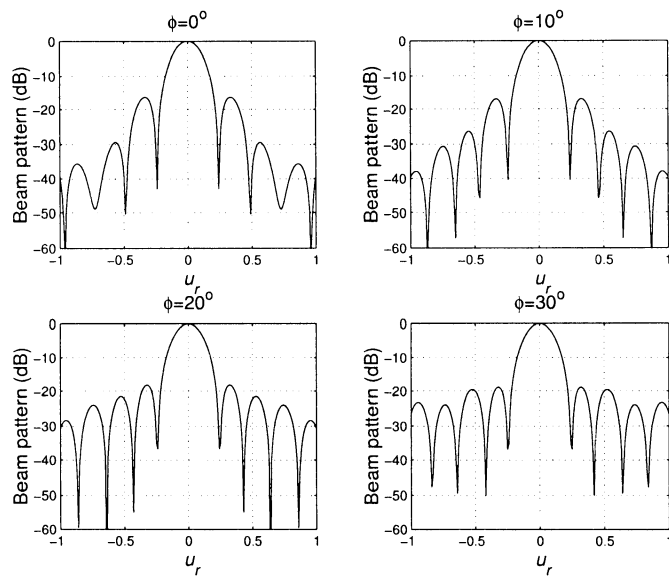


Figure 4.56 Beam pattern cuts of a standard 91-element hexagonal array with uniform weighting: (a) $\phi = 0^\circ$; (b) $\phi = 10^\circ$; (c) $\phi = 20^\circ$; (d) $\phi = 30^\circ$.

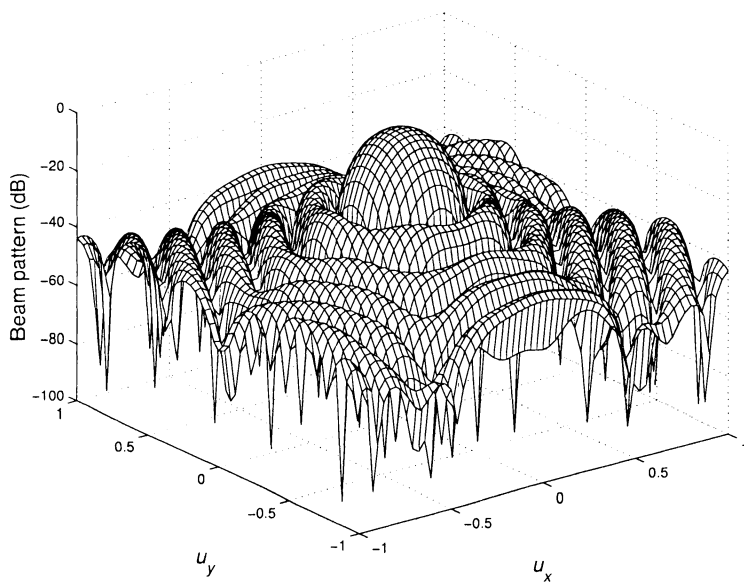


Figure 4.57 Beam pattern of a standard 91-element hexagonal array: radial taper, $R = 2.75\lambda$.

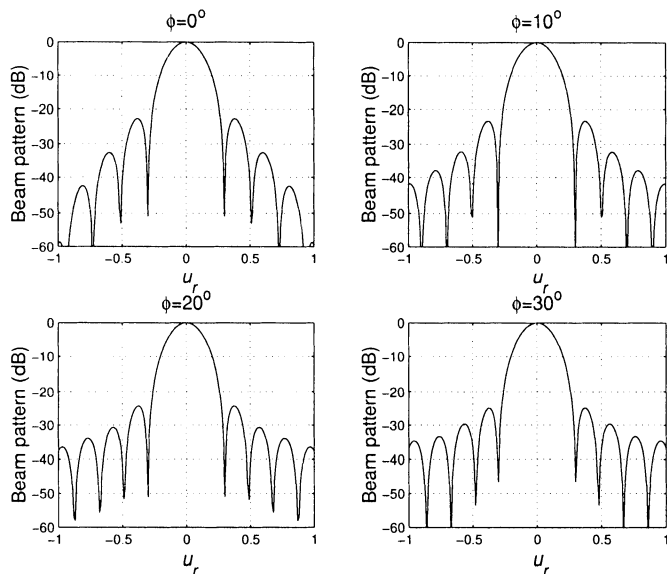


Figure 4.58 Cuts through beam pattern of a standard 91-element hexagonal array with radial taper: $R = 2.75\lambda$.

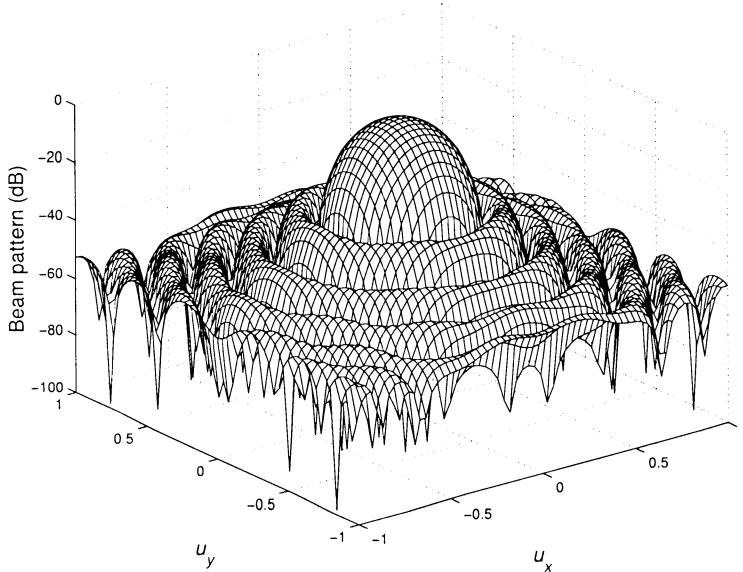


Figure 4.59 Beam pattern of a standard 91-element hexagonal array with radial taper squared weighting: $R = 2.75\lambda$.

The corresponding beam patterns for the weighting in column three of Table 4.4 are shown in Figures 4.59 and 4.60.

As expected, the sidelobe levels are much lower and the main lobe is wider for both radial tapers in comparison to the uniform weightings.

In Example 4.4.2, we have assumed that the desired radial weighting function is known. An alternative approach is to assume that the desired beam pattern is known and use (3.156) to find the weight vector.

If we desire a Dolph-Chebychev beam pattern in each cross section, we use (4.111) :

$$B_\psi(\psi_x, \psi_y) = \frac{T_{N-1}(x_o \cos \frac{\psi_x}{2} \cos \frac{\psi_y}{2})}{R}, \quad (4.271)$$

to generate the desired beam pattern. We sample the resulting beam pattern at N_H points and use (3.156) to find w_{nm} .

If we desire a Taylor beam pattern, we use (4.220) and (4.221) to generate the desired beam pattern. We sample the resulting beam pattern at N_H points and use (3.156) to find w_{nm} .

In both cases, it is important to choose a sampling grid that gives a well-conditioned $\mathbf{V}^H(\psi)$. Several examples are developed in the problems. A Dolph-Chebychev example is done in Problem 4.4.5. The results indicate that the resulting beam pattern is sensitive to the sampling grid and the choice of N_H .

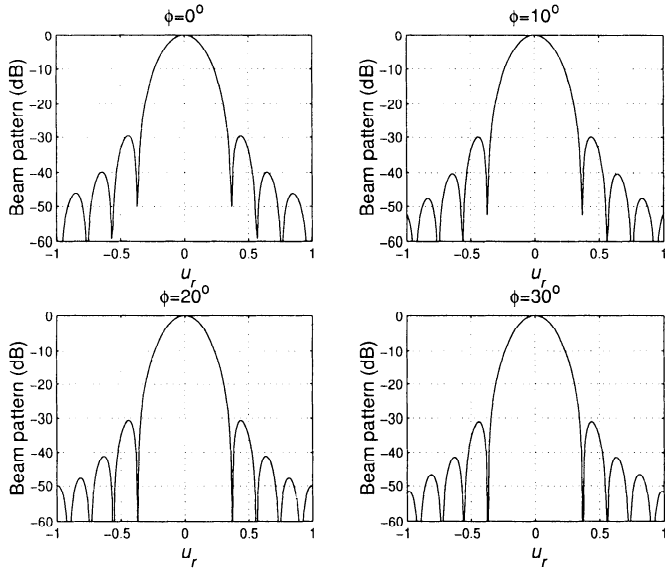


Figure 4.60 Cuts through beam pattern for a standard 91-element hexagonal array with radial taper squared weighting: $R = 2.75\lambda$; (a) $\phi = 0^\circ$; (b) $\phi = 10^\circ$; (c) $\phi = 20^\circ$; (d) $\phi = 30^\circ$.

4.4.3 Hexagonal Grid to Rectangular Grid Transformation

Most of the Fourier transform relationships that we used for beam pattern design and analysis can be utilized with hexagonal arrays by defining a suitable hexagonal Fourier transform or hexagonal DFT. An excellent discussion of hexagonal signal processing is contained in Mersereau [Mer79].

We use an approach due to Lo and Lee [LL83] that is similar and adequate for our purposes. The basic idea is to map the hexagonal array into an equivalent rectangular grid array and formulate the processing using the equivalent array.

In Figure 4.61(b), we show a 19-element standard hexagonal array. In Figure 4.61(a) we show a 19-element array on a standard rectangular grid ($d = \lambda/2$). To obtain the rectangular grid array, we have rotated and stretched the hexagonal grid array.

We write the beam pattern of the rectangular grid array in \mathbf{v} -space,

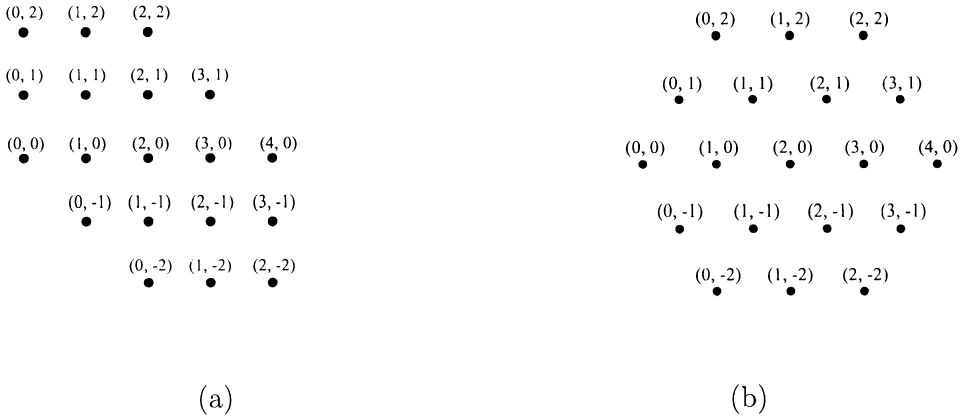


Figure 4.61 Hexagonal-rectangular transformation.

$$B_{\mathbf{v}}(v_x, v_y) = \sum_{m=-\frac{N_x-1}{2}}^{\frac{N_x-1}{2}} w_{nm}^* \exp \left\{ j\pi \left[mv_y - \frac{N_x - |m| - 1}{2} v_x - \frac{m}{2} v_x \right] \right\} \cdot \sum_{n=0}^{N_x - |m| - 1} \exp j\pi n v_x, \quad (4.272)$$

where

$$v_x = \sin \theta_r \cos \phi_r, \quad (4.273)$$

and

$$v_y = \sin \theta_r \sin \phi_r, \quad (4.274)$$

and the subscript “r” denotes rectangular.

Comparing the expressions in (4.272) and (4.264), we obtain the relation between \mathbf{u} -space and \mathbf{v} -space,

$$v_x = u_x \quad (4.275)$$

and

$$v_y = \frac{u_x}{2} + \frac{\sqrt{3}}{2} u_y, \quad (4.276)$$

or

$$\mathbf{v} = \begin{bmatrix} 1 & 0 \\ \frac{1}{2} & \frac{\sqrt{3}}{2} \end{bmatrix} \mathbf{u} \quad (4.277)$$

and

$$\mathbf{u} = \begin{bmatrix} 1 & 0 \\ -\frac{1}{\sqrt{3}} & \frac{2}{\sqrt{3}} \end{bmatrix} \mathbf{v}. \quad (4.278)$$

We can take any hexagonal array and map it into an equivalent rectangular-grid array. The motivation for this transformation is that we will find several array processing algorithms that work well on rectangular arrays. We implement these algorithms on the rectangular grid array and then transform the results from \mathbf{v} -space to \mathbf{u} -space.

4.4.4 Summary

In this section, we have studied arrays whose elements are located on a hexagonal (or equilateral-triangular) grid. The grid provides an efficient spatial sampling strategy and is widely used in practice.

In Section 4.4.2, we considered standard hexagonal arrays and assumed that we had synthesized the desired beam pattern using a continuous circular aperture. We then sampled the continuous aperture weighting on a hexagonal grid to obtain the array beam pattern.

In Section 4.4.3, we introduced a hexagonal-grid to rectangular-grid transformation that will enable us to use techniques developed for rectangular grids to solve hexagonal-grid problems. We find this transformation to be useful in several optimal array processing algorithms.

A number of other hexagonal-grid array issues are developed in the problems.

4.5 Nonplanar Arrays

In many applications of interest the physical location of the sensors must conform to the shape of the curved surface that they are mounted on. Examples include arrays mounted on submarines, aircraft, or missiles. These arrays are referred to as **conformal arrays**, and their properties are discussed in numerous references.

References that discuss various aspects of conformal arrays include Boriootti [Bor87], Hansen [Han81], Mailloux [Mai84], Antonucci and Franchi [AF85], Hansen [Han98], and Kummer et al. [KSV73].

A complete discussion of the issues associated with the various conformal array geometries would take us too far afield, so we will restrict our attention to two commonly used geometries: cylindrical and spherical. We discuss cylindrical arrays in Section 4.5.1 and spherical arrays in Section 4.5.2.

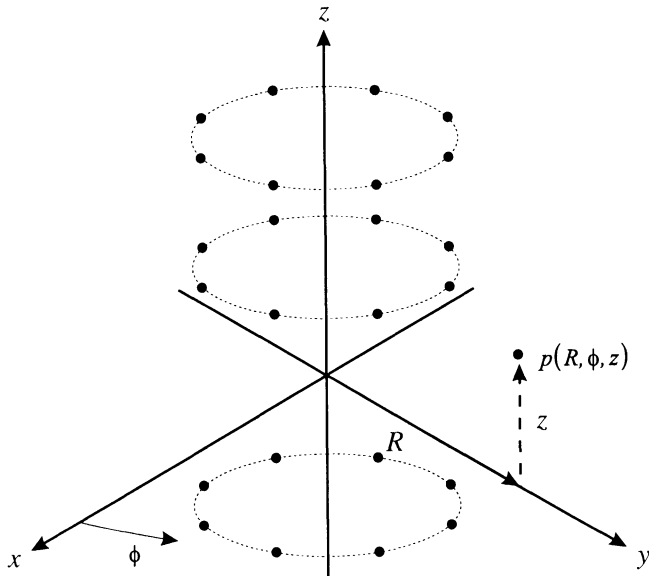


Figure 4.62 Cylindrical array geometry and the cylindrical coordinate system.

4.5.1 Cylindrical Arrays

The cylindrical array geometry and the cylindrical coordinate system are shown in Figure 4.62.

The element beam pattern are assumed to be isotropic. The beam pattern is given by

$$B(\theta, \phi) = \sum_{n=-\frac{N-1}{2}}^{\frac{N-1}{2}} \sum_{m=1}^M w_{nm}^* e^{-j\mathbf{k}^T \mathbf{p}_{nm}}, \quad N \text{ odd}, \quad (4.279)$$

where N is the number of circular arrays and M is the number of elements in each circular array. The center of the circular arrays is the z -axis and the array is symmetric in the z -direction about the origin.

We can use the discrete version of (4.134) to write

$$B(\theta, \phi) = \sum_{n=-\frac{N-1}{2}}^{\frac{N-1}{2}} \sum_{m=1}^M w_{nm}^* e^{j k_0 [R \sin \theta \cos(\phi - \phi_1) + z_n \cos \theta]}. \quad (4.280)$$

This can be written as

$$B(\theta, \phi) = \sum_{n=-\frac{N-1}{2}}^{\frac{N-1}{2}} e^{jk_0 z_n \cos \theta} \left\{ \sum_{m=1}^M w_{nm}^* e^{jk_0 R \sin \theta \cos(\phi - \phi_m)} \right\}. \quad (4.281)$$

The term in the braces is just the beam pattern of the n th circular array. Thus,

$$B(\theta, \phi) = \sum_{n=-\frac{N-1}{2}}^{\frac{N-1}{2}} e^{jk_0 z_n \cos \theta} B_{cir,n}(\theta, \phi), \quad (4.282)$$

which is analogous to the beam pattern of a linear array with

$$w_n^* = B_{cir,n}(\theta, \phi). \quad (4.283)$$

If w_{nm}^* in (4.280) is separable,

$$w_{nm}^* = w_n^* w_m^*, \quad (4.284)$$

then (4.281) reduces to

$$\begin{aligned} B(\theta, \phi) &= \sum_{n=-\frac{N-1}{2}}^{\frac{N-1}{2}} w_n^* e^{jk_0 z_n \cos \theta} B_{cir}(\theta, \phi) \\ &= B_{lin}(\theta, \phi) B_{cir}(\theta, \phi), \end{aligned} \quad (4.285)$$

which is the pattern multiplication result from Chapter 2 (2.235).

We consider an example to illustrate a typical pattern.

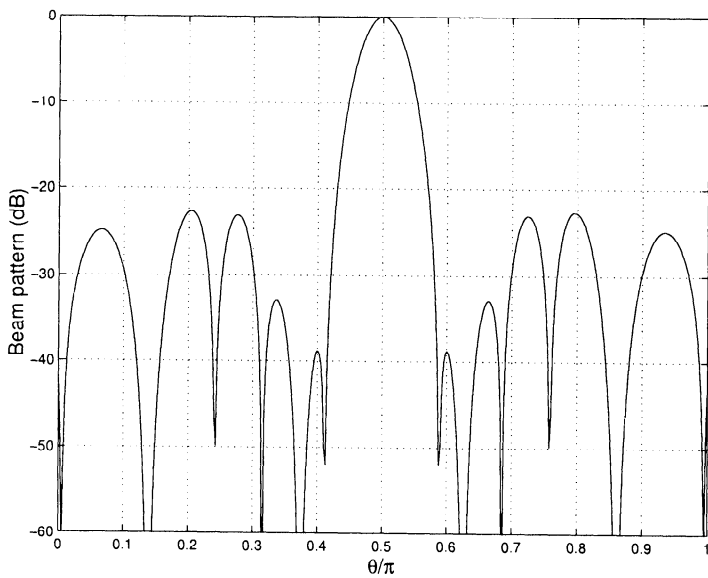
Example 4.5.1

We consider a cylindrical array consisting of 11 circular arrays with radius $2\pi R = 10\lambda$. We assume that $M = 25$ so that we can utilize 21 phase modes.

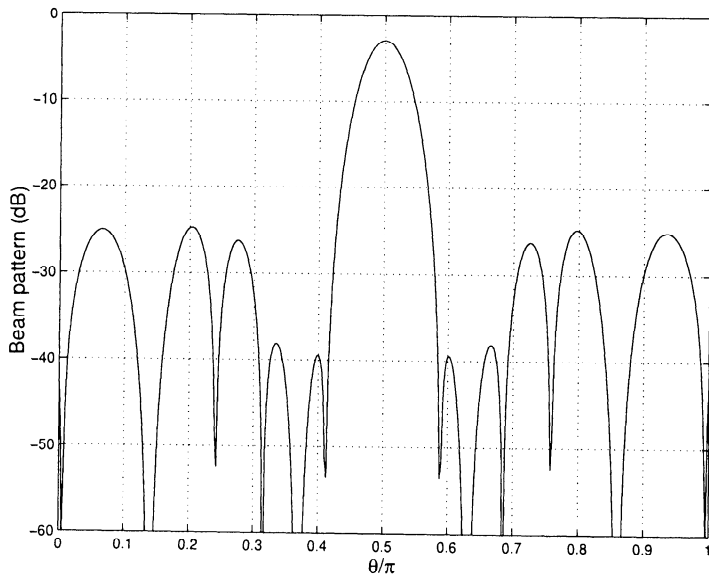
We want to create a beam with a narrow beamwidth pointed at $\theta = 0, \phi = 0$. We use Dolph-Chebychev weighting in the z -direction and the Villenueve uniform phase mode excitation from Example 4.2.1 for each circular array.

The resulting beam pattern is shown in Figure 4.63. We see that it has acceptable sidelobe behavior.

In many, if not most, applications the elements will have a non-isotropic beam pattern. As in the ring array case, the main response axis of the element pattern will point in a radial direction. Synthesis of a desirable beam pattern is more complicated, but the techniques in Section 3.9.3 are applicable.



(a)



(b)

Figure 4.63 Beam pattern cuts at $\phi = 0$ and $\phi = 0.045\pi$.

In many applications, the main response axis is scanned in azimuth and only the elements in a section around the MRA are utilized at a particular time. The techniques in Section 3.9.3 are also applicable to this problem.

References that discuss various aspects of cylindrical and cylindrical sector arrays include Hansen [Han98], James [Jam47], Lee and Lo [LL65], Harrington and Lepage [HL52], Hessel [Hes70], Munger and Gladman [MG70], Sheleg [She75], Borgiotti and Balzano [BB72], and Knudsen [Knu59].

4.5.2 Spherical Arrays

Arrays with elements on a spherical surface are used for various applications. In most cases, the array extends over a hemisphere. In other cases, the entire sphere is used.

References that discuss various aspects of spherical arrays include Schrank [Sch72], Hoffman [Hof63], Chan et al. [CIS68], Sengupta et al. [SSL68], and MacPhie [MP68]. Pattern coverage and grating lobes issues are discussed in these references.

We confine our discussion to an expression for the beam pattern. The spherical coordinate system was shown in Figure 2.1. The n th element of the array manifold vector is

$$[\mathbf{v}_k(k)]_n = \exp(-jk^T \mathbf{p}_n), \quad (4.286)$$

and the beam pattern is

$$B(\theta, \phi) = \sum_{n=1}^N w_n \exp(-jk^T \mathbf{p}_n). \quad (4.287)$$

Expressing \mathbf{k} and \mathbf{p} in spherical coordinates, we can write the beam pattern as

$$\begin{aligned} B(\theta, \phi) &= \sum_{n=1}^N w_n \exp \{ jk_0 R [\sin \theta \sin \theta_n \cos(\phi - \phi_n) \\ &\quad + \cos \theta \cos \theta_n] \}, \end{aligned} \quad (4.288)$$

where R is the radius of the sphere. For non-isotropic elements, the expression in (4.288) must be modified to include the element patterns. The technique in Section 3.9.3 can be used to synthesize a desired beam pattern. Several examples are developed in the problems.

4.6 Summary

In this chapter, techniques for analyzing and synthesizing planar arrays have been developed. The chapter focused on the array geometries: rectangular, rings, circular apertures, and hexagonal arrays that are commonly used in practice.

Section 4.1 considered arrays with sensors on a uniformly spaced rectangular grid. Many of the techniques developed for linear arrays carried over to rectangular grid arrays. Separable weightings produced sidelobe behavior that varied significantly as ϕ changed. Circularly symmetric weightings were developed to improve the behavior.

Section 4.2 considered ring apertures and ring arrays. The function $J_o(\cdot)$ played the same role in a ring aperture that $\text{sinc}(\cdot)$ did for a linear aperture. Phase mode excitation beamformers were developed that allowed the use of linear array weightings to synthesize desirable beam patterns.

Section 4.3 consider circular apertures. The discussion focussed on weighting functions that were separable in polar coordinates. Most of the examples consider desired beam patterns that were uniform in ϕ -space (a circularly symmetric pattern). A family of radial tapers was developed that were effective in controlling the sidelobe levels (Table 4.4). Synthesis of Taylor beam patterns was also developed. Techniques for synthesizing difference beams were developed.

Section 4.4 considered arrays whose sensors were located on an equilateral triangular grid that produced a hexagonal array. The elements lie on a set of concentric circles so the array is particularly suited to cases in which the desired beam pattern has circular symmetry. Beam pattern design techniques were developed. A hexagonal-to-rectangular transformation was developed that is useful in various applications.

Section 4.5 provided a brief discussion of nonplanar arrays.

There are several issues that we have not discussed in our development of classical array theory:

- (i) In some applications, there is mutual coupling between the sensor elements. An input to sensor n will cause an output at sensor m .
- (ii) In some applications, the incoming signals are polarized (either horizontal and vertical or circular).
- (iii) In some applications, the wavefront impinging on the array has curvature.

Although these topics are not discussed in detail, in the discussion of optimum array processing algorithms later in the text, we occasionally point out how these issues impact the performance of the algorithm.

4.7 Problems

P4.1 Rectangular Arrays

Problem 4.1.1

Derive the expressions for θ_H given in (4.27).

Problem 4.1.2

Derive the expressions for ψ_H given in (4.29).

Problem 4.1.3

Assume $N = M = 11$ and $d_x = d_y = \lambda/2$. We use separable Hamming weighting in both the x and y direction: $\theta_0 = 30^\circ$, $\phi_0 = 0^\circ$. Plot the beam pattern and find the directivity D_0 .

Problem 4.1.4

Repeat Problem 4.1.3 for separable Dolph-Chebychev weighting with -30 -dB side-lobes.

Problem 4.1.5

Consider an 11×11 standard square array. (a) The array MRA is broadside. Assume we use a separable Kaiser weighting with $\beta = 6$ in the x and y directions. Find and plot the resulting beam pattern. Compute the directivity and beamwidth. (b) Repeat part (a) for $\theta_0 = 45^\circ$, $\phi_0 = 30^\circ$.

Problem 4.1.6

Consider a 17×17 square array with $d_x = d_y = \lambda/4$. Use the separable Taylor weighting with -30 -dB SLL and $\bar{n} = 6$. Plot the beam pattern and compute the directivity and HPBW.

Problem 4.1.7

Use the $\text{vec}(\cdot)$ notation in Section 4.1.2 to derive the beam pattern for a delay-and-sum (conventional) beamformer for a signal arriving from ψ_{xT} , ψ_{yT} . Is the resulting beam pattern real?

Problem 4.1.8

In many cases, we are interested in beam pattern cuts at $\phi = \phi_c$. Modify the results in Section 4.1.2 to take into account that the beam pattern is a function of a single variable.

Problem 4.1.9

Verify that the results in Section 4.1.2 are valid for N and/or M odd. Are there any restrictions?

Problem 4.1.10

Assume N and M are even. Write $\text{vec}[\mathbf{w}]$ as

$$\text{vec}[\mathbf{w}] = \begin{bmatrix} \mathbf{w}_d \\ -\mathbf{J} \mathbf{w}_d^* \end{bmatrix}, \quad (4.289)$$

where \mathbf{w}_d is a $NM/2 \times 1$ vector corresponding to the upper half of $\text{vec}[\mathbf{w}]$. The total $\text{vec}[\mathbf{w}]$ is conjugate asymmetric. Find the resulting beam pattern.

Problem 4.1.11

Repeat Problem 4.1.5 for the circularly symmetric Kaiser weighting in (4.92).

Problem 4.1.12

Repeat Problem 4.1.5 for a circularly symmetric Hamming weighting. (a) Compare your results to the separable Hamming weightings in Example 4.1.1. (b) Compare the directivities of the two beam patterns.

Problem 4.1.13 [Ell81]

Find the separable weightings for a rectangular grid array with a rectangular boundary if $d_x = 5\lambda/8$, $d_y = 3\lambda/4$, $N = 8$, and $M = 12$, and if 25-dB and 35-dB Dolph-Chebychev patterns are desired in the xz and yz planes, respectively. Assume the main beam points at $\theta_0 = 0^\circ$ and plot the -3 -dB contour of the main beam. What are the heights of the off-axis sidelobes?

Problem 4.1.14 [Ell81]

In Problem 4.1.13, if the element pattern is hemispherically isotropic in $z > 0$ and is zero in $z < 0$, find the peak directivity. What is the areal beamwidth (defined as the area inside the -3 -dB contour)? Find the changes in directivity and areal beamwidth if the beam is scanned to the position $\theta = 30^\circ$, $\phi = 45^\circ$.

Problem 4.1.15 [Ell81]

Design an equispaced planar array under the following specifications.

- (a) Rectangular grid, rectangular boundary, separable distribution.
- (b) Sum and difference pattern capability.
- (c) Sum pattern scannable out to $\theta = 30^\circ$ in any ϕ -cut.
- (d) $\theta_{x0} = 14^\circ$ and $\theta_{y0} = 20^\circ$
- (e) Both principal cuts are Dolph-Chebychev, -20 dB in the xz -plane and -15 dB in the yz -plane.

Problem 4.1.16 [Ell81]

Assume that the sum pattern weighting found for the array of Problem 4.1.13 is retained, except that the sign of the weighting is reversed for the two quadrants in which $x < 0$. Write an expression for the resulting difference pattern. Plot this difference pattern for $\phi = 0^\circ/180^\circ$ and discuss the SLL.

Problem 4.1.17 [Ell81]

A rectangular grid array with $d_x = d_y = 0.7\lambda$ has a circular boundary for which $R = 3\lambda$. Because of the cutoff corners, there are only 13 elements per quadrant. Find

the weighting of this array if one uses Dolph-Chebychev separable weighting with -20 -dB sidelobes and sets the weighting of the three cutoff elements equal to zero. Plot the beam pattern in the cuts $\phi = 0^\circ, 15^\circ, 30^\circ$, and 45° . Find the beamwidth and directivity.

Problem 4.1.18 [Ell81]

Repeat Problem 4.1.17, except use a Tseng-Cheng nonseparable weighting with -20 -dB sidelobes. Find the beamwidth and directivity.

Problem 4.1.19

Repeat Problem 4.1.18 using the transformation in (4.119).

Problem 4.1.20

Consider a 17×17 square array with $d_x = d_y = \lambda/2$. Use the discretized Taylor pattern derived in Example 3.4.3 as a starting point.

- (a) Use the Tseng-Cheng rotation to generate a 2-D beam pattern.
- (b) Sample the pattern in wavenumber space. Use the inverse 2-D DFT to find the array weighting function.

Problem 4.1.21

Consider a standard 17×17 square array. Use the Villenueve \bar{n} weighting discussed in Section 3.4.4 with $\bar{n} = 6$ and -25 -dB sidelobes as a starting point. Repeat Problem 4.1.20.

Problem 4.1.22

Extend the results in Section 4.1.9 to the case of first derivative and second derivative nulls.

Problem 4.1.23

Repeat Example 4.1.9 with zero-, first- and second-order nulls at

$$\psi_{mx} = 0.25\pi, \quad \psi_{my} = 0.433\pi. \quad (4.290)$$

Problem 4.1.24

Repeat Example 4.1.9 with zero-order nulls at the following nine locations:

$$\psi_{mx} = 0.25\pi, \quad \psi_{my} = 0.41\pi, 0.43\pi, 0.45\pi, \quad (4.291)$$

$$\psi_{mx} = 0.27\pi, \quad \psi_{my} = 0.41\pi, 0.43\pi, 0.45\pi, \quad (4.292)$$

$$\psi_{mx} = 0.23\pi, \quad \psi_{my} = 0.41\pi, 0.43\pi, 0.45\pi. \quad (4.293)$$

Problem 4.1.25

Consider the model in Example 4.1.9. The nominal pattern is a symmetrical Dolph-Chebychev with -20 -dB sidelobes.

We want to design an array weighting so that in the region $(20^\circ \leq \theta \leq 50^\circ) \cap (40^\circ < \phi \leq 70^\circ)$ the beam pattern is lower than -50 dB.

Design a nulling scheme to achieve this result. Use as few degrees of freedom as possible. Plot a contour plot of your result.

P4.2 Circular Arrays

Problem 4.2.1

Consider an 8-element circular array with equal spacing between elements. It could also be viewed as two 4-element rectangular arrays with the first array oriented along the x - y axes and the second array rotated by 45° . (a) Using this model, find the beam pattern and compare your result to the result in the text. (b) Assume $d = \lambda$ in the rectangular arrays. Plot the resulting beam pattern.

Problem 4.2.2

Extend the approach in Problem 4.2.1 to other values of N .

Problem 4.2.3

Consider a 10-element circular array with uniform weighting whose radius is $R = \lambda$. Assume that an element is added at the origin with weight w_0 .

Choose w_0 to reduce the height of the first sidelobe.

Problem 4.2.4

Consider the cylindrical array in Figure 4.62. Assume the circular component has 10 isotropic elements in each circle separated by $d = \lambda/2$. There are 10 circular segments separated by $\lambda/2$. Assume uniform weighting of the 100 elements.

Plot the beam pattern.

Problem 4.2.5

Show that a uniform circular array can be modeled as a non-uniform linear array (e.g., pp. 205 of [Ma74]).

Problem 4.2.6

Show that a uniform circular array can be modeled as a set of uniform linear arrays where each ULA corresponds to a fixed θ (e.g., [TH92]).

Problem 4.2.7 [Ma74]

We want to derive the directivity of a single-ring circular array with isotropic elements.

$$D = \frac{4\pi |B_{max}|^2}{\int_0^{2\pi} \int_0^\pi |B(\theta, \phi)|^2 \sin \theta d\theta d\phi}. \quad (4.294)$$

(a) Show that a typical term in $|B(\theta, \phi)|^2$ can be written as,

$$w_m w_n^* \exp[jk\rho_{mn} \sin \theta \cos(\phi - \phi_{mn})], \quad (4.295)$$

$$\rho_{mn} = \begin{cases} 2R \sin \frac{|\phi_m - \phi_n|}{2}, & m \neq n, \\ 0, & m = n, \end{cases} \quad (4.296)$$

$$\phi_{mn} = \tan^{-1} \left[\frac{\sin \phi_m - \sin \phi_n}{\cos \phi_m - \cos \phi_n} \right], \quad m \neq n. \quad (4.297)$$

(b) Show the denominator can be written as $4\pi W$ where

$$W = \sum_{m=0}^{N-1} \sum_{n=0}^{N-1} w_m w_n^* \left(\frac{\sin k\rho_{mn}}{k\rho_{mn}} \right). \quad (4.298)$$

Hint: Utilize the following relation [AS65]:

$$\int_0^{\pi/2} J_0(x \sin \theta) \sin \theta d\theta = \left(\frac{\pi}{2}\right)^{1/2} \frac{J_{1/2}(x)}{(x)^{1/2}} = \frac{\sin x}{x}. \quad (4.299)$$

(c) Then,

$$D = \frac{|B(\theta_0, \phi_0)|^2}{W}. \quad (4.300)$$

Problem 4.2.8

Consider a uniform circular array with radius equal to 4λ . Assume N is chosen so $d = 0.4\lambda$.

- (a) Using phase mode excitation, construct a Hamming pattern in ϕ -space in the xy -plane.
- (b) Plot the beam pattern for $\theta = 30^\circ, 60^\circ$, and 90° .

P4.3 Circular Apertures

Problem 4.3.1

Consider a circular aperture with a separable weighting,

$$w_R(r) = \begin{cases} 1 - \left(\frac{r}{R}\right)^2, & 0 \leq r \leq R, \\ 0, & \text{elsewhere,} \end{cases} \quad (4.301)$$

and $w_\phi(\phi)$ is uniform.

Derive the results in the appropriate column of Table 4.4.

Problem 4.3.2

Repeat Problem 4.3.1 with

$$w_r(r) = \begin{cases} \left[1 - \left(\frac{r}{R}\right)^2\right]^2, & 0 \leq r \leq R, \\ 0, & \text{elsewhere.} \end{cases} \quad (4.302)$$

Problem 4.3.3

Consider the circular aperture in Problem 4.3.1 with the radial taper. Design an aperture weighting that is a least squares approximation to $w_r(r)$ with a constraint that there is a null at $\theta = \frac{110^\circ}{R/\lambda}$ and $\phi = 0^\circ$.

Problem 4.3.4 [Ell81]

A circular Taylor pattern, -20 -dB SLL, $\bar{n} = 3$, is desired from a continuous circular aperture for which $R = 3\lambda$. Find A^2 , σ , and the modified root position u_1 and u_2 . Write the explicit expression for this Taylor pattern. Plot the pattern in $0^\circ \leq \theta \leq 90^\circ$ and the aperture distribution in $0 \leq \rho \leq 3\lambda$.

Problem 4.3.5 [Ell81]

A circular grid array with four concentric rings at radii $\rho/\lambda = 0.7, 1.4, 2.1$, and 2.8 is to be weighted to give a pattern approximating a circular Taylor -20 -dB SLL, $\bar{n} = 3$. Determine the weightings (a) by conventional sampling of the Taylor distribution; (b) by matching to the nulls of the pattern found in Problem 4.3.4.

Problem 4.3.6 [Ell81]

Read the discussion in [Ell81] on Bayliss difference patterns. For a 6λ -diameter continuous circular aperture, find the weighting that will produce -20-dB SLL, $\bar{n} = 3$, Bayliss difference pattern. Write the explicit expressions for pattern function and aperture distribution. Plot both the pattern and the distribution.

Problem 4.3.7

Consider the following alternative to the Taylor circular aperture design procedure.

- (a) Design a linear aperture using the techniques in Section 3.4.3.
- (b) Transform the resulting pattern into two dimensions using the Tseng-Cheng transformation.

Utilize this approach for the model in Example 3.4.3 ($L = 10.5\lambda$) and compare the results to the Taylor circular procedure with $R = 5.25\lambda$.

P4.4 Hexagonal Arrays**Problem 4.4.1**

Consider a standard 61-element hexagonal array. Plot the beam pattern for the following circular aperture ($R = 2.25\lambda$) weightings:

- (a) Uniform
- (b) $w_R(r) = 1 - \left(\frac{r}{R}\right)^2$
- (c) $w_R(r) = \left[1 - \left(\frac{r}{R}\right)^2\right]^2$

Problem 4.4.2 (continuation)

Repeat Problem 4.4.1 for a standard 127-element hexagonal array.

Problem 4.4.3

- (a) Plot the co-array for a standard 61-element hexagonal array.
- (b) Discuss how to reduce the redundancy. Find several lower redundancy arrays.

Problem 4.4.4

Consider a standard 19-element hexagonal array.

- (a) Develop a full-dimension (19) beamspace procedure using orthogonal beams.
- (b) Plot the MRAs of the 19 beams in (u_x, u_y) space.

Problem 4.4.5

Show that (4.266) can be written as

$$B_u(u_x, u_y) = \frac{1}{N_H} \sum_{m=-\frac{N_x-1}{4}, m \text{ odd}}^{\frac{N_x-1}{4}} \left\{ \left[\sum_{n=1}^{\frac{N_x-|m|}{2}} e^{j\pi(n-\frac{1}{2})u_x} + \right. \right. \\ \left. \left. \sum_{n=-\frac{N_x-|m|}{2}}^{-1} e^{j\pi(n+\frac{1}{2})u_x} \right] e^{jm\frac{\sqrt{3}}{2}u_y} \right\} + \sum_{m=-\frac{N_x-1}{2}}^{\frac{N_x-1}{2}} \left\{ \left[\sum_{n=-\frac{N_x-1-|m|}{2}}^{\frac{N_x-1-|m|}{2}} e^{j\pi n u_x} \right] e^{jm\frac{\sqrt{3}}{2}u_y} \right\}. \quad (4.303)$$

Problem 4.4.6

Consider a standard 91-element hexagonal array. Design a beam pattern that has uniform sidelobes that are -40 dB lower than the main lobe. Assume the MRA is broadside and try to minimize the diameter of the main lobe.

P4.5 Nonplanar Arrays**Problem 4.5.1**

Consider two parallel standard N -element linear arrays in the xy -plane. The first array lies on the x -axis and is centered at the origin. The second array is parallel to the first array at $y = d_{sep}$ and is centered on the y -axis.

Assume $N = 40$. Plot the beam pattern for various d_{sep} .

Problem 4.5.2

Consider the array in Example 4.5.1. We want to steer the array to θ_0, ϕ_0 . Use Hamming weighting in the z -direction and Hamming weighting of the phase modes.

- (a) Find the appropriate weights and plot the beam pattern.
- (b) What is the HPBW?

Bibliography

- [AF85] J. Antonucci and P. Franchi. A simple technique to correct for curvature effects on conformed phase arrays. *Proc. 1985 Antenna Applications Symposium*. RADC/TR-85-743, Vol. 2, December 1985.
- [AGW72] N. Amitay, V. Galindo, and C. P. Wu. *Theory and Analysis of Phased Array Antennas*. Wiley-Interscience, New York, 1972.
- [AS65] M. Abramowitz and I. A. Stegun. *Handbook of Mathematical Functions*. Dover Publications, New York, 1965.
- [Bag76] A. B. Bagheroer. Space-time processes and optimal array processing. Technical Report 506, Navy Undersea Center, San Diego, California, December 1976.
- [Bak66] Y. V. Baklanov. Chebyshev distribution of currents for a plane array of radiators. *Radio Eng. Electron. Phys.*, vol.11, pp. 640–642, April 1966.
- [Bal82] C. A. Balanis. *Antenna Theory Analysis and Design*. Wiley, New York, 1982.

- [Bay68] E. T. Bayliss. Design of monopulse antenna difference patterns with low side lobes. *Bell System Tech. J.*, vol.47, pp. 623–640, May–June 1968.
- [BB72] G. V. Borgiotti and Q. Balzano. Analysis and element pattern design of periodic arrays of circular aperture on conducting cylinders. *IEEE Trans. Antennas Propagat.*, vol.AP-20, pp. 547–555, September 1972.
- [BVT99] K. L. Bell and H. L. Van Trees. Adaptive and non-adaptive beampattern control using quadratic beampattern constraints. *Proc. 33rd Asilomar Conference on Signals, Systems, and Computers*, Pacific Grove, California, pp. 486–490, October 1999.
- [Bor87] G. V. Borgiotti. Conformal arrays. In A. Rudge et al., editors, *The Handbook of Antenna Design*, vol.2, chapter 11, Peter Peregrinus, London, 1987.
- [CIS68] A. K. Chan, A. Ishimaru, and R. A. Siegelmann. Equally spaced spherical arrays. *Radio Sci.*, vol.3, pp. 401–404, May 1968.
- [Dav65] D. E. N. Davies. A transformation between the phasing techniques required for linear and circular aerial arrays. *Proc. IEE*, vo.112, pp. 2041–2045, November 1965.
- [Dav87] D. E. N. Davies. Circular arrays. In A. Rudge et al., editors, *The Handbook of Antenna Design*, vol.2, chapter 12, Peter Peregrinus, London, 1987.
- [DM84] D. E. Dudgeon and R. M. Mersereau. *Multidimensional Digital Signal Processing*. Prentice-Hall, Englewood Cliffs, New Jersey, 1984.
- [Ell64] R. S. Elliott. Beamwidth and directivity of large scanning arrays. *Microwave J.*, pp. 74–82, January 1964.
- [Ell81] R. S. Elliott. *Antenna Theory and Design*. Prentice-Hall, Englewood Cliffs, New Jersey, 1981.
- [Han59] R. C. Hansen. Tables of Taylor distributions for circular aperture antennas. Technical Report 587, Hughes Aircraft Co., Culver City, California, February 1959.
- [Han60] R. C. Hansen. Tables of Taylor distributions for circular aperture antennas. *IRE Trans. Antennas Propagat.*, vol.AP-8, pp.22–26, January 1960.
- [Han81] R. C. Hansen. *Conformal Antenna Array Design Handbook*. Dept. of the Navy, Air Systems Command, AD A11091, September 1981.
- [Han98] R.C. Hansen, editor. *Phased Array Antennas*. Wiley, New York, 1998.
- [Hes70] A. Hessel. Mutual coupling effects in circular arrays on cylindrical surfaces—aperture design implications and analysis. In A. A. Oliner and G. H. Knittel, editors, *Phased Array Antennas*, pp. 273–291, Artech House, Boston, 1972.
- [HL52] R. F. Harrington and W. R. Lepage. Directional antenna arrays of elements circularly disposed about a cylindrical reflector. *Proc. IRE*, vol.40, pp. 83–86, January 1952.
- [Hof63] M. Hoffman. Conventions for the analysis of spherical arrays. *IEEE Trans. Antennas Propagat.*, vol.AP-11, pp. 390–393, July 1963.
- [Hua81] T. S. Huang. Two-dimensional digital signal processing I. In *Topics in Applied Physics*, vol.42, Springer-Verlag, New York, 1981.

- [Jam47] P. W. James. Polar patterns of phase-connected circular arrays. *Proc. IEE*, vol.112, pp. 1839–1847, 1965.
- [Jas61] H. Jasik, editor. *Antenna Engineering Handbook*, pp. 2-25–2-26. McGraw-Hill, New York, 1961.
- [Knu59] H. Knudsen. Antennas on circular cylinders. *IRE Trans. Antennas Propagat.*, vol.AP-7, pp. S361–S370, December 1959.
- [KSV73] W. H. Kummer, A. F. Seaton and A. T. Villeneuve. Conformal antenna arrays study. Final Report, AD-909220, Hughes Aircraft Co., Culver City, California, January 1973.
- [LL65] S. W. Lee and Y. T. Lo. Pattern function of circular arc arrays. *IEEE Trans. Antennas Propagat.*, vol.AP-13, pp. 649–650, July 1965.
- [LL83] Y. T. Lo and S. W. Lee. *Antenna Handbook, Volume II (Antenna Theory)*. Van Nostrand Reinhold, New York, 1983.
- [Ma74] M. T. Ma. *Theory and Applications of Antenna Arrays*. Wiley, New York, 1974.
- [Mai84] R. J. Mailloux. Conformal and Low-Profile Arrays. In R. C. Johnson and H. Jasik, editors, *Antenna Engineering Handbook*, chapter 21, McGraw-Hill, New York, 1984.
- [Mai94] R. J. Mailloux. *Phased Array Antenna Handbook*. Artech House, Boston, 1994.
- [McC82] J. H. McClellan. Multidimensional spectral estimation. *Proc. IEEE*, vol.70, no.9, pp. 1029–1039, September 1982.
- [Mer79] R. M. Mersereau. The processing of hexagonally sampled two-dimensional signals. *Proc. IEEE*, vol.67, no.6, pp. 930–949, July 1979.
- [MG70] A. D. Munger and B. R. Gladman. Pattern analysis for cylindrical and conical arrays. *Proc. Conformed Array Conference*, AD-875 378, Naval Electronics Lab. Center, San Diego, California, January 1970.
- [MP68] R. H. MacPhie. The element density of a spherical antenna array. *IEEE Trans. Antennas Propagat.*, vol.AP-16, pp. 125–127, January 1968.
- [MZ94] C. P. Mathews and M. D. Zoltowski. Eigenstructure techniques for 2-D angle estimation with uniform circular arrays. *IEEE Trans. Signal Process.*, vol.42, no.9, pp. 2395–2407, September 1994.
- [PM62] D. P. Peterson and D. Middleton. Sampling and reconstruction of wave-number limited functions in n -dimensional Euclidean spaces. *Inf. Control*, vol.5, pp. 279–323, April 1962.
- [R⁺83] A. W. Rudge et al., editors. *The Handbook of Antenna Design*, chapter 12. Peregrinus, London, 1983.
- [RD82] T. Rahim and D. E. N. Davies. Effect of directional elements on the directional response of circular arrays *Proc. IEE*, vol.129, Part 11, no.1, pp. 18–22, February 1982.
- [RG75] L. R. Rabiner and B. Gold. *Theory and Application of Digital Signal Processing*. Prentice-Hall, Englewood Cliffs, New Jersey, 1975.
- [Sch72] H. E. Schrank. Basic theoretical aspects of spherical phased arrays. In A. A. Oliner and G. H. Knittel, editors, *Phased Array Antennas.*, pp. 323–327, Artech House, Boston, 1972.

- [SSL68] D. L. Sengupta, T. M. Smith and R. W. Larson. Radiation characteristics of a spherical array of circularly polarized elements. *IEEE Trans. Antennas Propagat.*, vol.AP-16, pp. 2–7, January 1968.
- [Sha61] E. D. Sharp. A triangular arrangement of planar-array elements that reduces the number needed. *IRE Trans. Antennas Propagat.*, vol.AP-3, pp. 126–129, January 1961.
- [She75] B. Sheleg. Circular and cylindrical arrays. *Workshop on Conformal Antennas*, AD-A015 630, Naval Air Systems Command, pp. 107–138, April 1975.
- [SK82] J. C. Sureau and K. J. Keeping. Sidelobe control in cylindrical arrays. *IEEE Trans. Antennas Propagat.*, vol.AP-37, pp. 1017–1018, 1989.
- [Ste81] S. Stein. Algorithms for ambiguity function processing. *IEEE Trans. Acoust., Speech, Signal Processing*, vol.ASSP-29, no.3, pp. 588–599, June 1981.
- [Tay60] T. T. Taylor. Design of circular apertures for narrow beamwidth and low sidelobes. *IRE Trans. Antennas Propagat.*, vol.AP-8, pp. 17–22, 1960.
- [TC68] F. I. Tseng and D. K. Cheng. Optimum scannable planar arrays with an invariant side-lobe level. *Proc. IEEE*, vol.56, pp. 1771–1778, 1968.
- [TH92] A. H. Tewfik and W. Hong. On the application of uniform linear array bearing estimation techniques to uniform circular arrays. *IEEE Trans. Signal Process.*, vol.40, no.4, pp. 1008–1011, April 1992.
- [Zio95] L. J. Ziomek. *Fundamentals of Acoustic Field Theory and Space-Time Signal Processing*. CRC Press, Boca Raton, Florida, 1995.

Copyright of Optimum Array Processing is the property of John Wiley & Sons, Inc. 2002 and its content may not be copied or emailed to multiple sites or posted to a listserv without the copyright holder's express written permission. However, users may print, download, or email articles for individual use.